IONIZATIONAL NONEQUILIBRIUM AND IGNITION IN PLASMA ACCELERATORS

by

Eric James Sheppard

B.S. Aerospace Eng., Boston University, 1983
S.M., Aeronautics and Astronatics, MIT, 1985
SUBMITTED IN PARTIAL FULFILLMENT OF THE
REQUIREMENTS FOR THE DEGREE OF
Doctor of Science
in
Aeronautics and Astronautics
at the
Massachusetts Institute of Technology
February, 1994

Signature of Author ________________
Department of Aeronautics and Astronautics
December 21, 1993

Certified by ________________
Professor Manuel Martinez-Sanchez, Thesis Advisor
Department of Aeronautics and Astronautics

Certified by ________________
Professor Judson R. Baron
Department of Aeronautics and Astronautics

Certified by ________________
Professor Daniel E. Hastings
Department of Aeronautics and Astronautics

Accepted by ________________
Professor Harold Y. Wachman, Chairman
Department Graduate Committee

Ionizational Nonequilibrium and Ignition in Self-Field Magnetoplasmadynamic Thrusters

by

Eric James Sheppard

SUBMITTED TO THE DEPARTMENT OF AERONAUTICS AND ASTRONAUTICS
IN PARTIAL FULFILLMENT OF THE REQUIREMENTS FOR THE DEGREE OF
DOCTOR OF SCIENCE

Abstract

The focus of this work is on identifying the processes behind the sustained initiation of ionization, or "ignition", at the inlet of a self-field magnetoplasmadynamic thruster (MPDT). Plasma accelerators generate high Isp thrust via a combination of high power densities and low mass densities, resulting in strong gradients of temperature and density, particularly in the areas of current concentration. Thermodynamic equilibrium is generally a poor assumption under such high power loading and this effects the excited state population distribution which is needed for calculating the overall recombination coefficients used in numerical flow models. These nonequilibrium conditions must be understood in order to accurately model the plasma.

A classical approach is adapted to characterize the nonequilibrium ionization problem. Atomic or ionic species are modeled by their electronically excited state structure for detailed finite-rate analysis of multi-step ionization processes, including both inelastic collisions and radiation (in a parametric form). The time scales for the excited states are found to be small enough compared to the ground state's to make the quasi-steady-state-solution assumption, which allows the excited state population distribution relative to the ground state to be determined by a modified mass balance law. Neglecting radiative effects, which are shown to be small in MPDTs, the overall rate coefficients for electron-neutral ionization collisions and electron-electron-ion recombination collisions are calculated for the hydrogen atom, and the argon atom and first ion.

These rate models are applied to the problem of ignition in a self-field MPDT, where the propellant is injected into the thruster neutral, but the plasma must be at least partially ionized at the inlet for effective electromagnetic thrust. Back-diffusion is assumed to be responsible for transporting electron-ion pairs back to the inlet wall (which is ion-attracting), and sustaining the initiation of ionization there. This approach is similar to that taken in diffusion flames, and other diffusion-reaction situations. Results from a simple, but illustrative, constant speed igntion model indicate that there is a "blowoff speed" ignition criterion. That is, if the propellant is injected at a speed less than the blowoff speed, then back-diffusion is sufficient to supply the inlet wall with enough electrons to initiate ionization. If the propellant is injected at a speed greater than the blowoff speed, then diffusion cannot supply the inlet with electrons, and the ionization front gets "blown" downstream. This explanation should hold generally even for the more realistic accelerating flow case. For atomic injection, the blowoff speed depends on the ambipolar coefficient, and the ionization rate constant of the propellant. Therefore, propellants of high diffusivity and low ionization potential will ignite more readily at a given temperature. Although temperature variation in the ionizing region is found to have little effect on the ignition of a constant speed plasma, the ionization rate coefficient is a strong function of the electron temperature, which is set by an overall energy balance in the channel. In the accelerating plasma ignition model, both momentum and energy are accounted for self-consistently. The resulting inlet speeds were generally small enough to avoid "blowoff", and the ionizing length scales were on the order of mm and were shorter than the magnetic diffusion scale length under typical self-field MPDT conditions. It was found that increasing the contraction ratio in the thruster channel lowered the electron temperature, which tended to quench ionization and stretch out the ionizing region. This work has shown that the initiation of ionization at the inlet of an MPDT may be explained by convective, diffusive, and collisional ionization processes alone, and is the first step towards a complete understanding of the initial ionization process in self-field MPDTs.

Thesis Supervisor: Professor Manuel Martinez-Sanchez
Department of Aeronautics and Astronautics

Acknowledgements

I couldn't imagine beginning these acknowledgements in any other way than by thanking Professor Manuel Martinez-Sanchez for teaching me to be a "rocket scientist". I am thankful that I had this opportunity to learn from him. Over the years (and there have been many of them), he has managed to teach me how to think about as sharply as I can.

I would also like to thank the other two members of my thesis committee. Prof. Judson Baron's probing questions and helpful comments were a great help. Prof. Daniel Hastings always kept me on my toes at our group seminars, and was a source of support in several roles over the years. Other Professors who had some impact on my MIT years were Professors David Akin, Leon Trilling, Douglas Carmichael, and the late Prof. James Melcher, who reminded me by example that one should strive to be both a good engineer *and* a good citizen. Professors Trilling and David Gonzales were kind enough to act as readers for my defense. I would also like to reach back and mention Professors Daniel Udelson and Luigi Morino of Boston University who were instrumental in getting me across the Charles River in the first place. My work over the years on AIAA student branch activities, Project Interphase, the Second Summer program, and MITES have been excellent learning experiences and outlets, and I would like to acknowledge that part of my education.

I would also like to acknowledge the GPOP Fellowship program, and the AFOSR, which both partially supported my doctoral studies.

Although I seem to have a talent for being a hermit, many lives have crossed mine and helped me to arrive here a little wiser or at least a little happier. Wayne Sprauve and Teresa Villarreal were there since the B.U. days, and they and their spouses continue to be my dear friends. My two roommates at BU, Paul French and Mike Thomas remain close and wise comrades. Here at MIT, Boris Zaretsky, Patrick Hanley, and their families have become part of my extended family.

Of course, my colleagues here at the MIT SPPL, SSL, and/or FDRL were always there to keep me on my toes one way or another. Heartfelt thanks and best wishes to Jean-Marc Chanty for our long and interesting friendship, David Rivas for always reminding me of what's important, Knox Milesap for the idea of a BBQ survey, Rodger Biasca for computer help and steadfast bowling, Eli Niewood for MPD talks and friendship, Scott Miller for explaining arcjets to me, and everyone else I can't think of as I write this. Thanks too to

the core of the MIT 4 Ace Club, J.P. and Mike Clarke, Rudy King, and Tom Washington, for their friendship, and some great lunches. Peggy Edwards' support, friendship, and sunny disposition helped brighten up this last hectic year.

In the "real" world, there are far too many names to fit in here, but I'd like to mention the Burditts, the Gillespie-Mobleys, John-Ralston Haynes, Jack Jensen, Theresa Linehan, Dennis Porche, and the VanNess family, who are always close in my thoughts despite the miles or years between us.

Everything I have managed to muddle through so far has been motivated, inspired, and supported by the many and various far-flung members of my family. Thanks to my siblings, Paulette, Arthur, Robert and sister-in-law Laurel for the joy of sharing in your generation. Thanks to all the littler (or at least younger) ones who kept me smiling. And thanks to Mom and Dad for, well, *me*, and all that followed.

And thank God for making everything possible.

This thesis is dedicated to three of the women in my life that aren't here to read it, but certainly contributed: Maude Tavares, Catherine Sheppard, and Hyacinth Young, my grandmothers and aunt.

Contents

List of Figures

List of Tables

Nomenclature

AI	Argon neutral atom.
AII	First Argon ion.
A_{jk}	Radiative transition probability.
B_{kj}	Einstein coefficient for stimulated emission
B_{jk}	Einstein coefficient for absorption
$\bar{c}$	A thermal speed.
C_a	Ambipolar diffusion factor $= D_a n_g$.
D_a	Ambipolar diffusion coefficient.
e	Electron charge $= 1.6 \times 10^{-19} C$.
E	Electric field.
E_{jk}	Energy gap between atomic levels j and k.
g_k	Degeneracy of a level.
G	Particle flux per unit area $G = u n_g$.
h	Channel height$/\sqrt{12}$.
h	Planck's constant $= 6.6 \times 10^{-34} Js$.
H	Channel height.
H	Hydrogen atom.
I_{kc}	Integral for collisional rate coefficient.
I_ν	Intensity of radiation from a line.
k_B	Boltzmann constant $= 1.38 \times 10^{-23} J/K$.
K_e	Electron thermal conductivity.
L	Thruster characteristic length.
Le	Lewis number.
$\dot{m}$	Mass flow rate.

m_e	Electron mass.
m_i	Ion mass.
n_e	Electron number density.
n_k	Number density of level k of the atom.
n_a	Atomic number density $= \sum_k n_k$.
n_g	Total heavy particle number density.
Π	Nondimensional Ohmic heating parameter.
R_m	Magnetic Reynolds number, $R_m = \mu\sigma uL$.
S_{jk}	Collisional rate coefficient.
t	Time.
T_e	Electron temperature.
T_g	Heavy particle temperature.
T_x	Excited level distribution temperature.
u	Parallel (streamwise) component of velocity.
v	Transverse component of velocity.
v_B	Bohm velocity.
V_i	Ion slip speed.
α	Ionization fraction, $\alpha = \frac{n_e}{n}$.
β	The ratio v_B^2/u_{ref}^2.
β_{kj}	Radiative escape factor.
Γ	Ion slip flux variable: $\Gamma = -n_e V_i$.
δ_k	Degree of nonequilibrium.
ρ	Mass density.
θ	Ratio of temperatures: $\theta = T_g/(T_g + T_e)$.
θ_{jk}	Collisional rate parameter, $\frac{k_B T_e}{E_{jk}}$.
λ	A mean-free-path, or a non-dimensional parameter.
Λ_m	Magnetic diffusion length scale.
Λ_n	A parameter in the ignition models.
τ	Optical depth.
χ_k	Coefficient of δ_1 in equation 3.21.
ψ_k	Radiative term in equation 3.21.

ϕ	Voltage.
ξ	Nondimensional streamwise length.
η	Nondimensional frequency.
ν	Frequency.
$\nu_o/2$	Half-width at half-height frequency.
σ	Electrical conductivity.

Chapter 1

Introduction

1.1 Objective

The goal of this work is to investigate the processes which act in the steady- state transition from an injected gas (of unknown but small ionization fraction) to a plasma (ionized gas) at the inlet of a self-field magnetoplasmadynamic thruster (MPDT). This work will explain the experimentally observed presence of a sustained mm-scale ionization front by first building up a model of the collisional ionization process, and then using this model in channel flow models which approximate MPDT flow. The steady-state maintenance of the ionization region, or "front", at the inlet is referred to here as ionizational "ignition".

This must ultimately be done within the physical context of the gas injection method used, which may involve complicated flow and current interactions in two or three dimensions, but such complications are not considered here. Instead, the focus will be on the physical processes which may influence ignition themselves, and the quasi-one-dimensional approach taken here is justified within the context of other researchers' work on similar problems. The propellant will be assumed to be injected through a porous backplate which results in essentially a one dimensional (the streamwise direction) flow problem, and this will be the basis for the analysis.

The next few sections will outline the ionizational ignition problem and the approach that will be taken here to analyze it. First, self-field magnetoplasmadynamic thrusters (MPDT) are described briefly, within the field of space propulsion in general. Next, nonequilibrium ionization issues in MPDT are discussed, followed by a discussion of the background of research on relevant nonequilibrium ionization and ignition problems and the approach taken here. Finally, the organization of the main body of the thesis is outlined.

1.2 Self-Field Magnetoplasmadynamic Thrusters

Rocket-powered vehicles produce thrust by imparting momentum and energy to their propellant as it is expelled from the vehicle. This may be achieved by chemical combustion, by heating (nuclear or electrical), or by electromagnetic acceleration. All are self-contained in that the working propellant must be carried on-board. While all rockets work on the same basic principles, there are several different types, each of which may be attractive for particular missions. [28] The following paragraphs briefly outline some of the fundamentals

.

To change the velocity of a space vehicle by an amount Δv (which is a function of the orbital maneuver being undertaken), using a thruster with exit velocity of u_{ex}, requires that the ratio of propellant mass used in the thrusting (M_p) to the initial mass of the spacecraft (M_o) (including the propellant) is governed the "rocket equation" [32] [28]:

$$\frac{M_p}{M_o} = 1 - \exp(-\Delta v / u_{ex})$$

For smaller $\Delta v / u_{ex}$, the propellant fraction is smaller. Thus, the exit velocity of the propellant, u_{ex}, is an important factor. Another parameter which is used in the field, which has the advantage of having the same units in either the fps or mks system, is the specific impulse, $I_{sp} = u_{ex}/g$, where g is the gravitational acceleration at the earth's surface.

There are three major types of rocket propulsion. Chemical, which includes both solid and liquid propellants, is by far the most prevalent. These devices create a high pressure in a combustion chamber via chemical reactions. In nuclear thermal rockets, a reactor heats the propellant directly or indirectly. Electric propulsion includes electrostatic (ion engines), electrothermal (resistojets, or, at higher power, arcjets), and electromagnetic (including the so-called magnetoplasmadynamic thrusters: MPDT) accelerators.

Chemical rockets have the advantage of carrying the energy source along inside the fuel and oxidizer, which is a savings in dead-mass. They are, however, limited to specific impulses of approximately 250-300 s for solids, 220-230 s for hydrazine, and 450 s for a hydrogen-oxygen mixture.

Nuclear rockets are very attractive because they offer the potential of both high specific impulse and thrust density. However, there are several issues which complicate their development, such as radiative contamination issues and the associated shielding structure (perhaps a large mass penalty) and operating lifetime.

Electromagnetic accelerators must carry external power supplies, which may be technical challenges by themselves in cases where the power needed is great (which is the case for MPDTs, which require power on the order of megawatts). However, they are limited in impulse only by the power supply available and perhaps by physical instabilities, and other limitations on thrust efficiency. High specific impulse is mass-efficient, although trip times using continuous, low thrust trajectories may be longer than for chemical propulsion, using impulsive maneuvers, for many missions. For a constant acceleration, $a = T/M$, where T is the thrust and M is the mass of the spacecraft, the trip time is the total velocity change divided by this acceleration:

$$t \approx \frac{\Delta v}{a}$$

so there is a time penalty for operating at lower continuous thrust. Comparison to impulsive thrust trip times is not direct since the trajectories include considerable coasting time, so that low-thrust trajectories may actually take less time for very long missions. Plasma rockets achieve relatively high specific impulses by using high power densities to accelerate low density propellants. Arcjets accelerate the flow electrothermally, magnetoplasmadynamic thrusters (MPDT) electromagnetically, and ion engines electrostatically.

While many of these plasma accelerators have been studied for 30 or more years, there are still many aspects of their operation which are not fully understood. Part of the lingering difficulties is due to the wide range of operating regimes which occur in different experiments (different thruster geometries, currents, propellants, diagnostic techniques). The complicated nature of plasmadynamics for an ionizing, accelerating, heating propellant has slowed the progress of analysis and has required many simplifications. This thesis will focus on the ionizational processes in a self-field MPDT.

Figure 1.1 is a schematic of the channel geometry for a 1-D self-field MPDT. In reality, they are coaxial devices, with a cylindrical anode (of radius r_a) outside of a cylindrical cathode (radius r_c), so that the diagram shows the upper half of such a thruster. Typical length scales for MPDT are: thruster length $L \approx 0.2m$, and electrode to electrode gap of

$H = r_a - r_c \approx 0.02m$ (cathode radii are on the order of $.05m$). In the quasi-1-D approach taken in this work, the flow will be considered to be completely axial, the current will be assumed to be completely transverse and the induced magnetic field will be into the page.

The plasma is accelerated by the Lorenz force (the cross product of the current and magnetic field). In applied MPDT, an external magnetic field is used. In self-field MPDT, the magnetic field induced by the current flowing in the plasma is used.

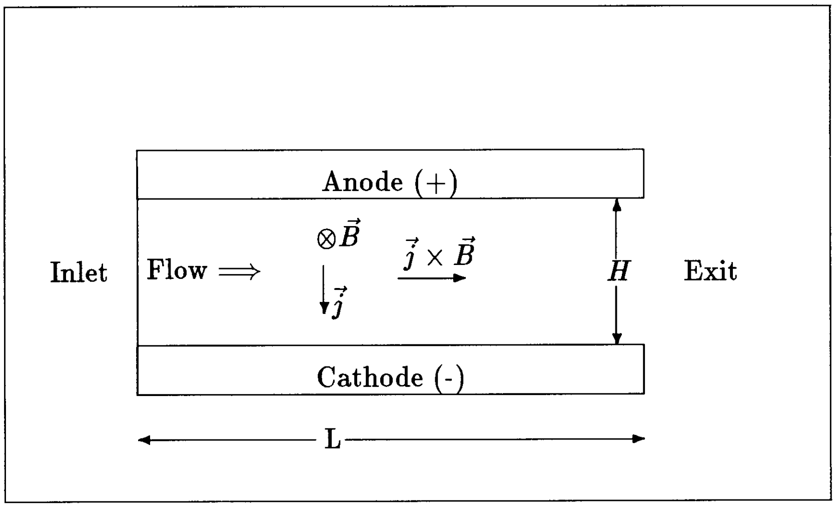

Figure 1.1: Simple 1-D, constant area MPDT channel

The purely electromagnetic thrust, T, of a self-field MPDT with applied current J is [32], [38]

$$T = bJ^2 = \dot{m}u_{ex}$$

where b, the self-field electromagnetic coefficient [21] is, using mks units:

$$b = \left(\ln\frac{r_a}{r_c} + \frac{3}{4}\right) \times 10^{-7}$$

and J is the discharge current, $\dot{m}$ is the mass flow rate, and u_{ex} is the exhaust velocity.

The thrust efficiency is

$$\eta = \frac{\dot{m}u_{ex}^2}{2JV}$$

where V is the discharge voltage, which is a function of the current and thruster conditions. [51]

MPD thrusters operate in an attractive regime. They have higher thrust densities than ion thrusters, but less than that of chemical rockets. Their specific impulse is higher than that of chemical rockets, but lower than that of ion engines. Therefore, MPDTs provide mass savings over chemical rockets, but not with the time penalty of ion engines.

MPDTs have also been shown to operate with a fairly wide variety of of inert and available gases, and over a wide range of thrust and specific impulse [17]. Argon, molecular hydrogen, molecular oxygen, molecular nitrogen, helium, lithium, and ammonia, [21] have been used.

Unlike ion thrusters, for example, MPDTs do not have distinct ion sources or ionizing regions and acceleration regions. As Niewood [51] has shown numerically, both ionization and acceleration may occur throughout the length of the device.

An important limitation on MPDT operation has been seen in experiments. As the current is increased, a limit appears, referred to as “onset”. This behavior has been seen to scale as the ratio of the square of the applied current to the mass flow rate. Several explanations have been extended to explain this phenomenon, or perhaps phenomena, characterized by high frequency voltage oscillations, and increased electrode erosion. [42] In this work, it is assumed that the thrusters are operating below the onset limit, so that conditions may be taken to be steady and laminar.

1.3 Nonequilibrium Ionization in Self-Field MPD Thrusters

Both the interpretation of spectroscopic diagnostics and the numerical simulation of plasma accelerators require accurate knowledge of the ionizational state of the plasma. Prediction of the ionization fraction under the typically high power to mass loading found in the thrusters requires a full accounting for a variety of non-equilibrium effects: rapid density changes, charge pair diffusion to walls and radiation escape, among them.

The total energy input into a self-field MPDT is higher than the ionization energy of the working gas, as the propellant is both ionized and accelerated. Combined with short residence times, and low densities, the plasma is likely to be out of local thermodynamic equilibrium (LTE) in some, if not all, of the thruster. If these devices are to be understood thoroughly, including the interpretation of optical diagnostics and the development of accurate numerical models, nonequilibrium analysis will be required.

Much work, both analytically and numerically, has been done assuming equilibrium or frozen flow, or by using nonequilibrium rate equations which are not appropriate for some of the conditions found in plasma accelerators. Some of these models were designed for use only within a specific temperature range, some ignore species variations and neglect significant differences, and some are based on assumes ranges of densities and temperatures which do not correspond to realistic accelerators. This thesis will first develop the tools necessary to improve on such work, and then extend the analysis by considering a case of special interest.

For this analysis, the atom or ion of interest will be analyzed in detail. The atom or ion structure is defined by energy states: its ground state, its electronically excited states (actually states lumped into more convenient levels), and its continuum (the next higher ion) [49] [7]. This model is necessary to accurately account for the processes responsible for the overall ionization rate. For example, the overall ionization rate may primarily be due to direct ground state to continuum collisional or radiative transitions (likely at high electron temperatures, as will be shown in Chapter 3). Alternatively, the overall rate may be primarily due to multi-step transitions where the atom is excited to higher and higher states by collisions or radiation until it reaches the continuum, or ionizes (this is the case at low temperature, as was exploited by Hinnov and Hirschberg's analysis [29], and will also be shown in Chapter 3).

We are interested in the processes which produce the initial ionization region at the inlet, as the performance of the thrusters will depend on whether some ignition condition is met. Preliminary to this work, we will carry out a detailed look at nonequilibrium ionization processes.

Of particular concern in this analysis are the roles of:

- Metastables. The metastable excited states (or pseudometastable lumped states), or at least the low-lying electronic states, may be significant in the ignition process, as relatively long-lifetime stages of multi-step ionization.

- Diffusion. Ambipolar diffusion, both streamwise and transverse, may contribute to the ionizing processes by direct loss or gain of atoms and/or ions and electrons (which then are available to ionize neutrals).

- Radiation. Photoionizing radiation may reach the inlet region from downstream. This is a non-local effect, requiring information about the state of the downstream plasma.

The parameters which influence ionizational ignition may involve the following variables: inlet density, temperature, and ionization fraction, as well as current density, applied electric field, and channel dimensions.

Besides the primary goal of analyzing nonequilibrium ionization effects on inlet ionization, this work will yield some results that are useful to the study of additional problems. One example is the calculation of the excited state population distribution of an atom or ion, which is needed if line radiation (from radiative decay between excited states) is considered, both for production and absorption calculations. Radiative effects are only likely to be significant in the production of ions near the inlet, where low temperatures and electron number density combine to reduce collisional effects [14], but there may still be some energy loss due to radiation, and, more importantly, there may be sufficient radiative emission for spectroscopic measurements to be made in the laboratory. An overall ionization rate model for an atom (and, for argon, an atom/ion mixture) which includes the effects of the excited states in a form which is compatible with computational models is developed in this thesis. Such a model can be used to bridge the gap between detailed flow calculations and spectroscopic diagnostics [59] and aid in the interpretation of such experimental measurements [36]. This is because the excited state populations may be backed out of the computational model in post-processing, as described in Appendix D.

1.4 Previous Work in this Field

1.4.1 Nonequilibrium Ionization

The standard method used for nonequilibrium ionization modeling is the so-called Collisional-Radiative (CR) model, which models an atom or ion as a ground state, its electronically excited states, and the continuum (the next higher ion). Intra-state transitions via both collisions (excitation/de-excitation, ionization/recombination) and radiation (radiative decay/stimulated excitation, photoionization/recombination) are included in rate equations - linear in the excited state populations - for each state. Collisional-radiative modeling of nonequilibrium plasmas has been analyzed by many authors for the last 30 years. Following is a brief review of some of this work that is relevant to the present work. The work that follows in chapter 3 is based on the framework that these researchers have built.

Van der Sijde, et al. [71] have published a comprehensive description and review of CR modeling in plasmas which covers the aims and limitations of this work. CR models aim to study elementary collisional and radiative processes by comparison with experiment, to determine the distribution of excited state populations, and calculate rate coefficients, to determine electron density and electron temperature from spectroscopic diagnostics, and to model plasma discharges and light sources, such as gas lasers. The CR modeling done in this thesis has as its primary goal the second aim listed: the calculation of overall ionization and recombination coefficients, with the excited state population distribution of significant but secondary interest. The limitations include the exclusion of molecular species (molecular ions) and the associated creation/destruction processes (their addition would require the addition of vibrational and rotational states), the assumption (generally) that the electrons have a Maxwellian velocity distribution, and that the model is limited to electron driven collisions (the addition of heavy particle - heavy particle collisions is possible, but it makes the rate model nonlinear in the excited state populations in a self-consistent model). They conclude that it is possible to have a qualitative, and, in some cases, a quantitative description of CR models of plasmas, that it should be possible to apply these models to atoms other than hydrogen (for which the original CR models were designed), and that the global character of analytic models of atoms may be simplified for the upper excited states when the time scales for the excited states' reactions are much smaller than the other characteristic time scales for the problem. This last point, the quasi-steady-state-solution assumption, allows the population distribution of the excited states to be calculated by imposing a dynamic balance on the excited states that is akin to the law of mass balance. In this case, radiative effects, and the influence of the ground state, which has a longer characteristic time scale, are included. This will be tested and then taken advantage of in chapter 3 of this thesis.

Bates, Kingston and McWhirter first proposed the classic CR model which considered a simple 3-level hydrogen atom The effect on the rate of loss of the population of an excited level by radiation was included in a parametric manner. The radiation produced by the spontaneous decay of an excited atom and resulting in an atom at a lower energy state may be locally absorbed by another of the lower energy atoms. This is known as the optically thick case, and if this is so, there is no net effect on the population of either the higher or lower state, since each level loses and gains one particle per event. In optically thin plasmas, there is no local reabsorption of the radiation, and each spontaneous decay of an excited atom results in a loss of one particle to that level, and a gain of one particle to the lower level. Bates, et al., presented results for optically thin [7], and optically thick [8] plasmas. The net rate of number density production was written for each level plus the continuum - the ion - including excitation and ionization (and their reverse processes) via both collisional and radiative processes. This formulation is the basis for most collisional-radiative modeling. Their work was an investigation of the recombination process, both collisional and radiative, for dense and tenuous plasmas, and noted that the overall "collisional-radiative recombination rate coefficient" had both a temperature and density dependence (as will be shown in chapter 3).

Hinnov and Hirschberg [29] developed a model for the overall three-body (electron-electron-ion) recombination rate of hydrogen atoms by assuming that the entire atom-continuum multi-step pathway is driven by a critical electronically excited level approximately $0.25eV$ lower than the ionizational potential energy. This assumption posits that the ionization process is multi-step, and that when the atom reaches an excited state at or above the critical level, it is essentially ionized, since the reaction rates above the critical level are very fast. This assumption was made for temperatures below 3000 K. Their model has been used in the past both for nonhydrogenic atoms and at temperatures well above their suggested temperature limit. As will be seen later in this chapter, use of the Hinnov-Hirschberg formula for other atoms at higher temperatures may yield results in error by several orders of magnitude. At temperatures below their recommendation of $3000K$, the Hinnov-Hirschberg formula is in good agreement with experimental observations. For temperatures between $3000K$ and $11600K$ (1 eV), their formula overestimates the recombination coefficient found in experiments by a factor which is less than ten [49], and at higher temperatures, the error grows. The Hinnov-Hirschberg formulation gives almost the same result as the much earlier Thompson model of recombination (extended to electron-electron-ion recombination [49]) which does not distinguish between atomic species.

Suckewer used a similar CR model as Bates, et al. [65] and assumed that each level's net production rate consists of excitation up from lower levels, and de-excitation down from the level into the lower levels (both collisional and radiative). This assumes that net ionization and net transitions to higher states are small compared to collisional excitation to lower levels. This simplified the algebra for solving for the populations of the levels, as only the levels below a particular level affect that levels population. This is somewhat similar to the formulation that will be used here, except all transitions are retained in the model outlined in Chapter 3 of this thesis.

Bacri and Gomes [4] [5]) have considered detailed, multi-level CR models of both the argon atom and ion in order to analyze the conditions for Local Thermal Equilibrium (LTE) of the excited states, and the determination of kinetic temperatures for atoms, ions, and electrons in argon plasmas. The standard CR model was applied to stationary arc discharges at atmospheric pressure, over an electron temperature range of $5000\ K < T_e < 13000\ K$, and an electron number density range of $10^{11}\ cm^{-3} < n_e < 10^{17}\ cm^{-3}$ (which correspond to the asymptotic region of an argon constricted arc plasma). Their models of the structure of both the argon atom and ion will be adopted and extended here. They also evaluated the role of atom-atom collisions in a C-R model [24], and concluded that, at atmospheric pressure, atom-atom collisions will play a role in the determination of the populations of the upper excited states for ionization fractions below 10^{-2}. In the cases of concern in this thesis, the electron temperature is high enough so that the influence of atom-atom collisions (which are characterized by the heavy particle temperature) is lower.

Braun and Kunc [11] used a three-level model to calculate steady-state overall collisional-radiative rate coefficients in nonequilibrium, partially ionized argon plasmas. They coupled the standard rate equations for the ground state, a lumped excited state, and the continuum to the Boltzmann equation for a self-consistent approach, over the electron temperature range $8000\ K < T_e < 25000\ K$ and the electron number density range of $10^{14}\ cm^{-3} < n_e < 10^{18}\ cm^{-3}$. They argue that the three-level argon model should be reasonable since three-level models for hydrogen have yielded fairly good results in the past. The same atomic model will be used here in this work for a three-level model (the lumped excited state of Braun and Kunc is the first lumped excited level in the argon atom model used here), except assuming that the electrons are Maxwellian. As Braun and Kunc state, however, and will be seen in chapter 3 of this thesis, neglecting the upper excited states will result in underestimating the overall recombination rate coefficient, particularly at low electron temperatures. They do point out that there is a great deal of uncertainty in the collisional rate coefficients involving the upper excited levels, which will add some uncertainty to the results of a multi-level model, and this must be kept in mind.

Owano and Kruger [52] recently published results of their research on the three-body collisional recombination coefficient of the argon atom. They conducted experiments on a flowing argon plasma in a 15 kW radio frequency inductively coupled plasma torch, using spectroscopic measurements to measure the electron-electron-ion three-body recombination rate. The spectroscopic measurements are used as a database for a two-dimensional axisymmetric computational code which takes into account various nonequilibrium effects, and from which the recombination rate coefficient is determined. These recombination coefficients compare well with those calculated by the approach described in chapter 3 of this thesis.

1.4.2 Inlet Ionization

Several researchers in the past have measured thin (mm-scale) ionization fronts in MPDT channel experiments. Other experiments have indicated that there are distinct differences in MPDT performance with different propellants, and attributed some of these differences to incomplete or delayed ionization. These observations suggest that there are significant, and species-related ionization initiation issues which influence performance, and for which there has been no full explanation to date. This section summarizes past research which is relevant to the problem of inlet ionization, which is the main focus of this thesis.

Experiments by Abramov, et al. [1] in 1968 used spectroscopic diagnostics and found a thin ionization front. The thickness of the front was much smaller than could be explained by the classical ionization length. Randolph, et al. [59], again using spectroscopic diagnostics, has recently found ionization fronts of a few millimeters. The calculated ionization length assuming Maxwellian electrons was found to be between one and three orders of magnitude larger than the measured value.

Toki, et al. [68] used a multi-channel MPDT to approximate an ideal two-dimensional discharge. This device allowed easy access to the discharge region for optical measurements with either argon or hydrogen as propellants. They measured delayed ionization with molecular hydrogen propellant and point out that there are some advantages to this behavior via what they describe as a situation resembling thermal pinch phenomenon in arcjet thrusters, except now there is significant additional thrust from the electromagnetic force. They also determined that anomalous ion excitation occurs in the discharge region in argon flows, lowering the efficiency.

Uematsu, et al. [69] tested a wide variety of molecular and atomic propellants for use in MPD thrusters: hydrogen, helium, neon, nitrogen, oxygen, argon, xenon, water, carbon dioxide, carbon monoxide, and ammonia. Experiments evaluated performance characteristics such as efficiency, thrust, erosion, and found three distinct groupings: atomic, molecular, and hydrogenous molecular propellants. Of particular significance to this thesis is the very low ionization fractions measured with molecular hydrogen injection (α, the ionization fraction, is the ratio of the electron density to the overall density of nuclei. With hydrogen propellant, they found $\alpha \approx 0.05$). They also suggest that the attractive thrust-to-power ratios found for the molecular gases may be due to the low ionization potential for molecular ions, and/or the recovery of their ionization energy through recombination.

Tahara, et al. [66] have reported results from experiments in a "one-dimensional" MPDT channel with several different propellants. They found that the current distribution depended strongly on the gas species injected, most importantly on whether the propellant is initially atomic (helium and argon were used) or molecular (hydrogen, nitrogen, and a hydrogen/nitrogen mix were used). Tahara, et al. posit that the ionization process of molecular species is slower than that of monatomic ones owing to the time lag for the dissociation process, especially at lower current levels. That is, ionization in molecular gases occurred further downstream and thus the current was more concentrated further downstream than for monatomic gases.

Experiments carried out by Heimerdinger and Kilfoyle [27], [36] have observed the detailed physics of self-field magnetoplasmadynamic (MPD) thrusters, and motivated this work. Based on these studies, we have a good idea of what the characteristics of the accelerator plasma are. At the exit, electron densities appear to range from $10^{20} m^{-3}$ and up, at high ionization fractions. While electron temperatures vary somewhat around an average of $12000K - 24000K$, there is evidence that the ion temperatures may range from well below the electron temperature, up to several electron volts [36]. Heimerdinger [27] also ran experiments with flared (expanding) channels, and noted that the initiation of ionization in the thrusters was difficult as the expansion was increased. An explanation of this will be developed in Chapter 4 of this thesis.

There have been several attempts to overcome the difficulties of modeling the ionization region in analytical and numerical models. More recently, work has focused on the structure of the ionizing zone or front measured in experiments.

The simplest way to model ionization is the hydrodynamic model, which applies when the diffusion-reaction scale length is much smaller than the characteristic flow scale and the reaction zone may be assumed as a front, as described in the case of combustion by Buckmaster [13]. Kuriki, et al. [39] treated the thin ionization front as a jump condition across a deflagration wave. The ionization fraction rises from essentially zero to one across this jump. While this method allows for consideration of the frozen flow energy loss due to the endothermic ionization process, it says nothing about the ionization front itself, its structure or its scale. Brushlinskii, et al. [12] used an "ignition switch" in a numerical model of plasmadynamic channel flow in quasistationary plasma accelerators. They argued that the equilibrium ionization fraction increases rapidly over a small temperature interval, so that a discontinuous change at some critical ionization temperature would be a reasonable simplification (if the parameters of the jump were chosen correctly). They identified two regimes for ionizing channels: a stationary regime, where there was a fixed ionization front, and a periodic regime, where the ionization front fluctuates. The regime was determined by the ratio of total current squared to mass flow rate (a higher value implied a more stationary front).

Numerical models of the thruster channel, such as those of Niewood in in one dimensional [50] and axisymmetric [51] geometries, may be forced to assume a "reasonable" inlet ionization fraction. This α must be large enough so that the ionizing rate at the inlet is not so small that ionization does not effectively occur within the thruster channel, and small enough not to conceal the effects of the ionization process and invalidate frozen loss calculations, for example. While this may be quite reasonable in the context of simulating the overall thruster, there is no way to pin down the inlet ionization fraction beyond bracketing it within a range of safe values, and no way to explain the ionization region. Other numerical models have either assumed equilibrium ionization [64], or a frozen, fully ionized plasma [40]. As discussed above, it is highly unlikely that either of these two ideal conditions are met in an MPDT.

Chouieri, et al. [17] [18] explain the thin ionization fronts found in Randolph's experiments [59] by anomalous ionization caused by plasma microturbulence. This produces a superthermal tail in the electron distribution that may increase the ionization coefficient, and therefore decrease the ionization length scale enough to produce mm-scale ionizing regions.

Their results do indicate that microturbulence may play a role in increasing the ionization coefficient, but their model is not self-consistent with respect to the overall thruster channel flow, using typical values of the inlet speed and number density taken from disparate experiments. Therefore, their results should be considered to be illustrative of a possible effect, but inconclusive in application to self-field MPDT inlet ionization.

Burton and Tiliakos [14] considered supersonic injection into a 1-D MPDT channel, and patched their model with a channel-flow solver. Their work looked at the details of the "preionization" region at constant bulk speed and varying electron temperature, and is somewhat similar to this work; however, in the supersonic case, back-diffusion does not play a significant role. They included a crude radiation model, but found that while radiation serves to start up the ionization process from very low ionization fractions (α less than about 10^{-6}) up to $\alpha \approx 10^{-5}$, ionization could not be supported solely by photoionization throughout the region. The preionization region was found to be a few mm long, and increased with decreasing density (increasing speed for fixed mass flow rate), indicating that collisional ionization must play a crucial role. However, the inlets of self-field MPDTs are not expected to be supersonic, per the calculations of Martinez [46], Niewood [50] [51] and Seals and Hassan [61]. The inlet ionization work carried out in this thesis will consider subsonic injection.

1.5 Approach to Solving the Inlet Ignition Problem

There are two steps taken in solving this problem. First, accurate ionization rate models for the gases of interest are developed, and then these rate models are applied to the inlet ignition problem.

A detailed finite-rate model is developed by adapting a kinetic approach, and applying it first to steady, stationary (i.e., discharge tubes) plasmas (hydrogen, argon atom, argon ion). This initial work has three purposes: to apply a known approach to ionization to the species of interest, to determine the population distribution of the excited levels of these species under a variety of conditions, and to calculate overall recombination coefficients based on these distributions.

The nonequilibrium ionization work presented here was motivated by interest in several issues relevant to plasma accelerators. Briefly, they are

- Ionization may be primarily due to multi-step processes in some regimes; most critically, in the low electron density/low electron temperature regime near the inlet.
- The results from detailed atom/ion models may be used to determine equivalent overall rate coefficients for ionization and three-body recombination. These models (specifically for the argon and hydrogen atoms and the argon ion) may be used in flow models.

The second part of this work considers back-diffusion of ion-electron pairs as an explanation for steady-state inlet ignition. This is explained through a series of 1-D analyses of increasing realism, which allow identification of the key parameters governing ignition and of their interplay in the complex phenomena near the inlet, under different assumed conditions. The ionization region itself will be assumed to be of constant area throughout.

The key hypothesis in this analysis will be that ion-electron pairs diffuse back towards the ion-attracting inlet wall, and that the back-diffused electrons are the drivers for ignition. This was inspired by and is similar to diffusion flames in combustion theory [76] [23], and unpremixed reaction-diffusion problems in general [58], in which diffusion provides the primary transport mechanism for and the mixing of the reactants necessary to sustain the reaction in steady-state.

The addition of back-diffusion in the problem increases the order by one and so requires a new boundary condition, which is that the electron-ion pairs pass through a pre-sheath heading towards the inlet, and that the ions enter a sheath (not modeled explicitly here) right at the inlet wall at the Bohm velocity, which is the classical result from sheath theory [16] [10].

1.6 Thesis Organization

Chapter 2 sets the stage for the the 1-D flow calculations for a self-field MPDT, introducing the equations of motion, and discussing several transport properties of significance to this work. An analysis which estimates the influence of radiation on the inlet ionization problem and on the rate equations in general follows.

The collisional-radiative model adopted here is presented in chapter 3. The standard collisional-radiative set of rate equations for a multi-level atom or ion is reformulated in such a way as to include the influence of the excited states on the overall ionization rate directly. The effect of radiation on the overall rate coefficients is also analyzed in a simple 3-level model. The final results most relevant to this work will be the calculated overall rate coefficients for various atoms and/or ions, which will be used in the ignition flow models of Chapter 4.

A series of numerical models are included in Chapter 4, covering constant speed and accelerating flows, constant and varying temperature flows and both atomic and molecular (dissociating) species injection.

Chapter 5 is a discussion of the results of this work, a summary of its conclusions, and recommendations for further work on the topics covered in this thesis.

Chapter 2

Steady-State One Dimensional Flow and Radiation Transfer

The dominant topic of interest here is the transition between the injected cold gas and the downstream plasma. The situation to be considered is that of injection through a porous backplate, which is essentially a 1-D flow. This chapter will first present the 1-D model equations of motion, then discuss some details and transport properties, and finally estimate the possible role of radiation in volumetric production. Figure 2.1 shows the configuration of a quasi-1-D self-field MPDT, with the x-axis in the axial direction and the transverse y-axis starting at a position halfway between the anode and cathode. Here, B is the magnetic field, j is the current density, H is the interelectrode gap, and L is the channel length. This is actually a quasi-1-D model, since transverse ambipolar diffusion to the walls will be included. Quasi-1-D models for self-field MPDTs have been developed in the past by many researchers. [46] [37] [50]

2.1 Equations of Motion

The flow is assumed to be inviscid, and transverse heat conduction and magnetic diffusion are neglected. However, transverse ambipolar diffusion is retained, which may play an important role at low densities, as observed in Niewood's 1-D MPDT channel computations [50], the analysis of Heimerdinger [27], and as will be shown in Chapter 4 of this thesis.

The steady-state quasi-one-dimensional equations of motion for a nonequilibrium plasma

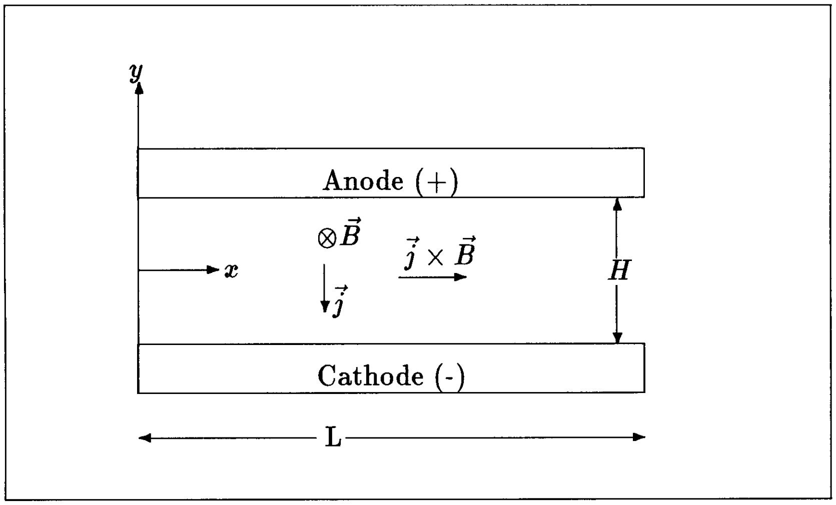

Figure 2.1: Constant area MPDT channel

are: overall continuity, electron continuity, overall momentum, electron energy, heavy species energy, and a magnetic field equation [50] [53] [46]. In addition, it is assumed that the ionization front is in a constant area channel, or at least that area variation effects are negligible.

The overall conservation of mass equation is, with n_g representing the total number density of nuclei, and u the average or bulk velocity:

$$\frac{dun_g}{dx} = 0 \tag{2.1}$$

The ion (or electron) continuity equation is:

$$\frac{\partial un_e}{\partial x} - \frac{\partial}{\partial x}(D_a\frac{\partial n_e}{\partial x}) - \frac{\partial}{\partial y}(D_a\frac{\partial n_e}{\partial y}) = \dot{n}_e \tag{2.2}$$

where n_e is the number density of electrons (and ions too, if there are only first ions present), D_a is the ambipolar diffusion coefficient, and $\dot{n}_e$ is the volumetric production rate of ions, via collisions and/or radiative effects.

The overall momentum equation, neglecting friction, is:

$$\frac{dn_gu^2}{dx} = -\frac{dp}{dx} + \vec{j}\times\vec{B} \tag{2.3}$$

where p is the gasdynamic pressure, B is the azimuthal (induced) magnetic field,$\vec{j}$ is the current density, and $\vec{j}\times\vec{B}$ is the Lorenz force.

The electron energy equation, neglecting electron-heavy energy transfer, friction, transverse heat conduction, and radiative loss, is

$$\frac{3}{2}k_B\frac{dn_g u\alpha T_e}{dx} = -\frac{d}{dx}\left(K_e\frac{dT_e}{dx}\right) + \frac{j^2}{\sigma} - E_{ac}\dot{n}_e \tag{2.4}$$

where the T_e is the electron temperature, k_B is Boltzmann's constant, $\alpha = n_e/n_g$ is the ionization fraction, K_e is the electron heat conduction coefficient, j is the current density, σ is the electron electrical conductivity, and E_{ac} is the magnitude of the energy gap between the ground state of the atom and the ion.

The heavy particle energy equation, neglecting electron-heavy energy transfer, friction, and transverse heat conduction, is replaced with the assumption that $T_g \approx$ constant.

The following steady-state Maxwell's equations are also used (the magnetoquasistatic form [47]):

$$\nabla \times \vec{E} = 0 \tag{2.5}$$

$$\mu_o\vec{j} = \nabla \times \vec{B} \tag{2.6}$$

$$\nabla \cdot \vec{B} = 0 \tag{2.7}$$

from which the following magnetic field equation can be arrived at, which neglects transverse magnetic diffusion:

$$\frac{\partial B}{\partial t} + \frac{\partial uB}{\partial x} = \frac{\partial}{\partial x}\left(\frac{1}{\mu_o\sigma}\frac{\partial B}{\partial x}\right) \tag{2.8}$$

The pressure, from $p = \sum_s n_s k_B T_s$, for a two temperature plasma is

$$p = \frac{\rho}{m_i}k_B[(1+\alpha)T_g + \alpha T_e] \tag{2.9}$$

where $\rho = m_i n_g$ is the mass density and m_i is the nuclei mass.

A generalized Ohm's law is also used. Derivation of this expression and the definition of β, the Hall parameter, are given in section 2.1.1.

2.1.1 Details of the Equations of Motion

Here, some of the physics of the flow is analyzed. First, the generalized Ohm's law is derived, then the Lorenz force term in the momentum equation is used to define a "magnetic pressure". Finally, the electrodynamic power term in the energy equation is used to identify an important non-dimensional parameter, the magnetic Reynolds number.

Generalized Ohm's Law - Hall Effects

The generalized Ohm's Law is derived from the electron species-momentum equation, after dropping the electron inertia terms (assuming that electrons carry very little momentum due to their mass). If subscript r designates all other species, then the force density balance for the electrons is:

electrostatic force + Lorenz force + pressure force = collisional friction force(s)

or:

$$en_e\vec{E}' + en_e\vec{v}_e \times \vec{B} + \nabla p_e = \sum_r m_e n_e \nu_{er}(\vec{v}_r - \vec{v}_e)$$

Where $\vec{E}'$ is the electric field in the moving frame:

$$\vec{E}' = \vec{E} + \vec{v} \times \vec{B}$$

and ν_{er} is the total collisional frequency between electrons and all other species, r.

Now, if the other species are heavy enough so that $|\vec{v}_r| \ll |\vec{v}_e|$, then $\vec{j} = -en_e\vec{v}_e$, and the electron momentum equation becomes:

$$en_e\vec{E}' - \vec{j} \times \vec{B} + \nabla P_e = \frac{m_e}{e}\nu_e\vec{j}$$

or

$$\vec{j} + \vec{j} \times \vec{\beta} = \sigma\vec{E}' - \frac{1}{en_e}\nabla P_e \tag{2.10}$$

Where σ is the DC scalar conductivity,

$$\sigma = \frac{e^2 n_e}{m_e \nu_e} \tag{2.11}$$

$|\vec{\beta}| = \beta = \frac{eB}{m_e\nu_{er}}$ = the Hall parameter.

Note that $\frac{eB}{m_e} = \omega_c$ is the cyclotron or gyro frequency, so that $\beta = \frac{\omega_c}{\nu_{er}}$ (which is dimensionless). Thus the Hall parameter is the number of Larmor cycles (in radians) between collisions. For $\omega_c \ll \nu_{er}$ the Hall effects are negligible - in a highly collisional plasma, the cyclotron motion is arrested as electrons experience many collisions per cycle.

The Momentum Equation; Magnetic Pressure

The Lorenz force term in the momentum equation (eq. 2.3) may be simplified as follows:

$$\vec{j} \times \vec{B} = \frac{1}{\mu_o}(\nabla \times \vec{B}) \times \vec{B}$$

$$= \frac{1}{\mu_o}[(\vec{B} \cdot \nabla)\vec{B} - \frac{1}{2}\nabla B^2]$$

Now, if the plasma flow is assumed to be two-dimensional, the currents are constrained to cylindrically longitudinal planes. This requires that $\vec{B} = B_\theta \hat{e}_\theta$, where $\hat{e}_\theta$ is the azimuthal unit vector and that the first term in the last expression above is zero in the 2-D case. Neglecting viscous effects, the one-fluid axial momentum equation 2.3 may be written in 1-D as:

$$\frac{dn_g m_i u^2}{dx} + \frac{d}{dx}\left[p + \frac{B^2}{2\mu_o}\right] = 0 \tag{2.12}$$

The quantity $\frac{B^2}{2\mu_o}$ appears in the same manner as the pressure, prompting its being referred to as the magnetic pressure. In most MPD thrusters, this is significantly larger than the gasdynamic pressure. However, normal pressure effects are not small at the inlet and exit, where the gradients may be comparable to the magnetic field gradients.

The Energy Equation; The Magnetic Reynolds Number

The $\vec{E} \cdot \vec{j}$ term drives the energy equation - the only energy added to the plasma comes from this electrodynamic power. A useful non-dimensional ratio may be found by expanding this term.

Using equation 2.10 to solve for $\vec{E}$ (neglecting electron pressure effects):

$$\vec{E} = \frac{\vec{j}}{\sigma} - \vec{v} \times \vec{B} + \frac{\vec{j} \times \vec{\beta}}{\sigma}$$

Then:

$$\vec{E}\cdot\vec{j} = \frac{\vec{j}\cdot\vec{j}}{\sigma} - \vec{j}\cdot(\vec{v}\times\vec{B}) + \vec{j}\cdot\frac{\vec{j}\times\vec{\beta}}{\sigma}$$

$$= \frac{j^2}{\sigma} + \vec{v}\cdot(\vec{j}\times\vec{B})$$

= rate of ohmic heating + rate at which useful (thrust) work is done.

Comparing these two terms yields a meaningful parameter, the magnetic Reynolds number (R_m). The last equation is used for the ratio, and an order-of-magnitude analysis is carried out:

$$\frac{useful\ work}{ohmic\ heating} = R_m \sim \frac{vjB}{\frac{j^2}{\sigma}}$$

and using $j \sim \frac{B}{L\mu_o}$ from equation 2.6,

$$R_m = \mu_o \sigma v L \tag{2.13}$$

where v and L are appropriate characteristic speed (generally based on the axial flow) and length scale, respectively.

Note that, for effective performance as a thruster, $R_m \gg 1$. Large R_m may result from a combination of large conductivity (σ), and axial Lorenz force (assuming that the bulk of the flow is always axial). Small R_m can be attributed to low conductivity or a short channel. The Magnetic Reynolds Number is also equal to the ratio of convection of the magnetic field to its diffusion in the magnetic field equation (1-D, equation 2.8):

$$R_m = \frac{\sigma\nabla[uB]}{\frac{1}{\mu_o}\frac{d^2B}{dx^2}}$$

Using the definition of the characteristic time scale of magnetic diffusion from Melcher [47], $\tau_m = \mu\sigma L^2$, the magnetic Reynolds number can also be seen as:

$$R_m = \frac{\tau_m}{\tau_c}$$

Here, τ_c is the characteristic time scale of the bulk plasma's passage through the channel, $\tau_c = \frac{L}{v}$.

2.2 Diffusion

2.2.1 Streamwise Ion-Neutral Slip

The streamwise slip of ions plays an important role in this work, so some care is taken in evaluating it. Since ions are being directly accelerated while the neutrals are accelerated by collisions with ions, there are actually two effects (acceleration and density gradients) leading to ion-neutral slip. This section will develop an alternative to Fick's Law applicable to the inlet ignition model.

Starting with the 1-dimensional neutral momentum equation, in which electron-neutral collisional forces are neglected compared to ion-neutral forces,

$$m_i n_n v_n \frac{dv_n}{dx} = -\frac{dp_n}{dx} + m_i n_n n_e \bar{c}_{in} Q_{in} (V_i - V_n) \tag{2.14}$$

where n_n is the number density of neutrals, the species velocity of the neutrals is v_n, and the slip velocities of the neutrals and ions are, respectively, V_n and V_i. The ion-neutral thermal velocity is $\bar{c}_{in}$, and the ion-neutral momentum transfer cross-section is Q_{in}. We assume that $|v_n - u| = |V_n| \ll u$ everywhere, so that

$$n_n v_n \frac{dv_n}{dx} \approx n_n u \frac{du}{dx}$$

Overall mass continuity requires that $n_n V_n + n_e V_i = 0$, and the neutral pressure is

$$p_n = k_B n_n T_g$$

With constant T_g, we can rewrite equation 2.14 as:

$$m_i n_n u \frac{du}{dx} = -k_B T_g \frac{dn_n}{dx} + m_i n_g n_e \bar{c}_{in} Q_{in} V_i \tag{2.15}$$

where $n_g = n_e + n_n$ is the number density of the heavy particles. Solving for $n_e V_i$, the ion slip flux,

$$n_e V_i = \frac{1}{n_g \bar{c}_{in} Q_{in}} \left(n_n u \frac{du}{dx} + \frac{k_B T_g}{m_i} \frac{dn_n}{dx} \right) \tag{2.16}$$

If we use the ambipolar diffusion coefficient [49], which has units of m^2/s:

$$D_a = \frac{k_B (T_e + T_g)}{m_i \bar{c}_{in} Q_{in} n_g} = (1 + \frac{T_e}{T_g}) \sqrt{\frac{\pi k_B T_g}{m_i}} \frac{1}{2 Q_{in} n_g} \tag{2.17}$$

as well as the definition of the Bohm velocity:

$$v_B = \sqrt{\frac{k_B(T_e + T_g)}{m_i}} \tag{2.18}$$

then equation 2.16 can be recast as:

$$n_e V_i = D_a \left(\frac{n_n u}{v_B^2} \frac{du}{dx} + \theta \frac{dn_n}{dx} \right) \tag{2.19}$$

where the parameter θ has been defined:

$$\theta \equiv \frac{T_H}{T_e + T_H} \tag{2.20}$$

If we assume that the acceleration term is negligible and that there is no total pressure gradient, then

$$\theta \frac{dn_n}{dx} = -\frac{dn_e}{dx}$$

and Fick's law results:

$$(n_e V_i)_F = -D_a \frac{dn_e}{dx} = -D_a n_g \frac{d\alpha}{dx} = -C_a \frac{d\alpha}{dx} \tag{2.21}$$

where n_g has been assumed to be constant.

However, retaining the inertia term and making no assumption about the total pressure gradient is more realistic, especially due to the large acceleration present in the inlet region. In this case, using the overall continuity equation (2.1), and the definition of the ionization fraction,

$$\alpha \equiv \frac{n_e}{n_g}$$

in 2.19, then the general expression for streamwise ion-neutral slip is

$$n_e V_i = D_a n_g \theta \left((1 - \alpha)(\frac{u^2}{\theta v_B^2} - 1) \frac{1}{u} \frac{du}{dx} - \frac{d\alpha}{dx} \right) \tag{2.22}$$

Note that, for this alternative formulation, acceleration with α constant at $u < \sqrt{\theta} v_B$ yields backward ion diffusion (relative to the flow) - the neutrals are moving forward at a faster speed than the ions due to the pressure gradient which provides the acceleration. In this regime, the slip is gradient dominated. Acceleration at $u > \sqrt{\theta} v_B$ means that the ions are moving faster than the neutrals, and slip is inertia dominated. (Note that $\sqrt{\theta} v_B = \sqrt{\frac{p_g}{m_i n_g}}$ is roughly the heavy particle thermal speed.)

The ambipolar diffusion coefficient can also be expressed as

$$D_a = \frac{C_a}{n_g}$$

where $C_a = D_a n_g$ is a function of temperature only. Using the form for D_a in equation 2.17, C_a for the argon atom is

$$C_a = 1.274 \times 10^{19} \left(1 + \frac{T_e}{T_g}\right) \sqrt{T_g} (m^{-1} s^{-1})$$

Note that C_a is a fairly weak function of temperature, particularly in comparison with the collisional rate coefficients, which may vary exponentially with T_e.

From the Fick's Law form, and the ion continuity equation, one can set up a balance between convection and axial diffusion to find the characteristic length scale for axial back-diffusion:

$$\frac{du n_e}{dx} \approx \frac{d}{dx} D_a \frac{dn_e}{dx}$$

$$l_D = \frac{D_a}{u_{ref}} = \frac{C_a}{G}$$

2.2.2 Accounting for Transverse Diffusion

In this section, the transverse diffusion of particles is taken into account in a channel of height H. This addition to the quasi-1-D model is necessary to strike a balance far downstream in the continuity equations. Particles may be lost to the walls via transverse diffusion and catalytic walls.

The origin of the y-axis will be the middle of the channel, so that $y = \pm H/2$ represents the walls. Assuming a parabolic distribution across the channel, the loss rate is uniform, since the diffusion rate term is a second order derivative. As in Niewood [50], the profile of particle densities for particles of type k (where k may represent an excited state, or ion, and $n_k(x)$ is the average density of level k across the channel.) is then

$$n_k(y, x) = \frac{3}{2} n_k(x) \left[1 - \left(\frac{2y}{H}\right)^2\right]$$

so that the diffusion loss rate for a level k, for an assumed parabolic transverse density distribution,

$$D_k \frac{\partial^2 n_k}{\partial y^2} = \frac{12 D_k n_k}{H^2}$$

or, using $h = H/\sqrt{12}$,

$$D_k \frac{\partial^2 n_k}{\partial y^2} = \frac{D_k n_k}{h^2}$$

The excited state diffusion coefficients are:

$$D_k = \sqrt{\frac{\pi k_B T_g}{m_i}} \frac{1}{2 Q_{jk} \sum_{j \neq k} n_j}$$

For the case of ambipolar loss (coupled diffusion of electrons and ions), we assume ion-attracting walls, a uniform loss rate (again a parabolic density profile), and require that at the edge of the sheath, the ions stream into the sheath at the Bohm velocity, or

$$n_e v_B = -D_a \frac{\partial d n_e}{\partial d y} \tag{2.23}$$

where $v_B = \sqrt{\frac{k_B(T_e+T_g)}{m_i}}$ is the Bohm velocity and the ambipolar diffusion coefficient, D_a, is defined in equation 2.17.

Assuming again that the transverse distribution is parabolic,

$$n_e(y,x) = Ay^2 + By + C \tag{2.24}$$

and subject to equation 2.23, plus a symmetry condition, which sets $B = 0$, and the condition that the average density across the channel is $n_e(x)$:

$$n_e(x) = \frac{1}{H} \int_{-H/2}^{H/2} n_e(y,x) dy$$

These conditions applied to equation 2.24 result in the following two equations for the two remaining unknowns, A and C:

$$n_e(x) = \frac{H^2}{12} A + C$$

and

$$\left[\frac{H^2}{4} A + C \right] v_B = -D_a H A$$

The rate of ambipolar loss, denoted here as $\mathcal{R}$, is

$$\mathcal{R} = -D_a \frac{\partial^2 n_e}{\partial y^2} = -2 D_a A$$

and, solving for A, and substituting, this is

$$\mathcal{R} = \frac{\frac{12 D_a n_e}{H^2}}{1 + \frac{6 D_a}{v_B H}} \tag{2.25}$$

Two regimes are identifiable here - one constrained by the diffusion rate and one constrained by the rate that ions stream into the sheath. Looking at the variable term in the denominator,

$$\frac{6 D_a}{v_B H} = \frac{3\sqrt{\pi}\left(\sqrt{\frac{T_e}{T_g}} + \sqrt{\frac{T_g}{T_e}}\right)}{H n_g Q_{in}}$$

Since $D_a \propto 1/n_g$, the quantity $(H\mathcal{R}/n_e)$ is a function of $H n_g$, and, more weakly, $\frac{T_e}{T_g}$, and T_g. For $\frac{T_e}{T_g} \approx O(1)$, and using $Q_{in} \approx 1.4 \times 10^{-18} m^2$ for argon [44], $\frac{6D_a}{v_B H}$ is unity when $H n_g \approx 10^{19} m^{-2}$.

The ion loss will be direct to the walls for $H n_g Q_{in} \ll 1$, and limited by diffusion (i-n collisions) at high values. Most cases of interest for plasma accelerators are near the transition point, $H n_g \approx 10^{19} m^{-2}$.

The nondimensional form of $H\mathcal{R}/n_e$ is

$$\frac{H\mathcal{R}}{n_e \sqrt{\frac{\pi}{m_i} k_B T_e}} = \frac{\frac{12}{H n_g Q_{in}}}{1 + \frac{6\sqrt{\pi}}{H n_g Q_{in}}} \tag{2.26}$$

Figure 2.2 is a plot of equation 2.26 as a function of $H n_g Q_{in}$. This shows that assuming diffusion only is reasonable down to roughly $H n_g Q_{in} \approx 1.0$ to stay within a factor of two with the overall rate, which is a reasonable approximation for this work.

2.3 Collisional and Transport Processes

Ionization/recombination and excitation/deexcitation inelastic collisions will be covered in detail in chapter 3. In this section, some of the other collisional and, in particular, transport processes of interest to this work are discussed.

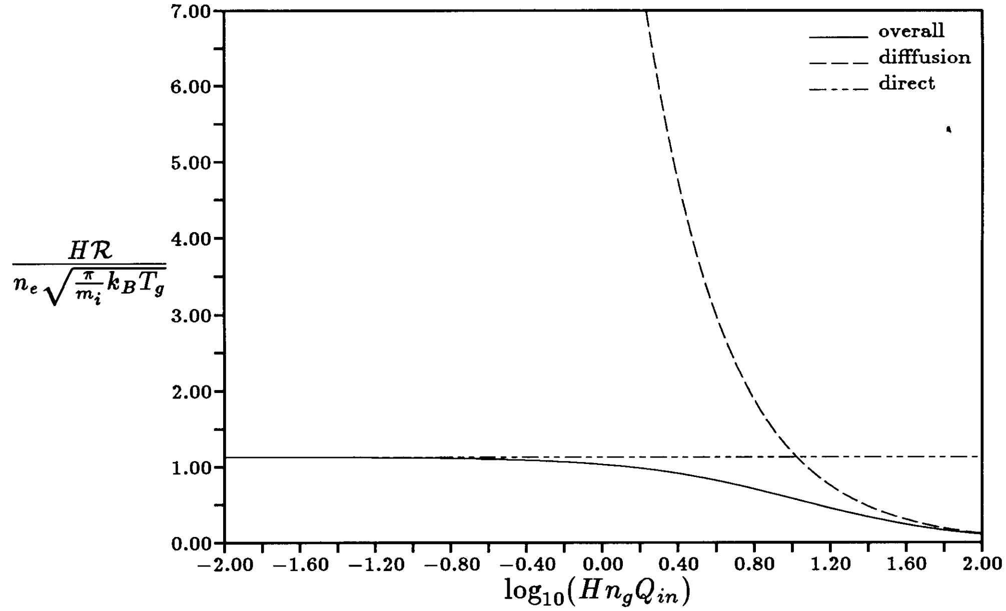

Figure 2.2: Nondimensionalized $H\mathcal{R}/n_e$ showing the regions where direct ion loss and diffusion dominate the ambipolar loss rate to the walls.

2.3.1 Electron Electrical Conductivity

The electron electrical conductivity as defined in equation 2.11 may vary as a function of both the electron temperature and the ionization fraction. This behavior is seen by recalling that the DC conductivity [10] is

$$\sigma = \frac{n_e e^2}{m_e \nu_e}$$

$$\begin{aligned} \nu_e &= \nu_{ei} + \nu_{en} \\ &= n_i Q_{ei} \bar{c}_e + n_n Q_{en} \bar{c}_e \end{aligned}$$

where n_i is the number density of ions and n_n is the neutral particle density, and $\bar{c}_e$ is the electron thermal speed (T_e in degrees Kelvin):

$$\bar{c}_e = \sqrt{\frac{8}{\pi}\frac{k_BT_e}{m_e}} = 6211\sqrt{T_e}\ \frac{m}{s}$$

Here, Q_{ei} is the Coulombic electron-ion collision cross-section [44] [60]

$$Q_{ei} = \frac{e^4 \ln\Lambda}{32\pi\epsilon_o^2(k_BT_e)^2}$$

where the nondimensional variable, Λ using mks units, and temperatures in K is

$$\Lambda = 1.24 \times 10^7 \sqrt{\frac{T_e^3}{n_e}}$$

where n_e is the number density of electrons, and the electron temperature is T_e, in K. Also, ϵ_o is the permittivity constant, and k_B is Boltzmann's constant.

The electron-neutral momentum cross-section for argon in the temperature range of the first argon ion from Liberman and Velikovich [44] is

$$Q_{en}^{LV} = [-0.488 + 3.96 \times 10^{-4} T_e] \times 10^{-20}\ m^2$$

Bittencourt [10] reports a species-independent electron-neutral cross section of

$$Q_{en}^{B} = 4.186 \times 10^{-24} T_e\ \ m^2$$

which is within 25 % of Q_{en}^{LV} at $T_e = 5000K$, and better at higher temperatures, and will be used here.

The electron-ion (Coulombic) collisional rate for the argon atom, from Bittencourt [10], is then:

$$\nu_{ei} = 3.62 \times 10^{-6} n_i T_e^{-3/2} \ln \Lambda\ \ s^{-1}$$

and the electron-neutral collisional rate for the argon atom, also from Bittencourt [10], is:

$$\nu_{en} = 2.60 \times 10^{-16} n_n T_e^{1/2}\ \ s^{-1}$$

so that the DC conductivity

$$\sigma = \frac{e^2}{m_e} \frac{n_e}{3.62 \times 10^{-6} \ln \Lambda n_i T_e^{-3/2} + 2.60 \times 10^{-16} n_n T_e^{1/2}}$$

or, assuming that $\ln \Lambda \approx 10$ and using the ionization fraction, $\alpha \equiv n_e/n_g$,

$$\sigma = \frac{A\alpha}{B(1-\alpha)T_e^{\frac{1}{2}} + D\alpha T_e^{-\frac{3}{2}}}$$

with $A = 2.81 \times 10^{-8}$, $B = 2.6 \times 10^{-16}$, $D = 3.62 \times 10^{-5}$ for the argon atom. Figure 2.3 shows the electrical conductivity of argon for equilibrium ionization.

If the temperature is constant, then a reference conductivity can be calculated at the high α end: $\sigma_{ref} \equiv \frac{A}{D} T_e^{\frac{3}{2}}$, and we can write

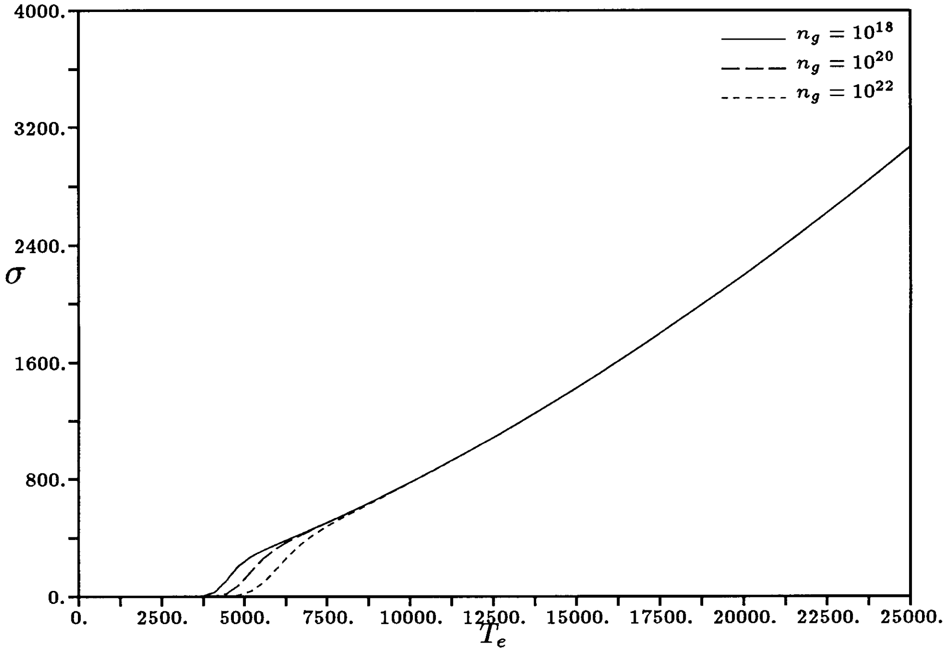

Figure 2.3: Argon electrical conductivity (si/m) vs electron temperature (at equilibrium ionization fraction). The densities are in m^{-3}. Note that the density variation due to variations of $\ln \Lambda$ are ignored in this calculation.

$$\frac{\sigma}{\sigma_{ref}} = \frac{\alpha}{\alpha\tau^{-3/2} + (1-\alpha)q\tau^{1/2}} = \frac{1}{\tau^{-3/2} + (\frac{1}{\alpha} - 1)q\tau^{1/2}} \tag{2.27}$$

where T_{ref} is a reference temperature, and $\tau = T_e/T_{ref}$ is the nondimensional electron temperature, and q is:

$$q = \frac{B}{D}T_{ref}^2 = 7.2 \times 10^{-12}T_{ref}^2$$

The parameter q is roughly the minimum ionization fraction for Coulomb collision dominance at T_{ref}, and q is generally of order 10^{-3}. The reference conductivity would be approximately 1000 to 2000 Si.

2.3.2 Electron Heat Conduction

The rates for ionization and recombination in a plasma are strongly dependent on the electron temperature. Comparison of the characteristic diffusion scale length, which is effectively the scale for the ionizing region, per results of the analysis in Chapter 4, to the heat conduction scale length results in a parameter which gauges whether temperature can be safely assumed to be fixed in the ionizing region, which would simplify the analysis. This is the Lewis number [13]:

$$Le = \frac{3}{2}\frac{k_B n_{ref} D_a}{K_e} = \frac{l_D}{l_{cond}}$$

The thermal conductivity for a plasma [49] (with no magnetic field, or only along the magnetic field, and including only the electronic contribution and Coulombic scattering) is:

$$K_e = \frac{1.7142 k_B^2 T_e \sigma}{e^2}$$

so that the Lewis number, with $n_{ref} \approx n_g$, becomes

$$L_e = \frac{3/2e^2}{1.7142k_B A}\frac{C_a[B(1-\alpha)T_e^{1/2} + DT_e^{-3/2}]}{\alpha}T_e$$

or

$$L_e = 9.628 \times 10^{-8}C_a[B(\frac{1}{\alpha} - 1)T_e^{-1/2} + DT_e^{-5/2}] \tag{2.28}$$

so that $L_e = L_e(T_e, T_H, \alpha)$ (and the α dependence only appears at low α). (Note: the constants A, B and D are the same ones used in the previous subsection on conductivity.)

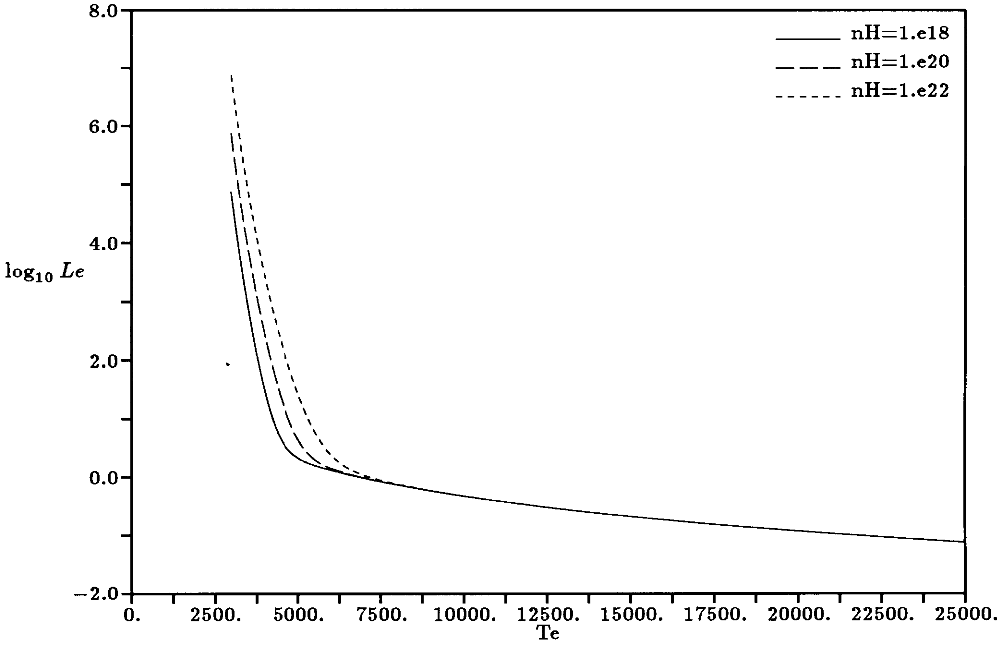

Figure 2.4: Lewis number vs T_e, for argon, with equilibrium ionization fraction.

Here $C_a = D_a n_g$. Figure 2.4 is a plot of Le vs electron temperature. The abrupt rise in Le at lower T_e is not realistic, and is due to the fact that only the electronic contribution to K_e is included in equation 2.28 and there are few electrons available at low temperatures. Note that Le drops with T_e. This is because K_e rises with T_e faster than C_a does.

The Lewis number is the ratio of the diffusion length scale to the electron thermal conduction length scale. Low Lewis numbers then imply that the electron temperature varies on a scale much longer than the diffusion scale, so that it is effectively frozen on the diffusive scale. Since the results of the analyses of Chapter 4 indicate that successful ignition occurs when the ionization length scale is on the order of the diffusion length, this means that zero Le (infinite K_e) implies a constant temperature ionizing region. For“typical” MPD thruster conditions, $Le \approx O(10^{-1})$, which implies that electron temperature variation on the ionizing region length scale is likely to be small.

2.4 Radiation Transfer in a Nonequilibrium Plasma

Although the emphasis in this thesis is on collisional production of ions, direct photoionization and photoexcitation may play roles. In order to estimate the possible effects of radiation on ionization at the inlet of an MPD thruster, some details of radiative transfer must be considered. The basics of the radiative transfer formulation to be used in this research as well as some preliminary calculations and estimates are presented in the following, and then estimates of the radiative scale lengths are made to justify neglecting radiation under the conditions typically found in a magnetoplasmadynamic thruster. Radiation will therefore not be included in the ignition models of Chapter 4. A standard parametric method of treating radiation, using radiative escape factors, will be outlined, and used in in Chapter 3 to estimate what effects radiation could have on the population distribution of the excited states of an atom and the overall ionization and recombination rate coefficients.

Radiation in a plasma may be produced by spontaneous or stimulated emission and depleted via absorption in processes involving the ground state, the excited states, and the ion. The loss or gain of energy of one of the states of an atom or ion is associated with a change in electronic state. In this section, estimates of the effects of radiation on the volumetric rates of interest to this work are outlined.

Figure 2.5, from Samaras [60] illustrates the definition of the specific intensity of radiation, I_ν, which is: [53], [60]

$$I_\nu = \lim_{dA,\, d\Omega,\, dt,\, d\nu \to 0} \left(\frac{dE_\nu}{dA \ \cos\theta \ d\Omega \ dt \ d\nu} \right)$$

where dE_ν is the total amount of radiant energy in the frequency range between ν and $\nu + d\nu$, passing through the element of surface area dA and in a direction confined to an element of solid angle $d\Omega$ during an element of time dt. The angle θ is the angle of the direction of radiation (unit vector s^1) with the outward normal to the surface A (unit vector A^1), so that $dA \cos\theta$ is the area element perpendicular to the ray considered. The dimensions for the specific intensity are joules/(m^2 steradian).

The specific intensity is governed by the radiative transfer equation, which states that the rate of change of the intensity with respect to space is due to the following three processes (written in terms of the Einstein coefficients, A_{nm}, B_{nm} and B_{mn}, to be discussed further below):

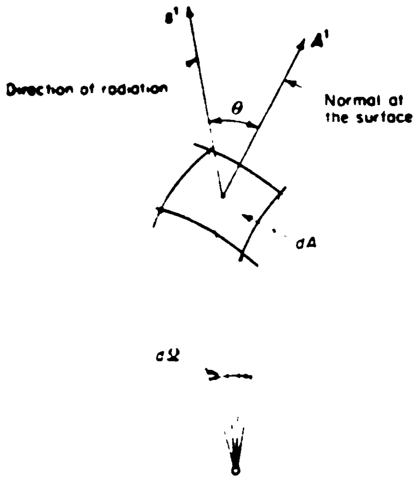

Figure 2.5: Geometry of radiation flow. From Samaras.

- radiation produced by spontaneous radiative decay of level n down to level m: $E_{nm} n_n \frac{A_{nm}}{4\pi} \phi(\nu)$
- radiation produced by stimulated emission of the transition $n \rightarrow m$ (typically a small effect, except in lasers): $E_{nm} n_n B_{nm} \phi(\nu) I_{nm}$
- radiation absorbed at level m and resulting in an $m \rightarrow n$ excitation: $E_{nm} n_m B_{mn} I_{nm} \phi(\nu)$

Where $\phi(\nu)$ is a shape factor, with units $1/\nu$, and assumed here to be the same for each of the three processes outlined above. The steady-state radiation transfer equation written in terms of the Einstein factors is then (for each line $n > m$):

$$\vec{\Omega} \cdot \nabla I_{\nu_{nm}} = [E_{nm} n_n \frac{A_{nm}}{4\pi} + E_{nm}(n_n B_{nm} - n_m B_{mn}) I_{\nu_{nm}}]\phi(\nu) \tag{2.29}$$

The three Einstein coefficients are related by the following two constraints [49] which are required by equilibrium balance [49]:

$$A_{nm} = \frac{8\pi h \nu_{nm}^3}{c^2} B_{nm} \tag{2.30}$$

and

$$B_{nm} g_n = B_{mn} g_m \tag{2.31}$$

The radiation transition probabilities for spontaneous emission, A_{lk}, A_{ck}, can be found tabulated [75] [35].

The following is the typical radiation transfer formulation [53], except for the application to nonequilibrium level populations. Equation 2.29 can be rewritten as:

$$\vec{\Omega} \cdot \nabla I_{\nu_{nm}} = E_{nm} B_{mn} \phi(\nu) \left[n_n \frac{g_m}{g_n} \frac{2h\nu_{nm}^3}{c^2} + \left(n_n \frac{g_m}{g_n} - n_m \right) I_{\nu_{nm}} \right] \tag{2.32}$$

At complete thermal equilibrium, the excited levels are populated according to a Maxwell-Boltzmann distribution:

$$\frac{n_m^*}{n_n^*} = \frac{g_m}{g_n} \exp\left(\frac{h\nu_{nm}}{k_B T_e} \right) \tag{2.33}$$

where the superscript $*$ denotes an equilibrium value. Also, there is perfect balance between photon emission and absorption (the righthand side of equation 2.32 is zero). Then

$$0 = n_n^* \frac{g_m}{g_n} \frac{2h\nu_{nm}^3}{c^2} + \left(n_n^* \frac{g_m}{g_n} - n_m^* \right) I_{\nu_{nm}}$$

or

$$I_{\nu_{nm}} = \frac{\frac{2h\nu_{nm}^3}{c^2}}{\exp(\frac{h\nu_{nm}}{k_B T_e}) - 1} \equiv B_{\nu_{nm}} \tag{2.34}$$

which is black-body radiation intensity, and $B_{\nu_{nm}}$ is Planck's radiation function.

Now the radiation transfer equation, equation 2.32 may be rewritten. First, the absorber density n_m is pulled out as a common factor,

$$\vec{\Omega} \cdot \nabla I_{\nu_{nm}} = n_m E_{nm} B_{mn} \phi(\nu) \left[\frac{n_n}{n_m} \frac{g_m}{g_n} \frac{2h\nu_{nm}^3}{c^2} + \left(\frac{n_n}{n_m} \frac{g_m}{g_n} - 1 \right) I_{\nu_{nm}} \right]$$

where the term outside the brackets on the righthand side is the absorption coefficient, defined as

$$k_\nu \equiv n_m E_{nm} B_{mn} \phi(\nu) \tag{2.35}$$

Then the equilibrium distribution (equation 2.33) can be used to obtain

$$\vec{\Omega} \cdot \nabla I_{\nu_{nm}} = k_\nu \left[\frac{n_n}{n_n^*} \frac{n_m^*}{n_m} \exp(\frac{-h\nu_{nm}}{k_B T_e}) \frac{2h\nu_{nm}^3}{c^2} + \left(\frac{n_n}{n_n^*} \frac{n_m^*}{n_m} \exp(\frac{-h\nu_{nm}}{k_B T_e}) - 1 \right) I_{\nu_{nm}} \right]$$

Stimulated radiation is insignificant whenever

$$\frac{n_n}{n_n^*}\frac{n_m^*}{n_m}\exp(\frac{-h\nu_{nm}}{k_BT_e}) \ll 1$$

which is a reasonable assumption for most lines, particularly the strong resonant lines (where the lower, absorbing level is the ground state). Therefore, stimulated radiation will not be considered anymore in this work.

A modified, nonequilibrium production term, $\tilde{B}_{\nu_{nm}}$ can be defined as

$$\tilde{B}_{\nu_{nm}} \equiv \frac{n_n}{n_n^*}\frac{n_m^*}{n_m}\exp(\frac{-h\nu_{nm}}{k_BT_e})\frac{2h\nu_{nm}^3}{c^2} \tag{2.36}$$

or, in terms of the Planck radiation function,

$$\tilde{B}_{\nu_{nm}} = \frac{n_n}{n_n^*}\frac{n_m^*}{n_m}\left(\frac{\exp(\frac{h\nu_{nm}}{k_BT_e})-1}{\exp(\frac{h\nu_{nm}}{k_BT_e})}\right)B_{\nu_{nm}}$$

If $\exp(\frac{h\nu_{nm}}{k_BT_e}) \gg 1$, then

$$\tilde{B}_{\nu_{nm}} \approx \frac{n_n}{n_n^*}\frac{n_m^*}{n_m}B_{\nu_{nm}}$$

Then the equation of radiation transfer (equation 2.32) may be rewritten as

$$\vec{\Omega}\cdot\nabla I_{\nu_{nm}} = k_\nu(\tilde{B}_\nu - I_{\nu_{nm}}) \tag{2.37}$$

where $\mu = \frac{1}{\cos\theta}$ carries the angular direction information, and $k_\nu \equiv E_{mn}B_{mn}n_m\phi(\nu)$ is the absorption coefficient for the line nm.

2.4.1 Photon Mean Free Paths

From inspection of the nonequilibrium radiation transfer equation (equation 2.37), the mean-free path (mfp) for radiation is $\lambda_\nu = 1/k_\nu$. From the definition of the absorption coefficient in equation 2.35, and using the relationships between the Einstein coefficients,

$$k_\nu = n_mE_{nm}B_{mn}\phi(\nu) = \frac{n_mg_nE_{nm}c^2A_{nm}\phi(\nu)}{8\pi g_mh\nu_{nm}^3}$$

where c is the speed of light, subscript n represents the higher energy level, subscript m represents the lower energy level, and E_{nm} is the energy gap between the two levels. Assuming that the line has a Lorenzian absorption shape [49], such as in the case of a Stark broadened line, then

$$\phi(\nu) = \frac{1}{\pi} \frac{\frac{\Delta\nu}{2}}{(\nu - \nu_o)^2 + (\frac{\Delta\nu}{2})^2}$$

or

$$\phi(\eta) = \frac{1}{\pi} \frac{\frac{2}{\Delta\nu}}{1 + \eta^2} \tag{2.38}$$

where $\eta \equiv 2(\nu - \nu_o)/\Delta\nu$. Substituting the line shape from equation 2.38, the absorption coefficient is

$$k_\nu = \frac{n_m g_n E_{nm} c^2 A_{nm}}{8\pi g_m h \nu_{nm}^3} \frac{1}{\pi} \frac{\frac{\Delta\nu}{2}}{(\nu - \nu_o)^2 + (\frac{\Delta\nu}{2})^2} \frac{10^{22} m^{-3}}{n_e}$$

and the absorption coefficient at the line center $k_\nu(\nu = \nu_{nm}) = k_{\nu_o}$ is

$$k_{\nu_o} = \frac{c^2 n_m g_n A_{nm}}{4\pi^2 g_m \nu^2 \Delta\nu} = \frac{c^3 n_m g_n A_{nm}}{4\pi^2 g_m \nu^4 \Delta\nu}$$

since

$$\Delta\nu = \frac{c}{\lambda^2}\Delta\lambda = \frac{\nu^2 \Delta\lambda}{c}$$

The "core" of a line may be defined as follows, relative to the mfp. If there is a characteristic length for the problem at hand, L_{ref}, then a portion of the line is effectively trapped if $\lambda_\nu / L_{ref} \ll 1$, or if

$$\frac{\lambda_\nu}{L_{ref}} = \frac{1 + \eta^2}{L_{ref} k_\nu} \ll 1$$

Therefore the core of a line is that portion of a line (the range of $|\eta|$) which is virtually trapped relative to the relevant length scale. This is determined by

$$\frac{1 + \eta^2}{L_{ref} k_{\nu_o}} = 1$$

or, defining $(\eta)_{core}$ as the value of η where this is satisfied,

$$(\eta)_{core} = \sqrt{L_{ref} k_{\nu_o} - 1} \approx \sqrt{L_{ref} k_{\nu_o}}$$

Using a "typical" Stark-broadened case, full-widths at half-height from Griem [26] are shown in table 2.1 for various lines in the argon atom and ion. The widths are linear

		Temperature (K)			
Species	Line (Ang)	5000	10000	20000	40000
AI	1067	4.75e-4	5.41e-4	6.23e-4	7.11e-4
	1048	4.60e-4	5.25e-4	6.04e-4	6.89e-4
	3554	0.199	0.247	0.303	0.347
AII	724	6.62e-3	4.93e-3	3.64e-3	3.21e-3
	4102	0.595	0.480	0.419	0.397

Table 2.1: Line widths, in Angstroms, for several argon atomic and ionic lines, From Griem (1974).

functions of n_e: the argon atom (AI) widths were calculated with $n_e = 10^{22}\ m^{-3}$ and the argon ion (AII) widths were calculated with $n_e = 10^{23}\ m^{-3}$ in Griem [26].

For the resonant line of the argon atom (a combination of the AI 1067 and 1048 lines), $E_{21} = 11.468eV = h\nu$, $\nu = 2.82 \times 10^{15} s^{-1}$), ($n = 2$ (the first lumped excited state), $m = 1$ (the ground state), $\delta\lambda \approx 0.0005$ angstrom, and $\Delta\nu \approx 10^9 s^{-1}$. The absorption coefficient at the line center (in mks units) is then: $k_{\nu_o} = 7.3 \times 10^{-17} n_1\ m^{-1}$.

Consider now three mfp's: for ionizing radiation (λ_c), for the "core" of a particular line (λ_l), and the "wings" of the line (λ_{ll}).

$$\lambda_l \approx \frac{1.3 \times 10^{16}}{n_1}$$

and in the wings, for a Lorenzian line, the mfp is:

$$\lambda_{ll} = \frac{1.3 \times 10^{16}}{n_1}\left(1 + \left(\frac{\nu - \nu_o}{\Delta\nu_o/2}\right)^2\right) = \frac{1.3 \times 10^{16}}{n_1}(1 + \eta^2) \tag{2.39}$$

The photoionization cross-section for a hydrogenic atom from a level with principal quantum number m ($m = \sqrt{E_{1c}^H / E_{kc}}$ is the effective quantum number [74], where E_{1c}^H is the ionization potential of the ground state of the hydrogen atom (13.6 eV), and E_{kc} is the ionizational potential of the level k of interest.) is [49]

$$Q_{ph}^m \approx 8 \times 10^{-22} \frac{m}{Z^2} \left(\frac{E_{mc}}{h\nu}\right)^3$$

At the threshold (where $E_{mc} = h\nu$), the mfp for direct ionization of the ground state via radiation is

$$\lambda_c \approx \frac{1.25 \times 10^{21}}{n_1}$$

Liberman and Velikovich [44] state that the mfp for photoionization in the argon atom is 10^6 times the mfp of the line center of the resonant line. Here, we see that it is roughly a factor of 10^5 larger.

Generally $n_1 \approx 10^{22}\ m^{-3}$ in MPDT flows. This would mean that $\lambda_l \approx 10^{-6}m$ and $\lambda_c \approx 0.1m$. These results indicate that line radiation is likely to be ineffective in the production of excited states (or even ionization of ground states from resonant ionic lines, which have length scales about ten times longer) because they are trapped locally. In addition, the photoionization scale length is longer than the scale lengths of interest for an ionizing front in an MPDT. Thus radiative effects will be dropped in the ignition problem analysis. However, the effects of radiation on the volumetric rate equations will still be considered in Chapter 3, in a parametric form described in the next section.

2.4.2 Radiative Escape Factor Method

This section describes a method used to simplify the inclusion of radiative effects in a CR model, namely the "escape factor" method. The escape factors for radiative decay processes $k \to j$, β_{kj}, are indications of the optical thickness of the plasma to the individual radiative lines, and each escape factor is the net emission for the line divided by the spontaneous emission. Therefore, the product of the escape factor and the spontaneous emission $(A_{kj}n_k)$ is the net emission. This allows radiation to be included in kinetic models in a parametric manner.

The net emission in all directions, per unit time, per unit volume, for the entire kj line is the spontaneous emission minus the absorption plus the stimulated emission:

$$A_{kj}n_k - \int_{\nu_o-\infty}^{\nu_o+\infty}\int_0^{4\pi} B_{jk}\phi_{jk}(\nu)I_\nu n_j d\Omega d\nu + \int_{\nu_o-\infty}^{\nu_o+\infty}\int_0^{4\pi} B_{kj}n_k\phi_{jk}(\nu)I_\nu d\Omega d\nu$$

Combining the two integral terms,

$$= A_{kj}n_k - \int_{\nu_o-\infty}^{\nu_o+\infty}\int_0^{4\pi} B_{jk}\phi_{kj}(\nu)I_\nu\left(n_j - n_k\frac{g_j}{g_k}\right)d\Omega d\nu$$

The escape factor is simply this divided by spontaneous emission, $A_{kj}n_k$. Thus, the escape factor for the kj line is [49]

$$\beta_{kj} = 1 - \left(\frac{n_j}{n_k} - \frac{g_j}{g_k}\right)\frac{B_{jk}}{A_{kj}}\int_\nu \phi_{kj}(\nu)\int_0^{4\pi} I_{kj}d\Omega d\nu \tag{2.40}$$

The case where $\beta_{kj} = 0$ corresponds to a plasma optically thick to the line, so that no radiation escapes the vicinity of its origin, and every decay event caused by spontaneous emission is balanced by its inverse process when the radiation is absorbed. Thick lines, then, have no net effect on the kinetic balance.

The case where $\beta_{kj} = 1$ corresponds to a plasma optically thin to the line, so that all radiation produced escapes from the volume of interest. Since no radiation is absorbed, there are no excitation events to counter the decay caused by emission and the emitting level registers the maximum possible net loss.

Realistically, due mostly to the fact that the populations of the excited states are low, radiative lines between the excited states are likely to escape the plasma volume, so that $\beta_{kj} \approx 1, j > 1$. However, resonant radiation lines (where the ground state is the lower level) are more likely to be captured since the ground state population is relatively high, so that $\beta_{k1} \approx 0$.

Radiation effects are twofold: they influence the excited state populations and they contribute directly via radiative recombination. We treat radiation in a simplified manner here, following the approach of [7], [24], and [49]. This allows us to parameterize the radiation effects in a convenient way. Each transition probability, A_{lk} $(l > k)$ is then multiplied by a radiative-escape factor, β_{lk} in the kinetic rate equations.

For the resonant radiative line between the first excited state and the ground, for example, the escape factor at a depth x in a slab of thickness h, can be found, following Holstein [30] [31]. The result is [49]:

$$\beta_{21} = \frac{1}{3\sqrt{\pi k_{21}}}\left(\frac{1}{\sqrt{x}} + \frac{1}{\sqrt{H - x}}\right)$$

where k_{21} is the absorption coefficient at line center. For the large absorption coefficients for the first resonant line of the argon atom found above, the space-averaged escape factors will be small, perhaps on the order of hundredths, but generally lower than that.

Note that the radiative power loss per unit volume is:

$$\sum_{k>1}(\sum_{j<k} n_k\beta_{kj}A_{kj}E_{kj})$$

Most of the radiative power is in the resonant line from the first excited state since $n_2 E_{21}$ is large. However, resonant lines are most likely trapped ($\beta_{k1} \ll 1$), so most of this power is reabsorbed before it can escape the plasma. Assuming a slab geometry, the power density from the remaining losses due to radiative decay of the excited states is well below the electromagnetic power density found in plasma accelerators (no more than a few percent). In the model, the escape factors are varied somewhat, although, in general, experimental evidence seems to indicate that $\beta_{lk} \approx 0$ for $1 = k < l$, and $\beta_{lk} \approx 1$ for $1 < k < l$; ie., most plasmas are optically thick towards the ground state, but optically thin for all other inter-level transfers.

Chapter 3

Modeling Nonequilibrium Ionization

As stated in the Introduction, self-field magnetoplasmadynamic thrusters (MPDT) operate under conditions which make it highly unlikely that the working plasma is in ionizational equilibrium. In particular, near the inlet, where rapid ionization, heating of the electrons, and acceleration take place, the plasma may be far from equilibrium. In order to study the inlet ignition problem properly, it is therefore necessary to look first at the details of nonequilibrium ionization, to both justify and develop a convenient and accurate overall volumetric production rate model. This rate model has the advantage of including the effects of the excited states on the overall net ionization rate without having to actually solve continuity equations for the individual states. This is a big advantage, since there are 19 or more excited levels, depending on the species modeled, and the additional continuity equations may be stiff. All of the results of this analysis are characterized by the local electron temperature, T_e, and/or electron number density, n_e, both of which must be determined self-consistently by a complete model of the thruster channel.

In addition, this approach allows the excited state population distribution in a thruster channel to be determined. This is of significance to spectroscopic diagnostics, where knowledge of the population distribution is needed to properly interpret either absolute or relative line radiation intensity measurements. This may be done by using the overall rate model developed in this chapter in a realistic flow simulation, and then generating the population distribution through post-processing. However, this issue is of secondary interest to this thesis, and will be considered briefly in Appendix D, both for a stationary case (glow discharge) and for some of the ignition cases.

This chapter will focus on a reformulation of the standard collisional-radiative (CR) rate model for atoms and ions, and the calculation of overall collisional rate coefficients for ionization and recombination. In the standard CR model, the structure of both atoms and ions is modeled as a ground state, a group of lumped electronically excited states, and the next higher ion, or continuum. Rate equations are then written for each of the modeled excited levels which include the effects of excitation, ionization, and radiative decay, and the inverse processes.

A schematic of the energy-structure of a typical atom or ion is shown in figure 3.1. (This figure is based on the hydrogen atom, for which excited state k has energy $E_k = E_{1c}(1 - 1/k^2)$, where E_{1c} is the ground state to continuum energy gap - the ionization potential energy.) The ground state (which will be denoted by index $k = 1$ in this analysis) is at zero energy. As is typical for most atoms and ions, the energy gap between the ground and the first excited state ($k = 2$) and the continuum ($k = \infty$) is several times the energy gap between the first excited state and the continuum ($k = \infty$). The simplest model of such an atom or ion is a two-level one: the ground state and the continuum. A three-level model would add either the actual first excited state, or a lumped excited level containing several close-lying (by energy) states. A multi-level model will be defined here as an atom or ion model which includes the ground state, several excited levels (actual states or lumped levels) and the continuum.

The ionizational equilibrium referred to here is "Saha-Boltzmann equilibrium", which is a statement of the law of mass action. That is, the plasma is in a state of equilibrium due entirely to collisional transitions amongst the excited levels as well as between the levels and the continuum. In a situation where equilibrium exists, each level's population is then calculated by the Saha-Boltzmann equilibrium formula applied to that level.

There are several distinctions to be made about what equilibrium is in a multi-level model [55] [72]. *Thermal equilibrium* would require that the levels are all populated as per the Saha-Boltzmann equation, the radiation fields are black-body, and the plasma is uniform in the volume of interest. A more likely case is *local thermodynamic equilibrium* (LTE), in which case each of the levels is at its Saha-Boltzmann (S-B, equilibrium) population, and the radiation field is unconstrained. *Complete LTE* (CLTE) occurs when all the levels are in

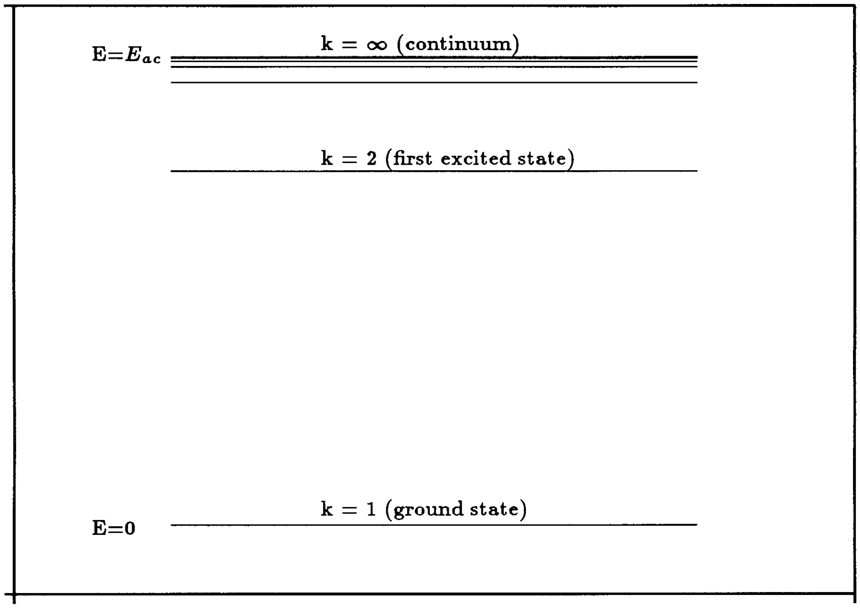

Figure 3.1: Electronically excitation energy structure of a multi-level atom or ion model

the S-B distribution, and *partial LTE* (PLTE) when the uppermost levels have equilibrated with one another by electron-atom (or ion) collisions, although they do not necessarily obey the S-B populations at the local electron temperature. It will be shown here that PLTE occurs most often under the conditions of interest in plasma thrusters.

Table 3.1, following Drawin's categorization (Chapter 3 in [72]) illustrates some of the variety of plasma conditions. Plasma accelerators are most likely to operate in the nonstationary, dynamical and partial LTE (or PLTE) regime.

Since the collisions in this model are all due to interactions between light, fast electrons and heavy, slow atoms or ions, a significant ratio relative to a transition between levels j and k is the ratio of the electron average kinetic energy to the energy gap between the levels, $\frac{3}{2}k_BT_e/E_{jk}$. The addition of the intermediary levels means that it is likely that a ground state atom will jump the gap E_{12} to the first excited level before ionizing. Gaps of E_{2c} and smaller are then of particular significance for ionization and recombination. Therefore, $\frac{3}{2}k_BT_e/E_{2c}$ is a reasonable ratio to scale temperatures for this problem. An energy of $\frac{2}{3}E_{2c}$ corresponds to a temperature of $31000K$ for argon and $26300K$ for hydrogen. Temperature on this order are commonly found both experimentally and computationally in MPDTs.

All approaches to the ionizational rate problem rely at some level on experimental

Condition:	Plasma Classification:
all $n_k \neq n_k^*$	complete non-LTE
only a few $n_k \neq n_k^*$	partial non-LTE
$\frac{\partial n_k}{\partial t} = 0$	steady-state
$\frac{\partial n_k}{\partial t} \neq 0$	transient
$\frac{\partial n_k}{\partial t} = 0$ and $\nabla \cdot (n\vec{v})_k = 0$	steady-state and homogeneous (uniform)
$\frac{\partial n_k}{\partial t} \neq 0$ and $\nabla \cdot (n < \vec{v} >)_k \neq 0$	transient dynamical
$\frac{\partial n_k}{\partial t} = 0$ and $\left(\frac{\partial n_{kt}}{\partial t}\right)_{coll,rad} \ll \nabla \cdot (n < \vec{v} >_k)$	steady-state diffusion-dominated

Table 3.1: Plasma Conditions

results, either to determine collisional cross sections or to fit rates directly. Most then express the net ionization rate as due to the difference between two-body (e-a) ionizing and three-body (electron-electron-ion) recombining collisions, neglecting radiation, and written in a form similar to:

$$\dot{n}_e = n_e n_a S_{ac} - n_e^2 n_i S_{ca} \tag{3.1}$$

where S_{ac} and S_{ca} are the overall ionization and recombination collisional rate coefficients, respectively, and n is a number density with units particles/unit volume. (The subscripts i and a refer to the continuum (the next higher ion) and the atom, respectively, and e refers to the electron.) When all species are in equilibrium (denoted here by superscript *); i.e., the ionization and recombination rates are balanced (overall microreversibility). Then,

$$S_{ac} = \left(\frac{n_e n_i}{n_a}\right)^* S_{ca}$$

and the net ionization rate (equation 3.1) can then be expressed as:

$$\dot{n}_e = n_e n_e^* n_i^* S_{ca} \left[\frac{n_a}{n_a^*} - \frac{n_e n_i}{n_e^* n_i^*}\right] \tag{3.2}$$

In this thesis, it will be assumed that the electron density is a given, or calculated quantity, and that $n_e = n_e^*$, $n_i = n_i^*$. Thus, equation 3.2 will become

$$\dot{n}_e = n_e^3 S_{ca} \left[\frac{n_a}{n_a^*} - 1 \right] \tag{3.3}$$

which is the general form that will be used later in this chapter to rewrite the standard rate equations.

In the full standard rate model adapted here, both collisional and radiative (in a parametric manner) volumetric losses and gains for the ground state, the excited states and the ion are accounted for. The radiative effects will be twofold: they may influence the excited state population distribution and they may contribute directly via radiative recombination. As will be seen, radiative effects are strongest at electron number densities and electron temperatures that are low compared to typical MPDT values.

3.1 Equilibrium Ionization Basics

Before discussing nonequilibrium ionization, the equilibrium case should be described. This is, again, equilibrium between the rates of ionization and recombination. The net ionization rate equation, as in equation 3.1, can be written most generally as the difference between a gain term (ionization) and a loss term (recombination):

$$\dot{n}_e = \dot{n}_e^{gain} - \dot{n}_e^{loss} \tag{3.4}$$

There are two important limits to this rate equation. When the rate coefficients and/or densities are small (where "small" is determined relative to the time scale of the problem at hand), then

$$\dot{n}_e \approx \dot{n}_e^{gain} \approx \dot{n}_e^{loss} \approx 0$$

the plasma is considered to be frozen, and reactions do not contribute to the determination of the densities of the excited states.

The other limit occurs when the rate coefficients and/or densities are high (again, the definition of 'high" depends on the other time scales involved), so that the reactions are rapid enough to drive the plasma virtually to equilibrium:

$$\dot{n}_e \ll \dot{n}_e^{gain}, \dot{n}_e^{loss}$$

If the ionization time scale is much smaller than that of any other process in the problem at hand (i.e., diffusion, convection), then $(\dot{n}_e^{gain} - \dot{n}_e^{loss}) \rightarrow 0$ very quickly compared to the rest

frozen	$\dot{n}_e^{gain} \rightarrow 0$	$\dot{n}_e^{loss}/\dot{n}_e^{gain}$ remains finite	$\dot{n}_e = N/\tau$; $\tau \rightarrow \infty$
equilibrium	$\dot{n}_e^{gain}/\dot{n}_e \rightarrow \infty$	$\dot{n}_e^{loss}/\dot{n}_e^{gain} \approx 1$	$\dot{n}_e = N/\tau$; $N \rightarrow 0$

Table 3.2: Summary of frozen and equilibrium cases. Here "0" and "∞" are relative to the other terms in the ion/electron continuity equation.

of the processes acting in the plasma, and this is an equilibrium plasma, where the excited state populations are *solely* dependent on the reactive balance.

To summarize the difference between frozen and equilibrium cases, equation 3.4 can be rewritten as

$$\dot{n}_e = \dot{n}_e^{gain}\left(1 - \frac{\dot{n}_e^{loss}}{\dot{n}_e^{gain}}\right) \tag{3.5}$$

and then table 3.2 summarizes the frozen and equilibrium cases.

Schematically, in the equilibrium case, the balance is

$$\text{atoms} + \text{ionization energy} = \text{ions} + \text{electrons}$$

The law of mass action for this case is, from Pai [54]:

$$\frac{p_i p_e}{p_a} = C T_e^{5/2} \exp\left(-\frac{E_{ac}}{k_B T_e}\right)$$

where p_i, p_e, and p_a are the partial pressures for the ion, electron, and atom species, respectively, and E_{ac} is the ionization energy for the atom. The factor C is determined from statistical mechanics, and involves the partition functions of the three species involved. In the case of ionization, the balance is referred to the Saha-Boltzmann equation [49]. For a level k of plasma species s, the Saha-Boltzmann (S-B) equation is:

$$S(s,k,T_e) \equiv \left(\frac{2\pi m_e k_B T_e}{h_P^2}\right)^{3/2} \frac{2g_i^s}{g_k^s} \exp\left(-\frac{E_{kc}^s}{k_B T_e}\right) = \left(\frac{n_e n_i^s}{n_k^s}\right)^* \tag{3.6}$$

where g_i^s is the degeneracy of the ion ground level, g_k^s is the degeneracy of the level k, E_{kc} is the energy difference between the continuum and the level k, and h_P is Planck's constant. The number densities are: for the level k, n_k^s; for the electrons, n_e, and for the continuum (next higher ion), n_i^s.

Assuming that $\sum n_k^s \approx n_1^s$, then the law of mass action applied to the balance between overall gain and loss yields the following equation for the ground state (level $k = 1$) of species s

$$S(s,1,T_e) = \left(\frac{n_e n_i^s}{n_1^s}\right)^* = \frac{S_{ac}^s}{S_{ca}^s} \tag{3.7}$$

Consider now a single gas species, so that the species superscript can be dropped. Defining the ionization fraction as the ratio of free electron density (n_e) to gas nuclei density (n_g),

$$\alpha \equiv n_e/n_g$$

then, from equation 3.7,

$$S(s,1,T_e) = \frac{\alpha_{eq}^2 n_g}{1-\alpha_{eq}}$$

Solving for the equilibrium ionization fraction, α_{eq},

$$\alpha_{eq} = \frac{1}{2\Lambda_2}\left(\sqrt{1+4\Lambda_2}-1\right) \tag{3.8}$$

which is a function of one parameter,

$$\Lambda_2 \equiv \frac{n_g}{S(s,1,T_e)}$$

The values of α_{eq} at high and low values of Λ_2 are

$$\alpha_{eq} \to \frac{1}{\sqrt{\Lambda_2}} \text{ as } \Lambda_2 \to \infty$$

$$\alpha_{eq} \to 1 - \Lambda_2 \text{ as } \Lambda_2 \to 0$$

Figure 3.2 is a plot of the equilibrium ionization fraction versus the parameter Λ_2. Figure 3.3 is a plot of the equilibrium ionization fraction versus the electron temperature for various number densities. Note that, although the ionization fraction drops with increasing overall density n_g at a particular temperature, $n_e/S(s,1,T_e)$ is a monotonically rising function of n_g.

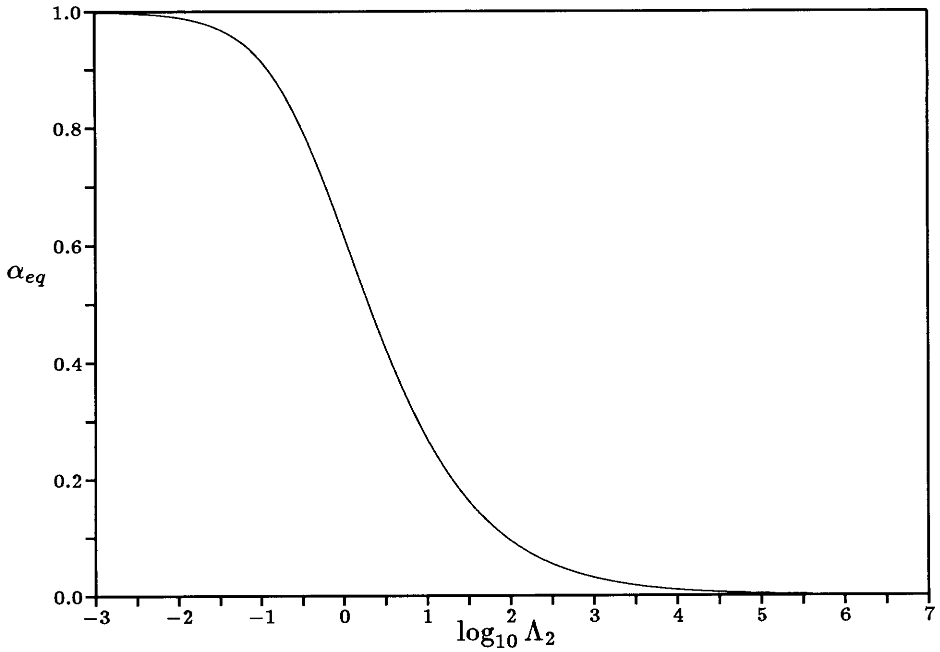

Figure 3.2: Equilibrium ionization fraction as a function of the parameter Λ_2.

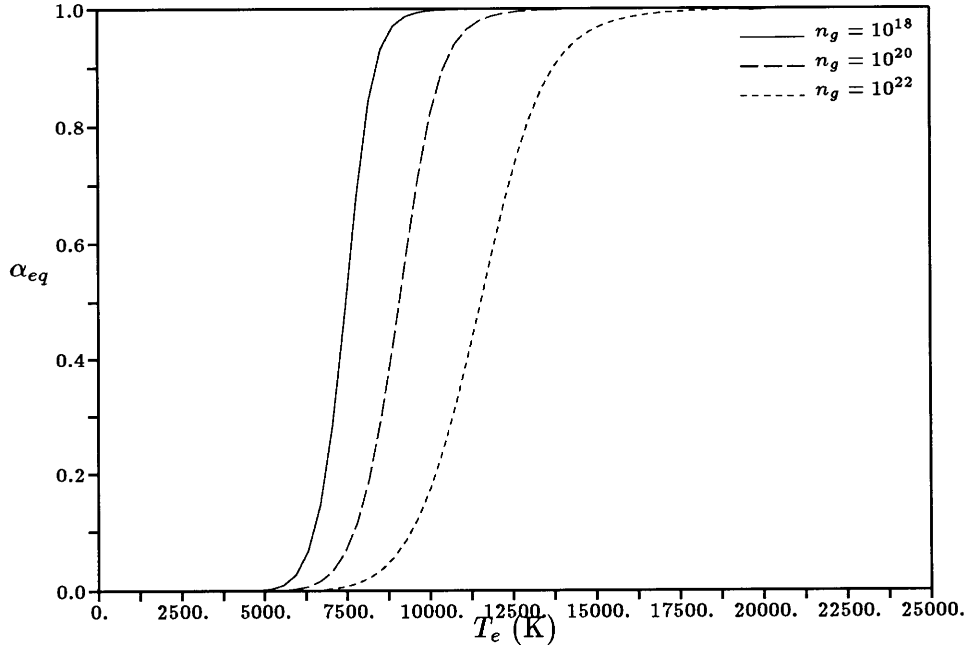

Figure 3.3: Equilibrium ionization fraction in argon as a function of electron temperature for various heavy particle densities (the units of n_g are m^{-3}).

3.1.1 Ionizational Equilibrium with Second Ions

For the case where second ions, of argon, for example, are present, the S-B (law of mass action) equations for the argon I and II species must be combined to determine the individual densities. Define

$$S(a,1,T_e) = \frac{n_e n_1^+}{n_1^a} = S^o \tag{3.9}$$

$$S(i,1,T_e) = \frac{n_e n_1^{++}}{n_1^+} = S^+ \tag{3.10}$$

where all of these densities are equilibrium densities. Then, using $n_e = n^+ + 2n^{++}$, the equilibrium densities are (using now the superscript $*$ to indicate an equilibrium quantity):

$$(n^+)^* = \frac{n_e^2}{n_e + 2S^+} \tag{3.11}$$

$$(n^{++})^* = \frac{n_e S^+}{n_e + 2S^+} \tag{3.12}$$

$$(n_1^a)^* = \frac{n_e (n^+)^*}{S^0} = \frac{n_e^3}{S^0(n_e + 2S^+)} \tag{3.13}$$

Then, if the total number of nuclei in the gas is $n_g = (n^+)^* + 2(n^{++})^* + n_a^*$, or

$$n_g = \frac{n_e^2}{n_e + 2S^+} + \frac{n_e S^+}{n_e + 2S^+} + \frac{n_e^3}{S^0(n_e + 2S^+)}$$

yielding the following equation for the ionization fraction, $\alpha = n_e/n_g$ (which can now be greater than one),

$$\alpha^3 \Lambda_2 + \alpha^2 + \alpha\left(\frac{1}{2\Lambda_2^+} - 1\right) - \frac{1}{\Lambda_2^+} = 0 \tag{3.14}$$

where Λ_2 is as before, and

$$\Lambda_2^+ = \frac{n_g}{S^+} = \left(\frac{g_i}{g_1}\right)^{atom} \left(\frac{g_1}{g_i}\right)^{ion} \exp\left(\frac{E_{1c} - E_{1c}^+}{k_B T_e}\right) \Lambda_2$$

Note that in the limits, as $\Lambda_2 \to \infty$, the single ion result of the previous section is approached, and as $\Lambda_2 \to 0$, $\alpha^* \to 2$.

To reflect the fact that some of the ions are first ions and some are second ions, and using $n_e = n^+ + 2n^{++}$, the ratio

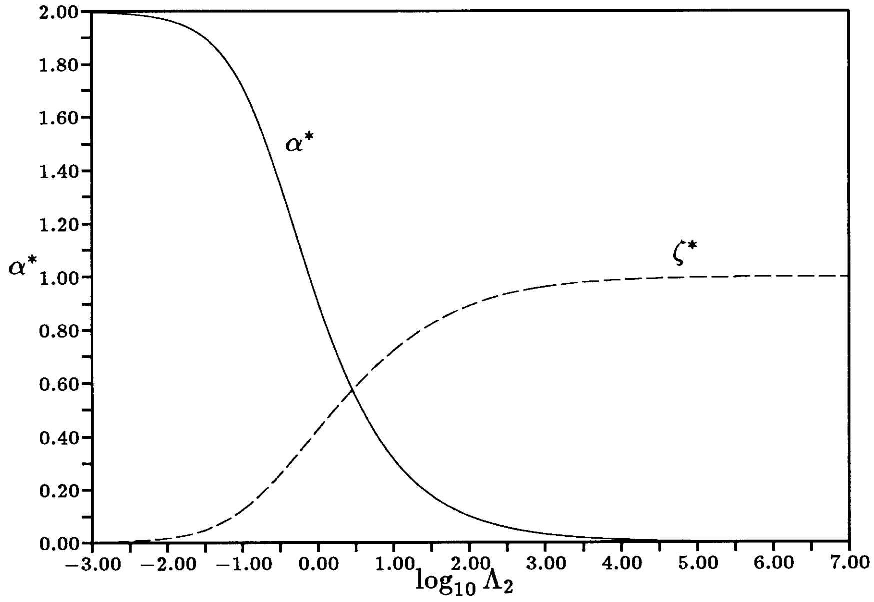

Figure 3.4: Equilibrium ionization fraction and ζ^* as a function of the parameter Λ_2 with both first and second ions present.

$$\zeta \equiv \frac{n^+}{n_e}$$

is defined. ($\zeta \approx 1$ for plasmas that are weakly ionized, and only the first ion is present regardless of the ionization fraction). ζ drops to zero when the plasma contains only second ions and electrons. For most cases relevant to plasma accelerators, $\zeta \approx 1$ except for certain hot, low density regions.) Note that the equilibrium ion ratio is

$$\zeta^* = \left(\frac{n_e}{n_e + 2S^+}\right)^* = \frac{\alpha_{eq}}{\alpha_{eq} + 1/\Lambda_2^+}$$

Figure 3.4 is a plot of both α^* and ζ^* for argon. In this plot, for simplicity, $\Lambda_2^+/\Lambda_2 = 6\exp(-2)$ The ionization fraction approaches 2 when all of the ions are second ions.

3.1.2 Ionizational Equilibrium with Two Gas Species

Besides the cases of singly and doubly ionized plasmas of one species, there are cases where there are two different singly ionized species present in the same plasma. One such situation occurs when a higher ionization fraction is desired in a plasma of a particular species under fixed conditions, in which case it is common to "seed" the plasma with a gas of lower ionization potential in order to produce more free electrons. Another situation where a second species may be introduced into a plasma is when a second gas, again of lower ionization potential than the original species (which implies more highly populated excited states) is used to produce more intense spontaneous decay line radiation when spectroscopic diagnostics are used in an experiment [36].

Consider then a case where two atomic species, s_1 and s_2 are present in a mixture, at the same temperature. The relevant temperature here is T_e, which is common. For atomic gases, differing T_g will not have an effect on the partition functions. Assuming that the $n_s = \sum n_k^s \approx n_1^s$; that is, that most of the each atomic species is in the ground state, then the equilibrium ionization fraction for each species is found from

$$\left(\frac{\alpha^2}{1-\alpha}\right)_s = \frac{S(s,1,T_e)}{n_g^s} = \frac{1}{\Lambda_2^s}$$

Writing this expression for both species, and dividing one by the other, the result is

$$\left(\frac{\alpha^2}{1-\alpha}\right)^*_{s_1} \left(\frac{1-\alpha}{\alpha^2}\right)^*_{s_2} = \left(\frac{g_i}{g_1}\right)_{s_1} \left(\frac{g_1}{g_i}\right)_{s_2} \frac{n_g^{s_2}}{n_g^{s_1}} \exp\left(\frac{E_{1c}^{s_2} - E_{1c}^{s_1}}{k_B T_e}\right)$$

where E_{1c}^s is the energy gap between the ground state (1) and the continuum (c) for each species. The S-B equilibrium ionization fractions are equal at the following "crossover temperature", T_x:

$$T_x = \frac{E_{1c}^{s_2} - E_{1c}^{s_1}}{k_B \ln\left[\left(\frac{g_1}{g_i}\right)_{s_1} \left(\frac{g_i}{g_1}\right)_{s_2} \frac{n_g^{s_1}}{n_g^{s_2}}\right]}$$

The crossover temperature, for a two gas species, $T_x(s_1, s_2)$, is the temperature beyond which the equilibrium ionization fraction of species 1 will be greater than that of species 2. For example, for several species combinations, at $n_g^{s_1} = n_g^{s_2}$: $T_x(A, H) \approx 10,100K$, $T_x(A, Cs) \approx 55,400K$, and $T_x(H, Cs) = \infty$ (since H and Cs have the same ground state and first ion degeneracies). Figure 3.5 illustrates the crossover temperature for the hydrogen/argon pairing. Shown are the equilibrium ionization fractions for each species at 5 different total number densities. Below $T_x(A, H) \approx 10,100K$, at the same densities, the hydrogen ionization fraction is higher than that of argon, and above T_x, the argon ionization fraction is the larger of the two.

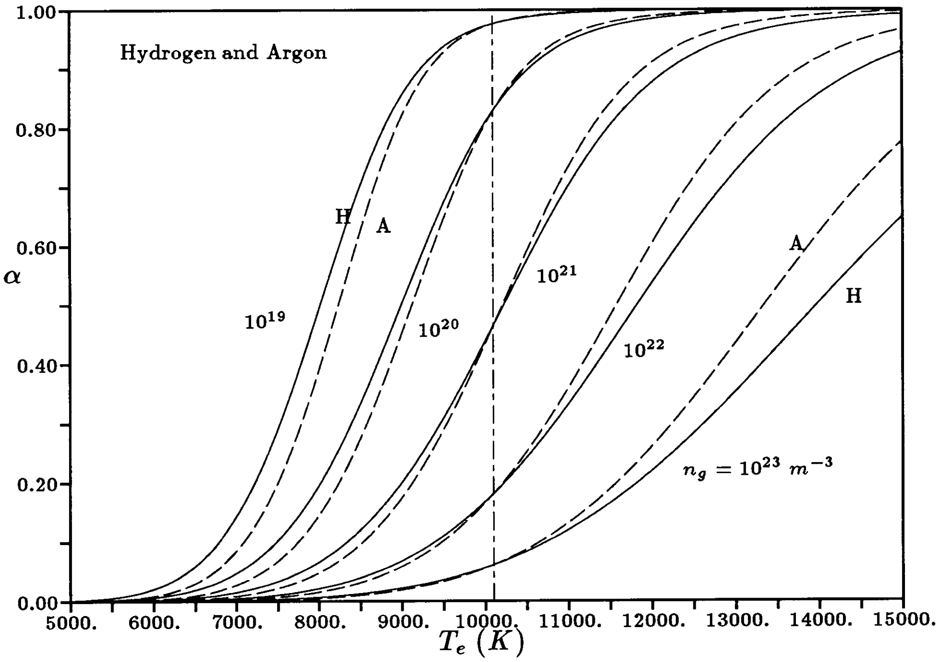

Figure 3.5: Equilibrium ionization fraction vs T_e for hydrogen (H) and argon (A) at various total number densities. The solid line represents hydrogen and the dashed line is argon. A vertical line is drawn at the crossover temperature, $T_x \approx 10100\ K$.

3.2 The Standard Collisional-Radiative (CR) Model

Here, the collisional-radiative model is presented. This is a standard approach, using volumetric production rate equations as in Bates [7], Gomes [24], and Mitchner and Kruger [49] as a basis. We then work with the steady-state continuity equations for each species s (either an electronically excited level or the continuum):

$$\nabla \cdot (n_s \vec{u}_s) = \dot{n}_s$$

The $\dot{n}_s$ terms are the volumetric production rates for each level and the continuum. The assumptions behind the model, the processes included in it, and the formulation of the problem are discussed below.

The model for the atom or ion in question consists of its ground state, its electronically excited states, and the continuum - the next ionic species. As described in appendix B, the actual excited states are not used; instead lumped levels are used, with the assumption that states with very close energies are likely to be quickly equilibrated amongst themselves.

3.2.1 Standard CR Assumptions

The following standard set of assumptions have been made in order to make the collisional-radiative modeling problem more tractable. Results from calculations by earlier researchers bear out that they are not overly constrictive [7] [49], and they do not conflict with the conditions found in MPDTs.

1. The electrons are assumed to be sufficiently equilibrated amongst themselves through collisions so that a Maxwellian distribution can be used for them. This, coupled with assumption 3, allows the rate coefficients for collisional processes to be easily calculated.

2. A two-temperature plasma is assumed. The electrons are assumed to have a Maxwellian distribution with a temperature T_e, and all of the heavy particles (atoms and ions) are at T_g.

3. It is also assumed that all of the inelastic collisions which have an effect on the number densities are driven by the electrons. This is generally a fair assumption in an MPD thruster - see figure 2 from [22] for a typical case.

4. The plasma is quasineutral, so that conservation of charge applies.

3.2.2 Standard CR Processes Included

Ten collisional or radiative processes which populate or depopulate a given excited state of an atom or ion are included in the standard CR model [7] [49]. The following is a description of the actual events behind the processes. Assume that we are focusing on an energy level k of atom or ion A: A_k. Then, for $j < k < l$, we have:

1. Collisions which excite atoms in lower electronic levels to the level k - a gain: $e + A_j \rightarrow e + A_k$
2. Collisions which deexcite atoms in level k down to lower electronic levels - a loss: $e + A_k \rightarrow e + A_j$
3. Collisions which excite atoms in electronic level k up to higher levels - a loss: $e + A_k \rightarrow e + A_l$
4. Collisions which deexcite atoms in higher electronic levels down to level k - a gain: $e + A_l \rightarrow e + A_k$
5. Singly ionizing collisions which deplete level k atoms - a loss: $e + A_k \rightarrow e + e + A^+$
6. Three body recombination collisions which produce level k atoms - a gain: $e + e + A^+ \rightarrow e + A_k$
7. Net radiative decay from level k atom to lower levels - a loss: $A_k \rightarrow A_j + h\nu_{jk}$ ($\nu_{jk} = \frac{E_k - E_j}{h}$)
8. Net radiative decay from higher levels down to level k - a gain: $A_l \rightarrow A_k + h\nu_{kl}$ ($\nu_{kl} = \frac{E_l - E_k}{h}$) Processes 7. and 8. are combined by means of the "escape factor", $0 \leq \beta_{kj} \leq 1$.
9. Radiative recombination events resulting in level k atoms - a gain: $e + A^+ \rightarrow A_k + h\nu_{kc}$ (where $\nu_{kc} = \frac{E_c - E_k}{h}$, where c is the continuum index and h is Planck's constant)
10. Photoionization (inverse of 9.) from level k. Processes 9. and 10. are combined by means of the "escape factor", $0 \leq \beta_{ck} \leq 1$.

3.2.3 Definition of The Degree of Nonequilibrium

The standard collisional-radiative rate equations [7] [49] (also see Appendix C) can be rewritten through use of the microreversibility relationships between the collisional rate coefficients. The resulting equations deal directly with the effects of nonequilibrium of the electronic states. Writing the ratio of a level's deviation from equilibrium to its equilibrium population as

$$\delta_k \equiv \frac{n_k}{n_k^*} - 1 \tag{3.15}$$

yields a useful variable, δ_k, to be referred to in this work as *the degree of nonequilibrium of a level k*. When the level k is at its S-B population, then $\delta_k = 0$. When the level k is underpopulated relative to its S-B value, then δ_k will be negative (the limit is an empty level, in which case, $\delta_k = -1$), and overpopulated levels have $\delta_k > 0$. Van der Mullen, et al. [70] refer to δ_k as the relative overpopulation of level k.

In the next sections, the standard CR equations are rewritten using the degree of nonequilibrium variable instead of the actual number densities, which was the original form. In these equations, it will be assumed that n_e is known.

3.2.4 Collisional Excitation and De-excitation to and from a Level

The net rate of change of number density of an excited level, k, to and from some other level, j, via excitation and/or de-excitation collisions is equal to the loss by deexcitation collisions down to the lower level plus the gain by excitation collisions from the lower level [49] [7] :

$$(\dot{n}_k^s)_j = -n_e n_k^s S_{kj}^s + n_e n_j^s S_{jk}^s$$

where n_j and n_k are the number densities of levels j and k, respectively, only electron-heavy collisions have been included, and S_{kj} is an excitation or deexcitation rate coefficient for the $j \rightarrow k$ transition. (See Appendix C for details of the choices for both collisional cross-sections and rate coefficients.)

$$(\dot{n}_k^s)_j = -n_e S_{kj}^s \left(n_k^s - n_j^s \frac{S_{jk}^s}{S_{kj}^s} \right)$$

Microreversibility (detailed balance) requires that the two rates be balanced when they are in their Saha-Boltzmann distribution. Taking advantage of this,

$$(\dot{n}_k^s)_j = -n_e S_{kj}^s \left(n_k^s - n_j^s (\frac{n_k^s}{n_j^s})^* \right)$$

where the superscript $*$ denotes an equilibrium value. Regrouping,

$$(\dot{n}_k^s)_j = -n_e S_{kj}^s (n_k^s)^* \left(\frac{n_k^s}{(n_k^s)^*} - \frac{n_j^s}{(n_j^s)^*} \right)$$

Finally, using equation 3.15,

$$(\dot{n}_k^s)_j = n_e^2 n_i^s \frac{S_{kj}^s}{S(s, k, T_e)} (\delta_j - \delta_k) \tag{3.16}$$

where $S(s, k, T_e)$ is the S-B equation for level k of species s, as defined by equation 3.6.

3.2.5 Collisional Ionization from and Recombination into a Level

The net rate of change of number density of an excited level, k, to and from the continuum is equal to the difference between ionization and recombination:

$$((\dot{n}_k)^s)_c = -n_e n_k^s S_{kc}^s + n_e^2 n_i^s S_{ck}^s$$

where S_{kc} is the ionization rate coefficient and S_{ck} is the three-body recombination rate coefficient. Regrouping,

$$((\dot{n}_k)^s)_c = -n_e S_{ck}^s \left(n_k^s \frac{S_{kc}^s}{S_{ck}^s} - n_e n_i^s \right)$$

and taking advantage of microreversibility, assuming that $n_e^*(n_i^s)^* = n_e n_i^s$:

$$((\dot{n}_k)^s)_c = -n_e S_{ck}^s \left(n_k^s (\frac{n_e n_i^s}{n_k^s})^* - n_e n_i^s \right)$$

or

$$((\dot{n}_k)^s)_c = -n_e^2 n_i^s S_{ck}^s \left(\frac{n_k^s}{(n_k^s)^*} - 1 \right)$$

and, using the degree of nonequilibrium variable, δ_k^s, this becomes

$$((\dot{n}_k)^s)_c = -n_e^2 n_i^s S_{ck}^s \delta_k^s \tag{3.17}$$

3.2.6 Radiative Losses from and Gains to a Level

The net rate of change of number density for a level k due to radiation is the sum of losses to lower levels, gains from higher levels, and net gain due to photorecombination.

$$(\dot{n}_k^s)_r = -\sum_{j<k} n_k \beta_{kj} A_{kj} + \sum_{l>k} n_l \beta_{lk} A_{lk} + n_e n_i^s \beta_{ck} A_{ck}$$

where A_{kj} are the Einstein probabilities for radiative transitions (the inverse of the mean radiative lifetime), and β_{kj} are the radiative escape factors defined in chapter 2. The escape factors allow for radiation to be considered parametrically: when $\beta_{kj} = 0$, no radiation escapes, the spontaneous emission associated with a decay from level k to j is balanced by absorption and excitation back up from j to k, and there is no net effect on the rate; when $\beta_{kj} = 1$, then the effect is a net rate of loss of level k number density and a net rate of gain of level j number density. The $n_e n_i^s \beta_{ck} A_{ck}$ term represents the net rate of production of level k number density due to the sum of photorecombination minus photoionization. Note that under conditions of strong irradiation and/or low local emission, the radiative escape factors may be greater than unity.

The microreversibility relations do not appear naturally here. However, they are still used in order to obtain the δ_k form:

$$(\dot{n}_k^s)_r = -\frac{n_e n_i^s}{S(s,k,T_e)} \sum_{j<k} \frac{n_k}{(n_k)^*} \beta_{kj} A_{kj} + \sum_{l>k} \frac{n_e n_i^s}{S(s,l,T_e)} \frac{n_l}{(n_l)^*} \beta_{lk} A_{lk} + n_e n_i^s \beta_{ck} A_{ck}$$

and finally:

$$\begin{aligned}(\dot{n}_k^s)_r = & -\frac{n_e n_i^s}{S(s,k,T_e)} \left[\sum_{j<k} \delta_k \beta_{kj} A_{kj} + \sum_{j<k} \beta_{kj} A_{kj} \right] \\ & + n_e n_i^s \left[\sum_{l>k} \frac{(\delta_l + 1) \beta_{lk} A_{lk}}{S(s,l,T_e)} \right] + n_e n_i^s \beta_{ck} A_{ck}\end{aligned} \tag{3.18}$$

3.2.7 The CR Equations in the δ_k Form

Using the terms derived above, the full rate equations may be written. The species superscript has been dropped for convenience.

For the continuum the net ionization is the sum of the ionization terms from the individual levels (see equation 3.17) minus the net radiative recombination term:

$$\dot{n}_e = n_e^2 n_i \sum \delta_k S_{ck} - n_e^2 \sum A_{ck}\beta_{ck} \tag{3.19}$$

and for the individual levels, grouping the terms derived above and given by equations 3.16, 3.17, and 3.19, results in:

$$\begin{aligned}
\dot{n}_k &= n_e^2 n_i[\sum_{j\neq k} \frac{(\delta_j - \delta_k)S_{kj}}{S(s,k,T_e)} - \delta_k S_{ck}] \\
&+ n_e n_i[\sum_{l>k} \frac{\delta_l A_{lk}\beta_{lk}}{S(s,l,T_e)} - \sum_{j<k} \frac{\delta_k A_{kj}\beta_{kj}}{S(s,k,T_e)}] \\
&+ n_e n_i[A_{ck}\beta_{ck} + \sum_{l>k} \frac{A_{lk}\beta_{lk}}{S(s,l,T_e)} - \sum_{j<k} \frac{A_{kj}\beta_{kj}}{S(s,k,T_e)}]
\end{aligned} \tag{3.20}$$

For those cases where there are multiple ions in the plasma, then conservation of charge requires:

$$\sum Z_i^s n_i^s = n_e$$

where Z^s is the charge of the ion of species s divided by e.

The final line of equation 3.20 shows that, even when the levels are all in their S-B equilibrium distribution (i.e., all δ_k are zero), there may still be a rate of change for all levels due to radiation. However, S-B equilibrium usually implies high electron number density, and then radiative effects on the rates are comparatively insignificant in affecting the excited state distribution (although this may not mean low radiation power loss).

3.3 Formulation of the CR Equations with Dynamic Equilibrium of the Excited States

So far, the standard CR equations have simply been rewritten in a convenient new form. Now, with the help of an assumption that will be tested first, the CR equations may be recast in a form which will make it possible to determine both the population distribution of the excited levels and overall ionization and recombination coefficients. This key assumption is that the excited states are in a dynamic balance because their characteristic time scales are much smaller than the convective and diffusive scales found in MPDTs (the quasi-steady-state-solution case). This is critical, since if the excited states varied on time - and length - scales similar to the convective and diffusive scales in the thruster, then the only way to include the effects of the excited states would be to include continuity equations for each of the states in a numerical simulation of the flow.

The upper levels relaxation time is on the order of the collisional time $t_{kj} = \frac{\lambda_{kj}}{\bar{c}_e}$, while the ground state relaxation time must be coupled to the diffusion time, which depends on whether diffusion is perpendicular (ambipolar boundary layer) or parallel (which is only likely near the inlet region of a channel) to convection:

$$(t_d)_\perp = \frac{h^2}{\bar{c}_{in}\lambda_{in}}$$

$$(t_d)_{||} = \frac{\bar{c}_{in}\lambda_{in}}{u_{ref}^2}$$

where λ_{kj} is the excitation mean free path, λ_{in} is the ion-neutral mean free path, $\bar{c}$ is a thermal velocity, and u_{ref} is a characteristic speed, which is typically $O(10^2) - O(10^3)\frac{m}{s}$ [27] for an MPD thruster. The resulting ratios are

$$\frac{t_{kj}}{(t_d)_\perp} = \frac{\bar{c}_{in}}{\bar{c}_e}\frac{\lambda_{in}}{h}\frac{\lambda_{kj}}{h}$$

$$\frac{t_{kj}}{(t_d)_{||}} = \frac{\lambda_{kj}}{\lambda_{in}}\frac{u_{ref}}{\bar{c}_e}\frac{u_{ref}}{\bar{c}_{in}}$$

For the perpendicular case, the first two ratio factors on the right-hand side should be small enough so that the ratio is small, even if the last term is not. However, in the parallel case, the ratio is not necessarily small. Near the inlet, we will have to consider diffusion and convection of the excited levels. However, if we limit ourselves to ambipolar boundary layers, then the upper level relaxation time scale is very short compared to the ground state and diffusive time scales.

This can be quantified by applying the rate equations, and requiring that the volumetric production time scale of each of the excited states be much smaller than the mechanical time scales characteristic of an MPD thruster device (i.e., convection and diffusion. This will be done only for the argon atom) The collisional time scale for a level k is

$$t_K = \frac{n_k}{\dot{n}_k} \approx \frac{1}{n_e S_K}$$

where $S_K = \sum_{j \neq k,c} S_{kj}$. The mechanical time scale is $t_m = l_{ref}/u_{ref}$. For the bulk plasma in an MPD thruster, of length $L \approx 0.2m$ and $u_{ref} \approx 8000m/s$ from the MPDT work of Martinez [46]. Thus the bulk mechanical time scale is

$$t_{mb} = \frac{L}{u_{ref}} \approx 2.5 \times 10^{-5} s$$

At the inlet, we use the back-diffusion length scale, $l_{ref} = C_a/G$, and a characteristic speed of a few hundred m/s, $u_{ref} \approx 200m/s$, which is appropriate average based on the 1-D MPDT calculations of Niewood [50] and Martinez [46] and the reference to experimental values of the inlet speed by Chouieri [18]. For a typical MPDT $G = n_g u = 8 \times 10^{24}$ (corresponding to $\dot{m}/A = 0.5 \frac{kg}{m^2 s}$, used by Martinez [46]), and the definition of C_a, the mechanical time scale at the inlet, t_{mi}, due to back-diffusion is

$$t_{mi} = \frac{C_a}{G u_{ref}} \approx 1.7 \times 10^{-8} \sqrt{T_e} s$$

for $T_e = 2T_g$. Then, $t_k \ll t_{mb}$ and $t_k \ll t_{mi}$ imply: $n_e S_K \gg 40000 \frac{1}{s}$ and $n_e S_K \gg 1.18 \times 10^8 / \sqrt{T_e} s^{-1}$, respectively.

Figure 3.6 is a plot of t_{mb}/t_K for the first lumped excited level of the argon atom, using bulk plasma conditions. This level is chosen for the comparison since the level to level energy gaps decrease as the continuum is approached, so the first excited level will have the largest t_K. The assumption that $t_{mb}/t_K \gg 1$ is shown to be quite reasonable in an argon plasma at MPDT conditions.

Figure 3.7 is a plot of t_{mi}/t_K, again for the first lumped excited state of the argon atom. For typical inlet densities ($n_g \approx 10^{22} m^{-3}$), the dynamic equilibrium assumption for the excited states would be valid at $\alpha > 0.001$ or more, which is very reasonable for the cases encountered in this work.

Another way to look at the time scale issue is to simply look at a stationary plasma, perturbed from equilibrium, relax back to equilibrium over time. If the excited states (and to be conservative, only the 7 lowest excited levels will be used here) relax much faster than does the ground state, then the excited level may be considered to be volumetrically balanced on the time scale of the ground state. The set of resulting equations is

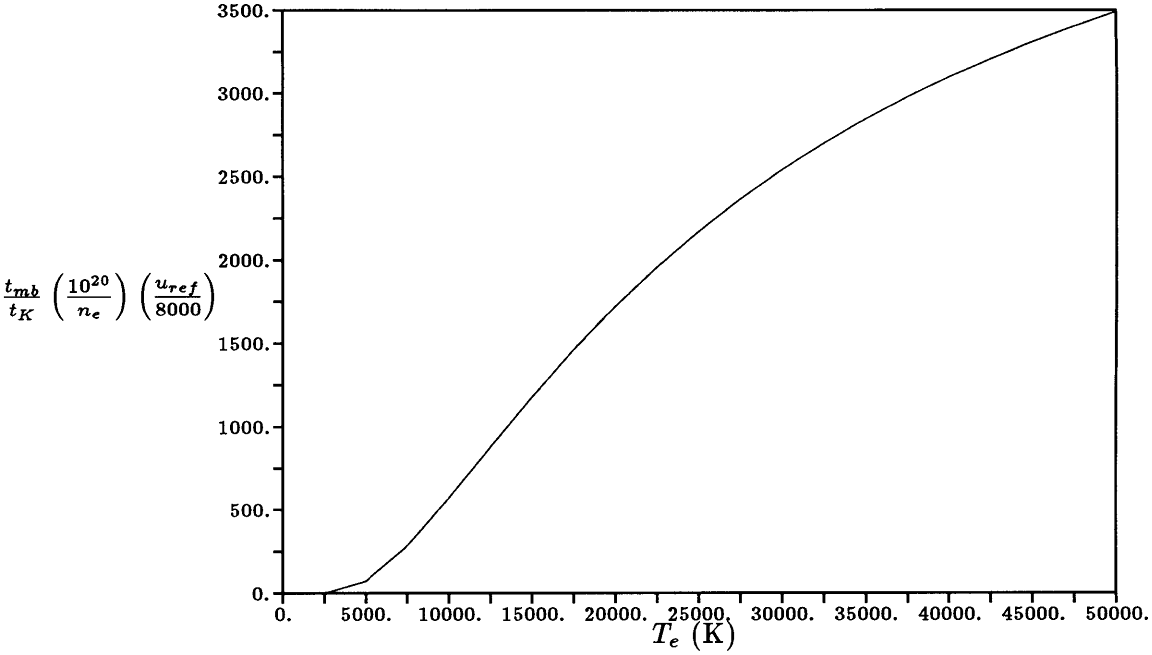

Figure 3.6: Argon atom, mks units. The ratio $\frac{t_{mb}}{t_K}$: bulk plasma conditions. This plot indicates that, under typical accelerator conditions, the assumption that $\dot{n}_{k>1} = 0$ is valid, and therefore the overall rate coefficients determined here can be used.

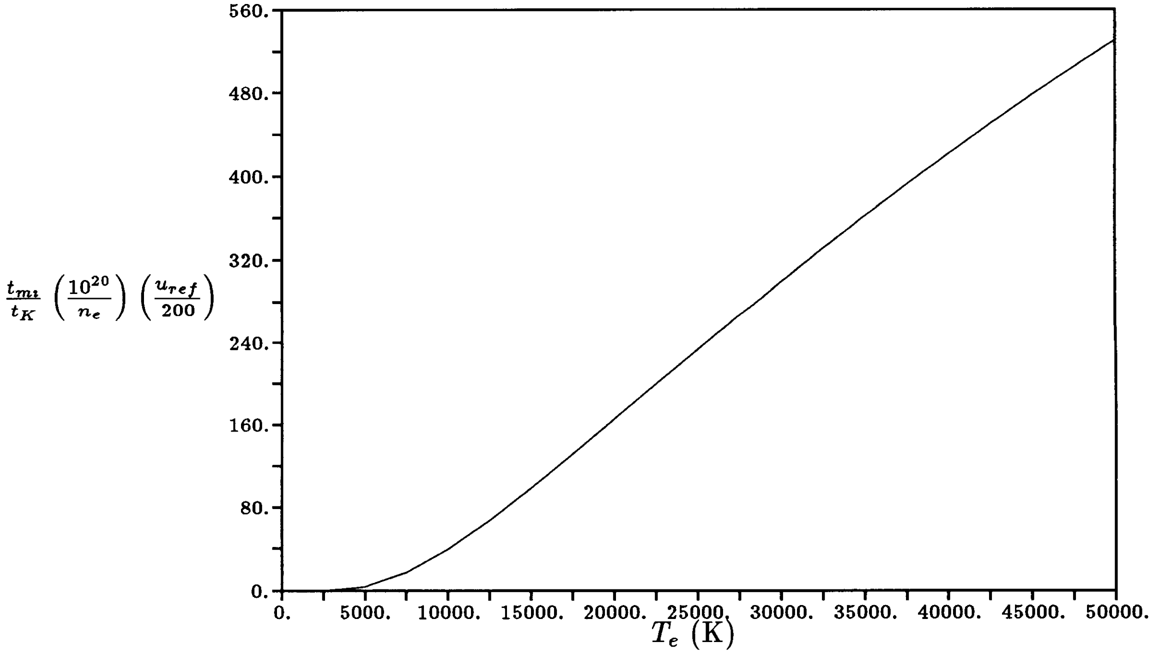

Figure 3.7: Argon atom, mks units. The ratio $\frac{t_{mi}}{t_K}$: inlet conditions. Again, the assumption that the excited states are dynamically balanced is good for the conditions anticipated at the inlet.

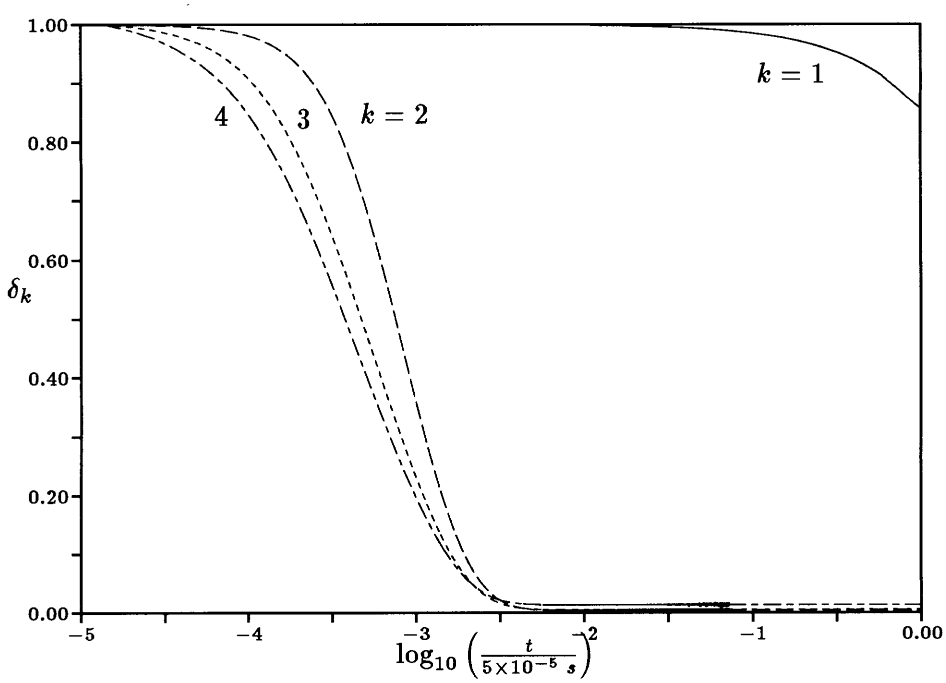

Figure 3.8: Argon atom, δ_k vs time for a multi-level perturbed plasma relaxing to equilibrium, at $T_e = 20000\ k$, $n_e = 10^{20}\ m^{-3}$, and initial condition that $\delta_k(t = 0) = 1$.

$$\frac{dn_s}{dt} = \dot{n}_s$$

where n_s is either one of the atomic levels (ground state or excited) or the continuum. This problem is expected to be quite stiff if the excited states time scales are indeed much smaller than that of the ground state. The integration is carried out from time $t = 0$ using a 4th order Kaps-Rentrop step routine for stiff equations which was adapted by Press and Teukolsky [57] for use with the one-dimensional marching drivers in *Numerical Recipes* [56].

The initial condition is somewhat arbitrary, although n_e and δ_k should be chosen so as to avoid both the frozen and equilibrium limits. The choice made here is $n_e = 10^{20}\ m^{-3}$, and $\delta_k(t = 0) = 1$ or $n_k = 2n_k^*$, at $T_e = 20000\ K$. Figure 3.8 shows the results for the first 4 levels (recall that $k = 1$ is the ground state, $k = 2$ is the first excited level, and so on). The excited states are seen to approach their equilibrium values much quicker than the ground state does - the excited level time scales are in fact three or four orders of magnitude less than the ground state's for the assumed conditions.

Having established that the time scale for the excited levels is much smaller than that of the ground state (which is tied to the MPDT mechanical time scales), we can assume that all the excited states are dynamically balanced (setting $\dot{n}_k/(n_e^2 n_i \approx 0$ to determine the population distribution, not to imply that it is frozen) and that only the ground state rates are on the order of convective and diffusive terms in the continuity equation. This condition is referred to as the quasi-steady-state-solution (QSSS) by van Der Sijde, et al. [71]. In this case, equation 3.20 could be used to solve for all of the δ_k as a function of the ground state, δ_1 in a form:

$$\delta_k = \chi_k(\bar{\beta}, n_e, T_e)\delta_1 + \psi_k(\bar{\beta}, n_e, T_e) \tag{3.21}$$

where $\bar{\beta}$ represents the matrix of escape factors, and ψ_k is entirely due to radiation escape, coming from the last line of equation 3.20. The density dependence comes from the fact that the radiative and collisional terms carry different powers of n_e.

This method allows the rate equations for the excited states to be solved independent of the ground state (or continuum) equations. The degree of nonequilibrium of the ground state, δ_1, is determined by the ion or the ground state continuity equation (assuming the electron density and total number density are known) which includes the effects of convection and diffusion. Equation 3.19 is now

$$\dot{n}_e = n_e^2 n_i \sum(\delta_1\chi_k + \psi_k)S_{ck} - n_e n_i \sum A_{ck}\beta_{ck} \tag{3.22}$$

Under the QSSS assumption, equation 3.20 yields the following equation, which can be used to calculate the coefficients χ_k and ψ_k:

$$\begin{aligned} 0 \quad = \quad & \left[\sum_{j\neq k} \frac{(\delta_1(\chi_j - \chi_k) + (\psi_j - \psi_k))S_{kj}}{S(s,k,T_e)} - (\delta_1\chi_k + \psi_k)S_{ck}\right] \\ + \quad & \left[\sum_{l>k} \frac{(\delta_1\chi_l + \psi_l)A_{lk}\beta_{lk}}{n_e S(s,l,T_e)} - \sum_{j<k} \frac{(\delta_1\chi_k + \psi_k)A_{kj}\beta_{kj}}{n_e S(s,k,T_e)}\right] \\ + \quad & \left[\frac{A_{ck}\beta_{ck}}{n_e} + \sum_{l>k} \frac{A_{lk}\beta_{lk}}{n_e S(s,l,T_e)} - \sum_{j<k} \frac{A_{kj}\beta_{kj}}{n_e S(s,k,T_e)}\right] \end{aligned} \tag{3.23}$$

This is a modified version of the law of mass action for each level k, with the influences of radiation and the degree of nonequilibrium of the ground state included.

3.3.1 Calculating Population Distributions

Ultimately, the goal of this analysis is the calculation of the overall ionization and recombination rate coefficients, but in order to include the influence of the excited states, it is necessary to find their population distribution (actually, the degree of nonequilibrium of each level) first. The population distribution of the excited states is now a function of δ_1, the electron temperature, and the set of radiative escape factors. In the formulation outlined above, the distribution was characterized by χ_k and ψ_k.

Without Radiation Effects

If radiation effects are dropped (equivalent to setting all of the escape factors in equation 3.23 to zero; physically, this would mean that all of the $A_{nm}\beta_{nm}/n_e$ factors in equation 3.23 are negligible), then all ψ_k are zero as well, and we have (assuming that $\delta_1 \neq 0$)

$$0 = \left[\sum_{j \neq k} \frac{(\chi_j - \chi_k) S_{kj}}{S(s,k,T_e)} - \chi_k S_{ck} \right] \tag{3.24}$$

Or the set of N equations, $k = 1, 2, ..., N$ (for a model with N excited levels, including the ground), to be solved for the χ_k factors:

$$\sum_{j \neq k} (\chi_j - \chi_k) S_{kj} = \chi_k S_{ck} S(s,k,T_e) \tag{3.25}$$

Recalling that, by definition, $\chi_1 = 1$, the equations may be solved for the other χ_k , and then from equation 3.21, the population distribution of all of the upper excited states relative to the ground may be obtained; ie,

$$\delta_k = \chi_k \delta_1 \quad \longrightarrow \quad \left(\frac{n_k}{n_k^*} - 1 \right) = \chi_k \left(\frac{n_1}{n_1^*} - 1 \right)$$

With Radiation Effects

Including the radiative effect introduces the electron dependence in the determination of the χ and ψ factors. The premise is that the coefficients, χ_k and ψ_k are independent of the state of the plasma itself, represented by δ_1. Therefore, referring to equation 3.23, the net coefficient of δ_1 and the net term not multiplied by δ_1 must be independently zero, leaving two sets of N equations for the $\chi_{k>1}$ and $\psi_{k>1}$ factors of the N excited states:

$$0 = \left(\left[\sum_{j \neq k} \frac{(\chi_j - \chi_k) S_{kj}}{S(s,k,T_e)} - \chi_k S_{ck} \right] + \sum_{l>k} \frac{\chi_l A_{lk} \beta_{lk}}{n_e S(s,l,T_e)} - \sum_{j<k} \frac{\chi_k A_{kj} \beta_{kj}}{n_e S(s,k,T_e)} \right) \tag{3.26}$$

$$\begin{aligned} 0 \;=\; & \left[\sum_{j \neq k} \frac{(\psi_j - \psi_k) S_{kj}}{S(s,k,T_e)} - \psi_k S_{ck} \right] + \sum_{l>k} \frac{\psi_l A_{lk} \beta_{lk}}{n_e S(s,l,T_e)} - \sum_{j<k} \frac{\psi_k A_{kj} \beta_{kj}}{n_e S(s,k,T_e)} \\ & + \frac{A_{ck} \beta_{ck}}{n_e} + \sum_{l>k} \frac{A_{lk} \beta_{lk}}{n_e S(s,l,T_e)} - \sum_{j<k} \frac{A_{kj} \beta_{kj}}{n_e S(s,k,T_e)} \end{aligned} \tag{3.27}$$

where now $\chi_{k>1}$ and $\psi_{k>1}$ depend on T_e *and* on the factors $A_{nm}\beta_{nm}/n_e$, which is the way that the electron density enters in these equations. In addition, $\chi_1 = 1$ and $\psi_1 = 0$.

3.3.2 Overall Rate Coefficients

Given the information about the populations of the excited states, it is possible to calculate the overall rate coefficients for ionization and recombination which can be used for the reaction rate model in an MPDT flow simulation. Although no radiative effects will be included in the final rate models used in flow problems, the influence of radiation will be considered in the analysis of this Chapter. What follows is a straightforward method to calculate these coefficients once the population distribution of the excited states has been characterized by the calculation of the χ_k and ψ_k values.

Atom Model

Applying equation 3.21 to equation 3.19, the continuum rate equation, and assuming that the number density of atoms is approximately equal to that of the ground state since the excited state populations are orders of magnitude less than the ground state's: $n_a \approx n_1$, then

$$\dot{n}_e = n_e^3 \sum (\delta_1 \chi_k + \psi_k) S_{ck} - n_e^2 A_{ck} \beta_{ck}$$

or, expanding the degree of nonequilibrium of the ground state,

$$\dot{n}_e = n_e^3 \left(\frac{n_1}{n_1^*} - 1 \right) \sum \chi_k S_{ck} + n_e^3 \sum \psi_k S_{ck} - n_e^2 A_{ck} \beta_{ck}$$

or, multiplying through,

$$\dot{n}_e = n_e^3 \frac{n_1}{n_1^*} \sum \chi_k S_{ck} - n_e^3 \sum \chi_k S_{ck} + n_e^3 \sum \psi_k S_{ck} - n_e^2 A_{ck} \beta_{ck}$$

Now, grouping terms,

$$\begin{aligned} \dot{n}_e &= n_e n_1 S(s,1,T_e) \sum_k \chi_k S_{ck} \\ & \quad - n_e^3 \sum_k [\chi_k - \psi_k] S_{ck} - n_e^2 \sum_k A_{ck} \beta_{ck} \end{aligned} \tag{3.28}$$

We can compare this with the standard form, equation 3.1. The corresponding overall rate coefficients, neglecting the radiative recombination term, are collisional ionization:

$$S_{ac} = S(s,1,T_e) \sum_k \chi_k S_{ck} \tag{3.29}$$

and collisional recombination:

$$S_{ca} = \sum_k [\chi_k - \psi_k] S_{ck} \tag{3.30}$$

and now the overall collisional ionization and recombination rate coefficients, S_{ac} and S_{ca}, respectively, depend on T_e and the $A_{nm}\beta_{nm}/n_e$ factors. In these summations, the reader should be reminded that $\chi_1 = 1$, $\psi_1 = 0$, by definition (see equation 3.21).

Formally, the radiative recombination term should be included in an overall recombination coefficient, so that the complete $\dot{n}_e$ may be written as $\dot{n}_e = n_e n_a S_{ac} - n_e^3 S'_{ca}$, where now,

$$S'_{ca} = \sum_k \left([\chi_k - \psi_k] S_{ck} + \frac{A_{ck}\beta_{ck}}{n_e} \right) \tag{3.31}$$

and the radiative part, $A_{ck}\beta_{ck}/n_e$, depends on n_e inversely as before. In fact, this is probably the preferred form in general, because there is no longer an absolute separation between "collisional" and "radiative" effects. The form in equation 3.30 is most directly applicable in the case of low $A_{nm}\beta_{nm}/n_e$, when radiative effects can be expected to be small.

It should be noted that, although the recombination terms, S_{ck} diverge as $k \to \infty$, the factors χ_k fall off fast enough with k so that the series will converge. Note also that equations 3.29 and 3.30 (or equation 3.31) show that overall microreversibility,

$$\frac{S_{ac}}{S_{ca}} = S(s, 1, T_e)$$

will only hold when the plasma is collisionally dominated: that is, when all $A_{kj}\beta_{kj}/n_e \ll \sum S_{kj}$, so that all $\psi_k = 0$.

Atom/Ion Combined Model

In the case where both atoms and ions are being ionized, then the approach is similar to that for atomic ionization alone. The difference is that now bookkeeping must account for the two different ion species. The volumetric rate equation for an ion of species s analogous to equation 3.22 is just

$$\dot{n}_i^s = n_e^2 n_i^s \sum (\delta_1^s \chi_k^s + \psi_k^s) S_{ck}^s - n_e n_i^s \sum A_{ck}^s \beta_{ck}^s \tag{3.32}$$

where the superscript s is the species index, and n_i^s is the number density of the next higher ion of species s, and the degree of nonequilibrium for each species is of the same form as used above:

$$\delta_k^s = \frac{n_k^s}{(n_k^s)^*} - 1$$

The volumetric rate equation for the ion of species s analogous to equation 3.23 is

$$\begin{aligned}
\dot{n}_k^s \quad = \quad & n_e^2 n_i^s \left[\sum_{j \neq k} \frac{(\delta_1^s(\chi_j^s - \chi_k^s) + (\psi_j^s - \psi_k^s))S_{kj}^s}{S(s,k,T_e)} - (\delta_1^s \chi_k^s + \psi_k^s) S_{ck}^s \right] \\
+ \quad & n_e n_i^s \left[\sum_{l>k} \frac{(\delta_1^s \chi_l^s + \psi_l^s) A_{lk}^s \beta_{lk}^s}{S(s,l,T_e)} - \sum_{j<k} \frac{(\delta_1^s \chi_k^s + \psi_k^s) A_{kj}^s \beta_{kj}^s}{S(s,k,T_e)} \right] \\
+ \quad & n_e n_i^s \left[A_{ck}^s \beta_{ck}^s + \sum_{l>k} \frac{A_{lk}^s \beta_{lk}^s}{S(s,l,T_e)} - \sum_{j<k} \frac{A_{kj}^s \beta_{kj}^s}{S(s,k,T_e)} \right] = 0
\end{aligned} \tag{3.33}$$

Equations 3.26 and 3.27 apply as well for each species, without modification, since the factor n_i^s appears in each term of equation 3.33. Therefore, the pair of equations are solved for each species to obtain the coefficients χ_k and ψ_k. The overall ionization rate coefficient for either the atom or ion species is

$$S_{ac}^s = \frac{n_e n_i^s}{(n_e n_i^s)^*} S(s, 1, T_e) \sum \chi_k^s S_{ck}^s \tag{3.34}$$

and the overall recombination rate coefficient (including the radiative recombination term) for each species is

$$(S_{ac}^s)' = \sum(\chi_k^s - \psi_k^s)S_{ck}^s + \frac{\sum A_{ck}^s\beta_{ck}^s}{n_e} \tag{3.35}$$

By conservation of charge,

$$\sum_s Z_i^s n_i^s = n_e$$

where $Z_i^s = q_i^s/e$, and q_i^s is the charge of the next higher ion of species s. Given n_e, this indicates another constraint on the first and second ion populations.

3.4 Three-Level CR Models

Now that the framework for calculating the population distribution of the excited states, and the overall rate coefficients has been set, it is possible to analyze the behavior of the plasma under a variety of conditions. In order to do so, a simple three-level species model consisting of the ground state (subscript 1), the first excited state (2) and the ion (c) will be used. The advantage of this model is that the χ_2 and ψ_2 terms can be found and calculated easily, and the resulting trends are easier to identify and interpret.

Recalling that $\delta_2 = \chi_2\delta_1 + \psi_2$, assuming that the excited state in a three-level model is in dynamic equilibrium is equivalent to solving the single linear equation: equation 3.23, for $k = 2$. This is

$$0 = \frac{[\delta_1(\chi_1 - \chi_2) + (\psi_1 - \psi_2)]S_{21}}{S(s,2,T_e)} - (\delta_1\chi_2 + \psi_2)S_{c2}$$

$$-\frac{(\delta_1\chi_2 + \psi_2)A_{21}\beta_{21}}{n_e S(s,2,T_e)} + \frac{A_{c2}\beta_{c2}}{n_e} - \frac{A_{21}\beta_{21}}{n_e S(s,2,T_e)}$$

Section 3.3.1 presents the general expressions used to find the rate coefficients. In this case, the two resulting equations are, assuming that $\delta_1 \neq 1$:

$$0 = \frac{(\chi_1 - \chi_2)S_{21}}{S(s,2,T_e)} - \chi_2 S_{c2} - \frac{\chi_2 A_{21}\beta_{21}}{n_e S(s,2,T_e)}$$

$$0 = \frac{(\psi_1 - \psi_2)S_{21}}{S(s,2,T_e)} - \psi_2 S_{c2} - \frac{\psi_2 A_{21}\beta_{21}}{n_e S(s,2,T_e)} + \frac{A_{c2}\beta_{c2}}{n_e} - \frac{A_{21}\beta_{21}}{n_e S(s,2,T_e)}$$

and, solving for χ_2 and ψ_2, with $\chi_1 = 1$, $\psi_1 = 0$ by definition, and $S_{c2}S(s,2,T_e) = S_{2c}$ via microreversibility,

$$\chi_2\left(T_e, \frac{A_{nm}\beta_{nm}}{n_e}\right) = \frac{S_{21}}{S_{21} + S_{2c} + \frac{A_{21}\beta_{21}}{n_e}} \tag{3.36}$$

$$\psi_2\left(T_e, \frac{A_{nm}\beta_{nm}}{n_e}\right) = \frac{-A_{21}\beta_{21} + A_{c2}\beta_{c2}S(s,2,T_e)}{n_e\left(S_{21} + S_{2c} + \frac{A_{21}\beta_{21}}{n_e}\right)} \tag{3.37}$$

The electron density dependence is due entirely to the radiation effects. At the limits: $n_e \to 0$, $\chi_2 = 0$, $\psi_2 = -1 + (A_{c2}\beta_{c2}S(s,2,T_e))/(A_{21}\beta_{21})$; $n_e \to \infty$, $\chi_2 = S_{21}/(S_{21} + S_{2c})$, $\psi_2 = 0$.

Next, to take a more direct look at the effect of radiation on the overall rate coefficients, consider the ratio of the overall recombination coefficient with radiation divided by that without radiation. Using equation 3.30, the overall recombination coefficient for no radiative effects (all $A_{kj}\beta_{kj}/n_e \ll \sum S_{kj}$) for the three-level model is:

$$(S_{ca})_{nr} = S_{c1} + \chi_2^{nr}S_{c2} = S_{c1} + \frac{S_{c2}S_{21}}{S_{21} + S_{2c}}$$

and the overall recombination coefficient, including radiative effects, following equation 3.31, is

$$\begin{aligned}(S_{ca}')_r &= S_{c1} + (\chi_2^r - \psi_2^r)S_{c2} + \frac{A_{c1}\beta_{c1} + A_{c2}\beta_{c2}}{n_e} \\ &= S_{c1} + \frac{S_{c2}S_{21} + (A_{21}\beta_{21} - A_{c2}\beta_{c2}S(s,2,T_e))/n_e}{\left(S_{21} + S_{2c} + \frac{A_{21}\beta_{21}}{n_e}\right)} + \frac{A_{c1}\beta_{c1} + A_{c2}\beta_{c2}}{n_e}\end{aligned}$$

$$R = \frac{(S_{ca}')_r}{(S_{ca})_{nr}}$$

This fraction, R, is an indication of the effects of radiation on the overall recombination coefficient (When radiative effects are negligible, $R \approx 1$). In general, R can be written as

$$R = \frac{1 + f_c(1 + f_r)}{1 + f_c}$$

where the collisional and radiative factors are, respectively,

$$f_c = \frac{S_{c2}S_{21}}{S_{c1}(S_{21} + S_{2c})}$$

$$f_r = \frac{A_{21}\beta_{21} - A_{C2}\beta_{c2}S(s,2,T_e)}{n_e S_{21}}$$

The difference between the overall rate coefficients relative to the no-radiation coefficient is a more useful variable. This is $R - 1$:

$$R - 1 = \frac{f_c f_r}{1 + f_c} \tag{3.38}$$

The relative difference is small under two conditions. The first case is when f_r goes to zero, regardless of the value of f_c, or the radiative terms are much smaller than the collisional ones. This corresponds to high electron density, and/or high electron temperature. The second case is when f_c goes to zero. This corresponds to all of the ionization coming from the ground state, so there is no radiation effect, because no excited states are involved.

3.4.1 Results From A Three-Level Atomic Argon Model

Figures 3.9 and 3.10 show $\log_{10}\chi_2$ and ψ_2 for the argon atom as a function of T_e and n_e. χ_2 is an indication of the collisional coupling between the ground and the excited state, and ψ_2 is the radiative coupling. Using $\beta_{k1} = 0.01$ here corresponds to a fairly thick (optically) environment (only 1 percent of the emitted line is not reabsorbed locally). The radiative escape factor for continuum-excited state radiation is taken to be one.

Figure 3.11 is the overall recombination coefficient (S'_{ca}) corresponding to the χ_2, ψ_2 plots. (The Drawin cross-sections are used to calculate the collisional rate coefficients.)

3.4.2 Results From A Three-Level Atomic Hydrogen Model

Figures 3.12 and 3.13 show $\log_{10}\chi_2$ and ψ_2, now for the hydrogen atom as a function of T_e and n_e. Again, $\beta_{k1} = 0.01$, and the radiative escape factor for continuum-excited state radiation is taken to be one.

Figure 3.14 is the overall recombination coefficient (S''_{ca}) corresponding to the χ_2 plot. (The Drawin cross-sections are used to calculate the collisional rate coefficients.)

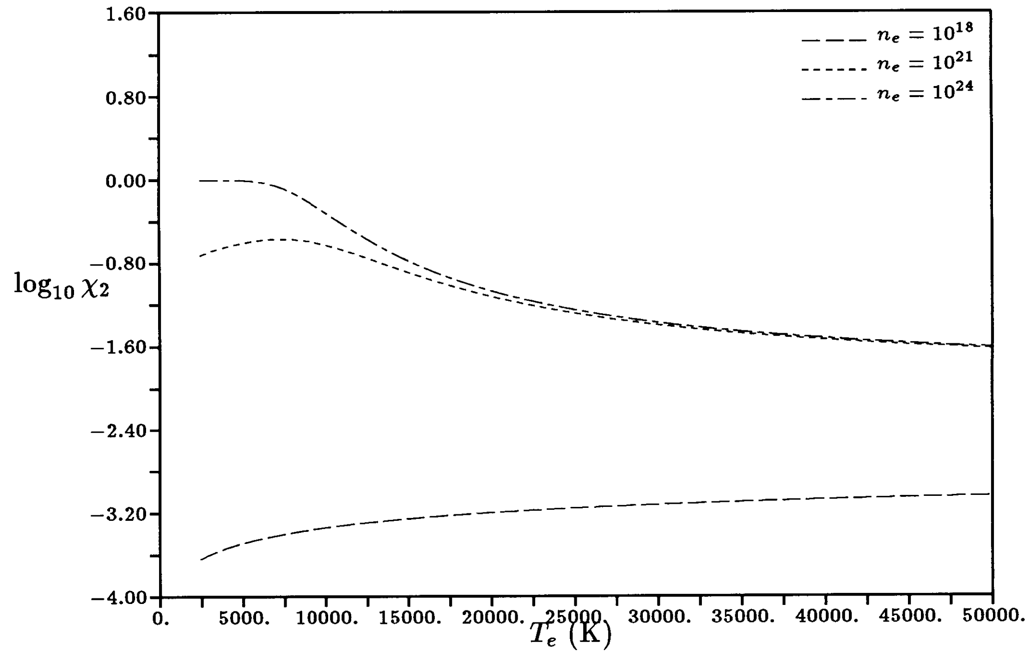

Figure 3.9: Argon atom, three-level model: χ_2 vs T_e. (mks units) Note that the effect of radiation is the electron number density dependence. The first excited state is strongly coupled to the ground state via collisions at low temperatures and is more strongly coupled to the electrons at higher temperatures.

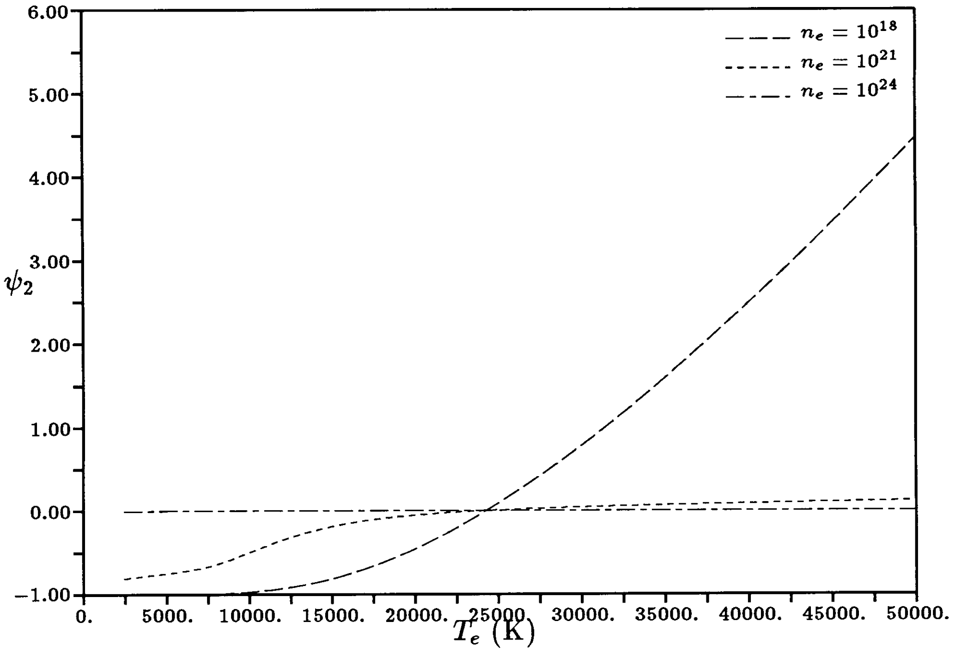

Figure 3.10: Argon atom, three-level model: ψ_2 vs T_e (mks units) Again, note the n_e dependence. At $n_e = 10^{18}$ m^{-3}, the radiating level (level 2, the first excited state) is heavily depleted (χ_2 is low, $\psi_2 \approx -1$; $\delta_2 = \frac{n_2}{n_2^*} - 1$ is close to -1) at low n_e and T_e in order to maintain the $\dot{n}_2 = 0$ balance.

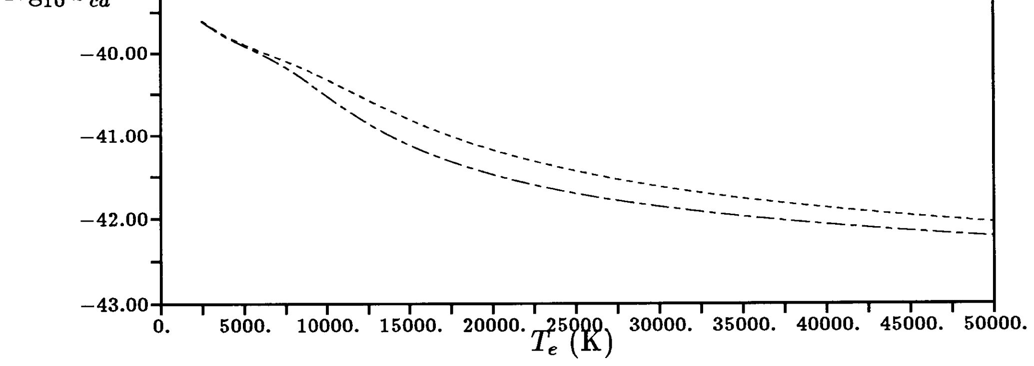

Figure 3.11: Argon atom, three-level model: Overall recombination coefficient (mks units).

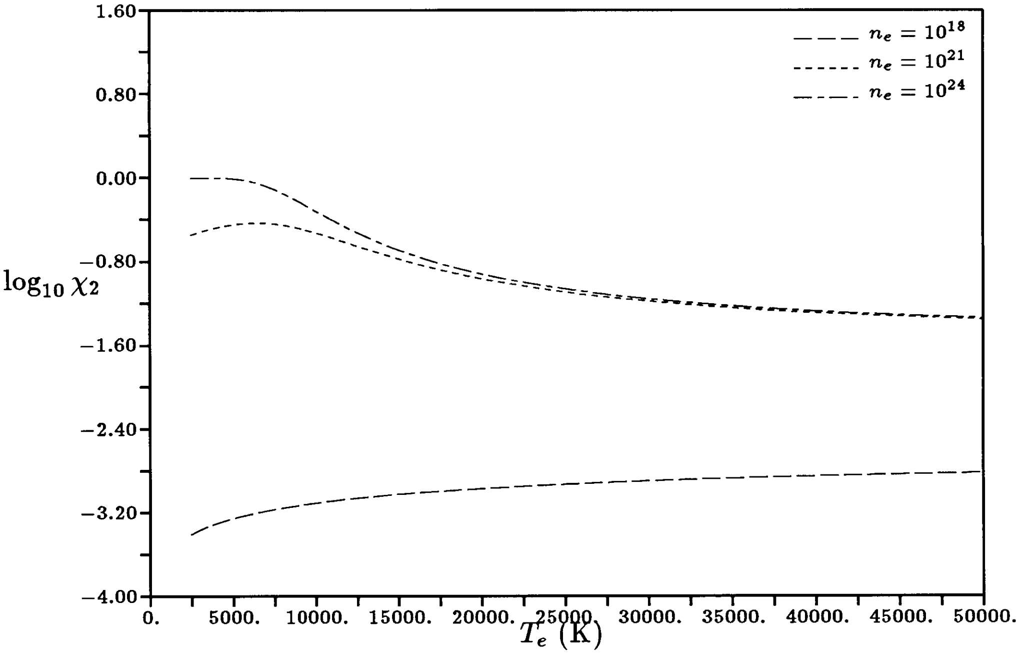

Figure 3.12: Hydrogen atom, three-level model: χ_2 vs T_e. (mks units)

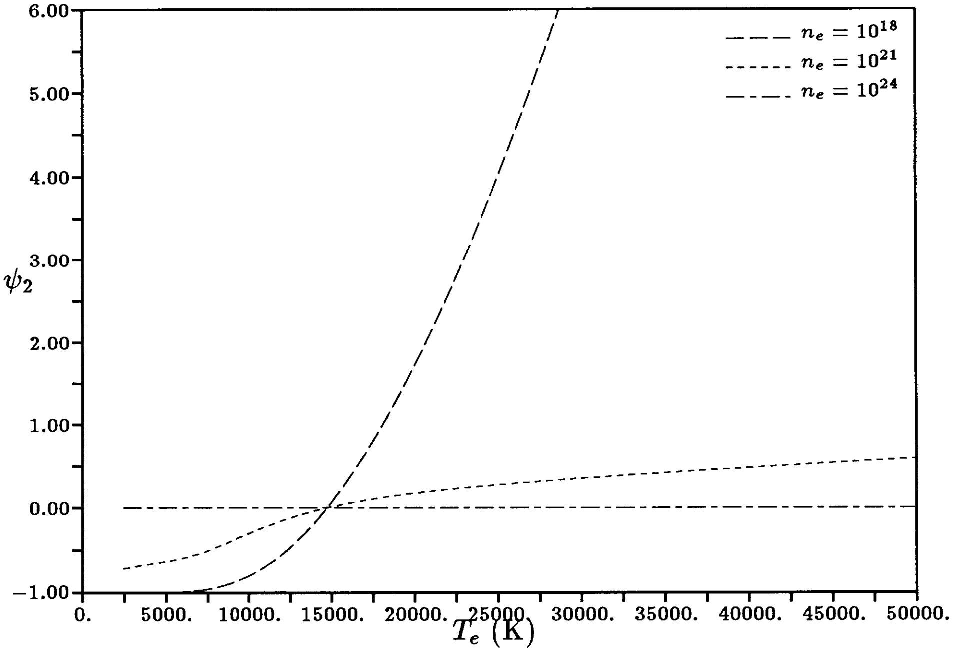

Figure 3.13: Hydrogen atom, three-level model: ψ_2 vs T_e (mks units)

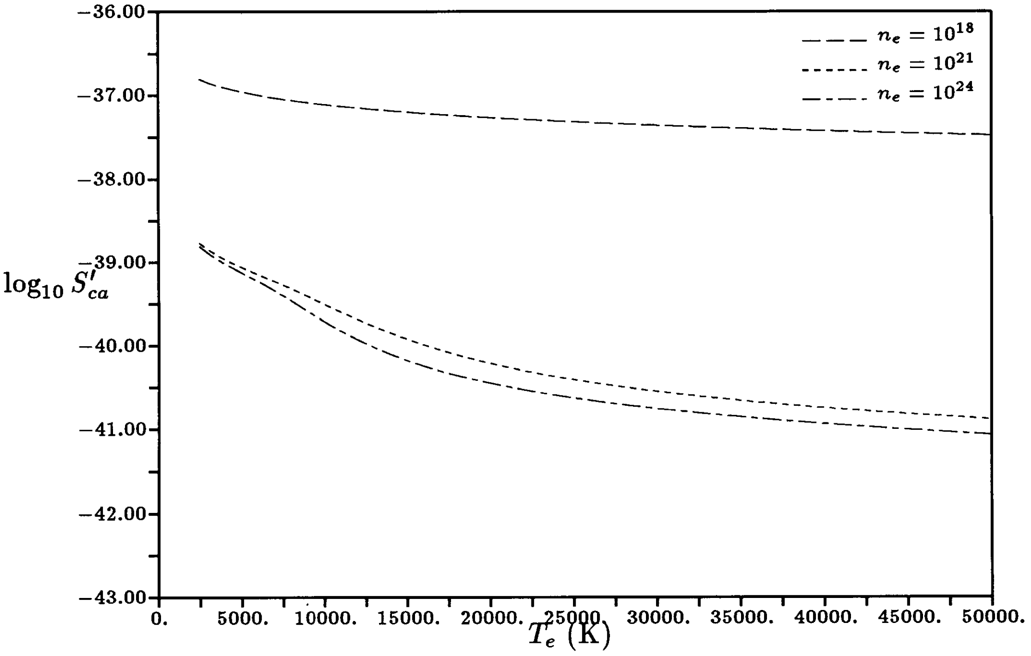

Figure 3.14: Hydrogen atom, three-level model: Overall recombination coefficient (mks units).

3.5 Multi-level Model Results

In what follows we will show specific examples of calculated excited state distributions and of the recombination rates which should result from them. Solution of the kinetic balance equations for each of the excited states and the continuum requires independent information about the driving terms, namely, the spatial and temporal derivatives, as well as the diffusive and catalytic wall losses. In a stationary plasma (e.g. a discharge tube), only the latter would be significant; in an MPD flow, at least the convective derivative would also be required, and they must be generated in the course of a broader numerical calculation of the flow.

Appendix B contains details about the levels used in the various models used in this work. The levels used are not necessarily the actual electronically excited states, but lumped levels.

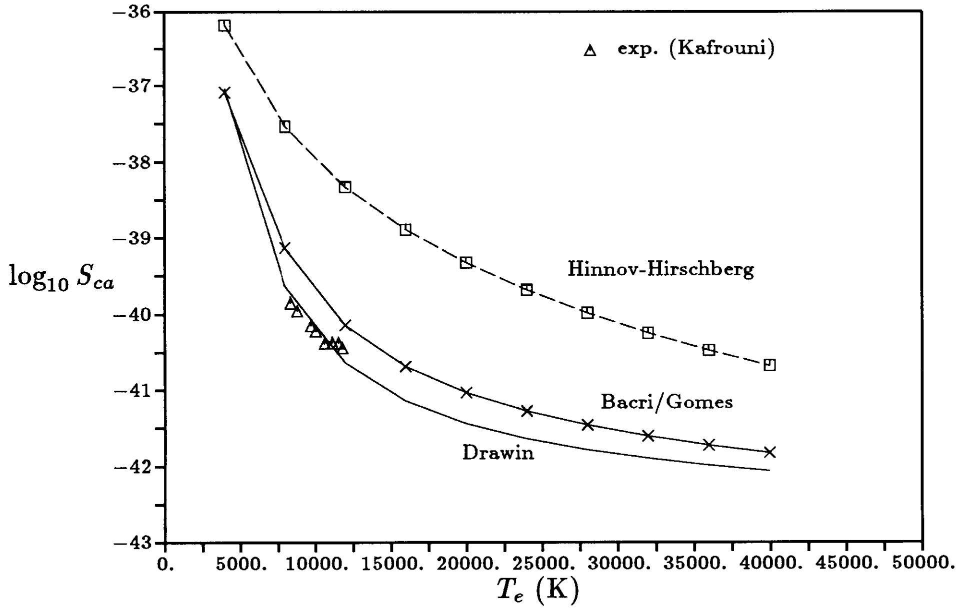

Figure 3.15: Argon atom, multi-level model: Overall recombination coefficient (mks units). The curve using the Drawin cross-sections does not include forbidden transitions. The Bacri/Gomes curve does. The experimental data is from Kafrouni.

3.5.1 Overall Rate Coefficients

Argon Atom

Figure 3.15 contains plots of the argon atom overall recombination coefficient (overall microreversibility applies in this case in calculating the ionization rate coefficient) vs T_e via three methods: the Hinnov-Hirschberg model (for reference), and two multi-level argon (atom only) rate models.

The Hinnov-Hirschberg results are several orders of magnitude above the argon model at higher temperatures. The H-H model was derived for hydrogenic atoms at electron temperatures below 3000 K, so that it is not a good choice for a wide temperature range, although it has been used here at the SPPL and elsewhere. The argon atom results using the Drawin cross-section model have been curve-fitted to arrive at an overall recombination coefficient (useful up to $T_e = 50000K$):

$$S_{ca} = 8.25 \times 10^{-43} \exp\left(\frac{(\ln(\frac{T_e}{1000}) - 3.95)^2}{0.6144}\right) \frac{m^6}{s} \tag{3.39}$$

This compares favorably with the results reported by Owano, et al. [52], who used

S_{ca}	$T_e(K)$ 10000	 20000	 40000
this work	6.84×10^{-41}	3.63×10^{-42}	9.22×10^{-43}
Owano	6.10×10^{-41}	3.15×10^{-42}	5.87×10^{-43}

Table 3.3: Collisional rate coefficients for three-body recombination in argon: comparison of the results of this work and those of Owano. The units of S_{ca} are m^6/s.

a spectroscopic analysis of the recombination rate in a flowing argon plasma to adjust a theoretical result. They found the overall three-body electron-ion recombination coefficient to be

$$S_{ca}^{Owano} = 3.3 \times 10^{-44} \left(\frac{135300}{T_e} + 2\right) \exp\left(\frac{47800}{T_e}\right) \quad \frac{m^6}{s} \qquad (3.40)$$

The overall recombination is made up of the contributions from the ground state and each of the excited states. In the non-radiative effect case, this is

$$S_{ca} = \sum_k \chi_k S_{ck}$$

In figure 3.16, the ratio $\chi_k S_{ck}/S_{ca}$ is plotted vs k for 4 temperatures. This ratio is the percentage of the overall recombination due to a particular level, k. Note that at the lower temperature (5000 K), the ground state contribution is very low, and that the major contribution comes from the higher excited states. As the temperature increases, the ground state's relative contribution increases, and at 40000 K, more than half of the overall recombination coefficient is due to the ground state. To accentuate the fact that the levels close to the continuum are the main contributors at low temperatures, figure 3.17 shows the $T_e = 5000\ K$ case vs E_k. Gonzales [25] calculated the same ratio for the individual vibrational states for $O_2 - Ar$ dissociation collisions. In that case, the biggest contribution over the temperature range of $4000 - 12000\ K$ came from the vibrational levels whose energies were about half the dissociation energy.

Figure 3.18 is a plot of the overall collisional recombination coefficients calculated in this work using the Drawin cross-sections as compared with both experimental and calculated values. The experimental results are from the work of Kafrouni [34], and the compilation of

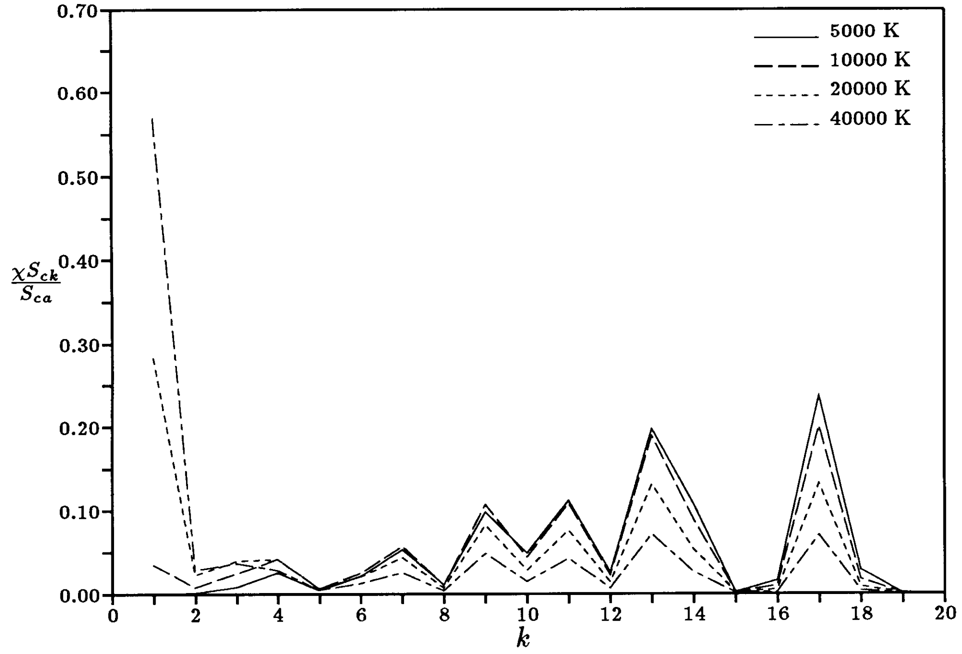

Figure 3.16: Argon atom, multi-level model: plot of $\chi_k S_{ca}/S_{ca}$ vs k at various electron temperatures.

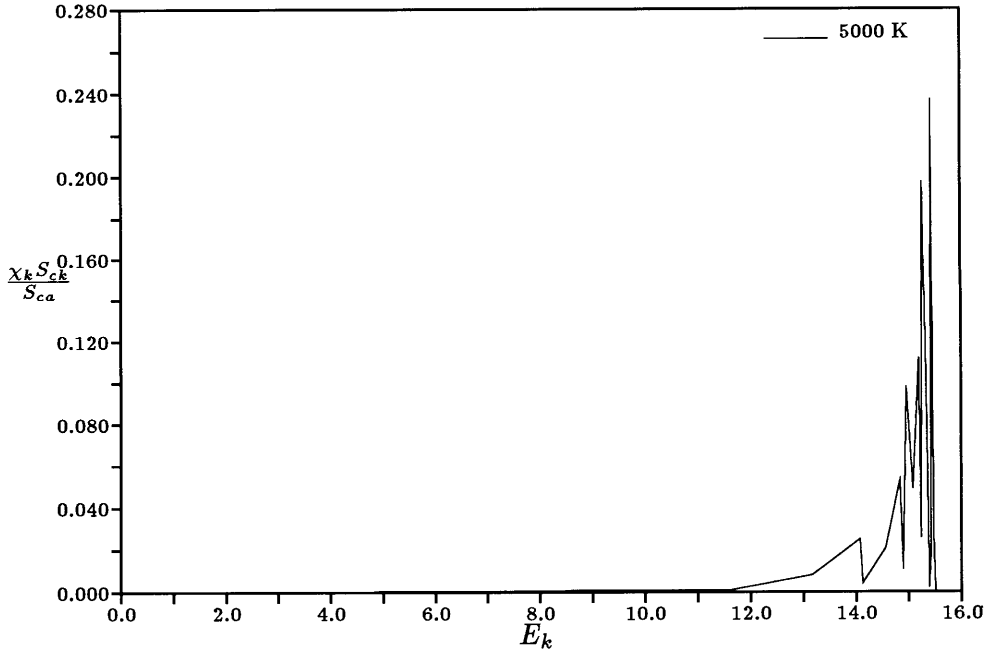

Figure 3.17: Argon atom, multi-level model: plot of $\chi_k S_{ca}/S_{ca}$ vs E_k at $T_e = 5000\ K$.

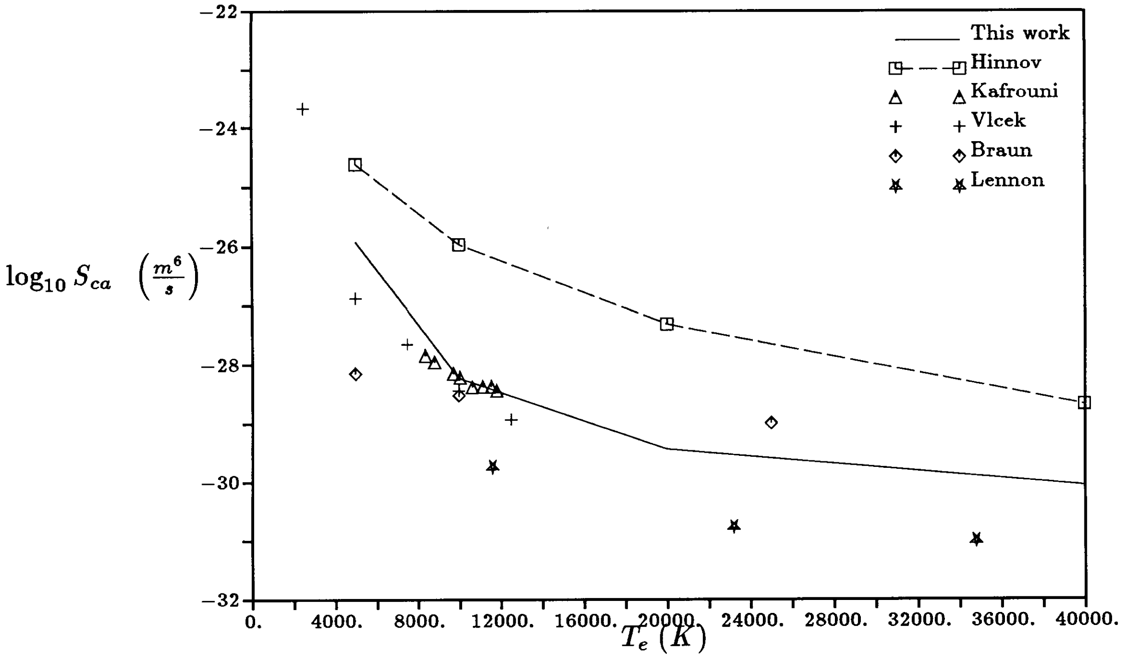

Figure 3.18: Argon atom, multilevel results comparèd to the experimental results published by both Kafrouni and Lennon, the results of a 65-level argon CR model by Vlcek, the Hinnov-Hirschberg theoretical formula, and Braun and Kunc's three-level CR model.

Lennon, et al. [43]. There is a great deal of scatter in the measured rate coefficients which makes it difficult to judge the accuracy of the numerical results The Hinnov-Hirschberg theoretical formula [29] for the species independent recombination coefficient, applicable at electron temperatures below roughly 3000 K, is also shown, for reference. Published results from a three-level argon model from Braun and Kunc [11] and a 65-state CR argon model from Vlcek and Ferdinand [73] are also shown. There is a great deal of scatter, but the results from this thesis agree reasonably well (within an order of magnitude) with the experiments of Kafrouni and the calculations of Vlcek at the lower temperatures, and appears to follow the trend of the Lennon data at higher temperatures, although Lennon's results seem to be low by an order of magnitude.

Argon Ion

A 33-level second ionization model for argon was also developed, and the overall three-body recombination coefficient (from the second argon ion down to the ground state of the first argon ion) calculated. Note that the gap between the highest excited state used and the

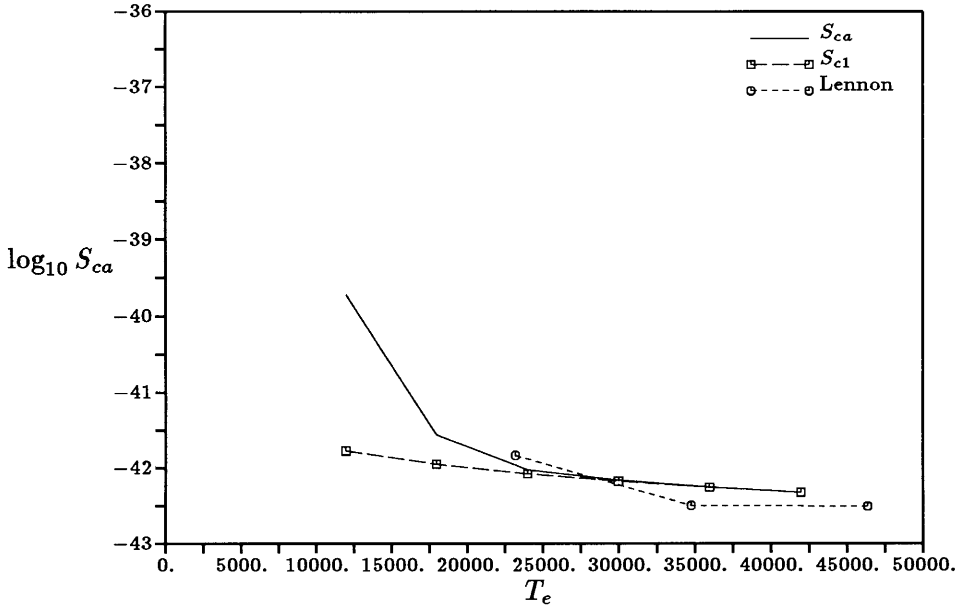

Figure 3.19: Argon ion, multi-level model: Overall recombination coefficient (mks units), using the Drawin cross-sections. Preliminary comparison to the recommended rates of Lennon, based on experiments, et al. seems reasonable.

ion is 2.77 eV. This is a weakness at low T_e, as the low temperature behavior depends on the missing upper levels, but at lower temperatures, second ions should not be of much significance.

$$S_{ci} = 7.17 \times 10^{-40} \exp\left(-\frac{(\ln(\frac{T_e}{1000}) - 1.3485)^2}{0.9293}\right) \frac{m^6}{s} \tag{3.41}$$

Figure 3.19 is a plot of the overall recombination coefficient for the argon ion, S_{ci}, and the ionization coefficient for the ground state of the ion alone, S_{c1}. The full model result, S_{ci}, matches well with S_{c1} at temperatures above 25000 K, which indicates that none of the excited states of the argon ion contribute significantly to the overall production of second ions at $T_e > 25000\ K$. Also plotted are experimental results from the compilation of Lennon, et al. [43], which show good agreement with the calculations.

Hydrogen Atom

A 20-level model was used to calculate the overall rate coefficients for the hydrogen atom. Figure 3.20 contains plots of the hydrogen overall recombination coefficient. In this case, the Drawin curve has been curvefit by the following formula (good up to $T_e = 60000K$):

$$S_{ca} = 6.985 \times 10^{-42} \exp\left(\frac{(\ln(\frac{T_e}{1000}) - 4.0883)^2}{0.8179}\right) \frac{m^6}{s} \tag{3.42}$$

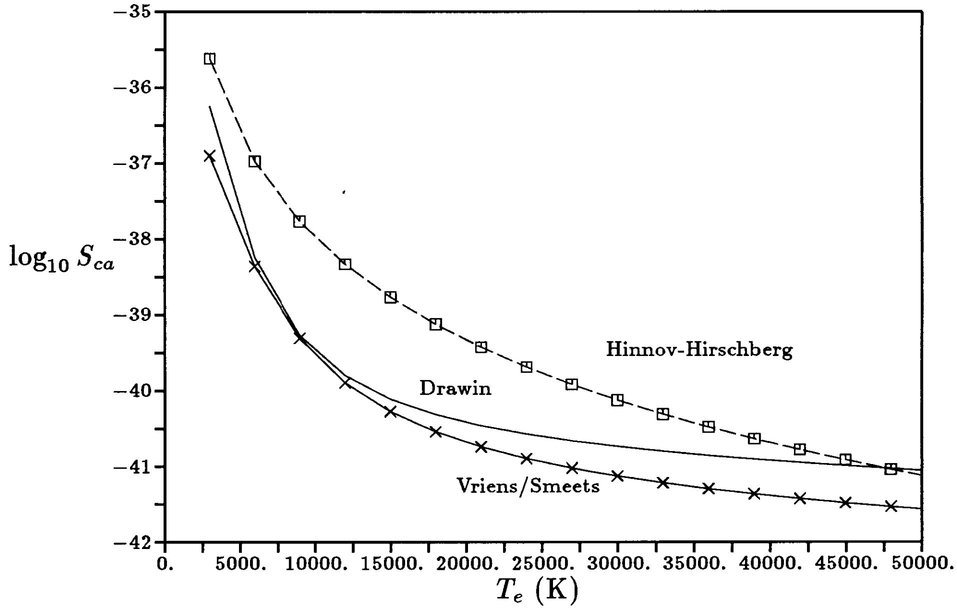

Figure 3.20: Hydrogen atom, multi-level model: Overall recombination coefficient (mks units). The curve using the Drawin cross-sections does not include forbidden transitions. The curve which uses the Vriens and Smeets (1980) rate model does.

3.6 Summary

In this chapter, the standard Collisional-Radiative (CR) volumetric production rate equations have been recast into a more convenient form which highlights each excited level's relative degree of nonequilibrium. If the excited levels can be assumed to be in dynamic equilibrium (the QSSS assumption) - and they have been shown to be so under the conditions of interest here - then the overall ionization and recombination rate coefficients may be calculated. If there are no radiative effects, then the coefficients are dependent on T_e only, and overall microreversibility applies. A comparison of the relative contribution of each level to the overall recombination rate showed that, at high temperatures, the ground state contributes the most, while at temperatures below about 15000 K, the upper levels dominate.

The overall recombination coefficients for the argon atom and first ion, and the hydrogen atom have been calculated using multi-level models, with no radiative effects. The atomic rate models will be used in Chapter 4 in the analysis of ionizational ignition in MPDTs.

Chapter 4

The Initiation of Ionization In MPD Thrusters

As stated in the introduction, there have been several experimental observations that there is a mm-scale ionization region at the inlet of self-field magnetoplasmadynamic devices. Other experiments have noted a "dissociation lag" with molecular propellants, which indicates that there is a species-dependent ignition criterion.

Steady-state initiation of ionization over a finite length at the inlet of an MPD thruster, defined here as "ignition", may in general include the effects of metastable states, multi-step ionization, radiation and back-diffusion of energetic particles in addition to the more familiar fluid dynamic and magnetic field behaviors. The purpose of this work will be to characterize the possible effects of each of the processes, and judge their scales, within the context of a numerical simulation of the inlet flow. Radiation has been dropped here due to the short absorption length scale (or small radiative escape factors), and because Burton and Tiliakos [14] noted that radiation only played a role at ionization fractions lower than those found in this study. The multi-step and metastable effects are included in the rate model as indicated in Chapter 3. Ambipolar back-diffusion is assumed here to be the main mechanism responsible for ignition.

Three models will be considered. First, a simple constant speed and temperature model will be used to present the general findings. Next, the electron temperature is allowed to vary in a constant speed model. Finally, the effects of acceleration on ignition are considered in a constant temperature model, although an overall energy balance will be found to be

Injection	Species	Electron Thermal Conductivity	Acceleration
atomic	argon	∞	no
atomic	argon	K_e	no
atomic	argon	∞	yes

Table 4.1: Ignition Cases

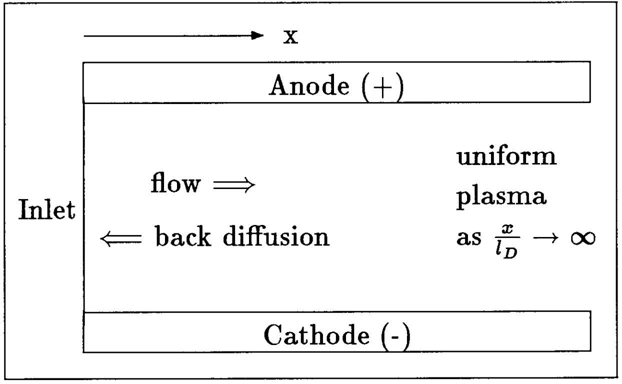

Figure 4.1: 1-D Thruster Inlet Region

necessary to make the problem self-consistent. These cases are listed in table 4.1. (infinite electron thermal conductivity implies constant T_e)

Injection of atomic argon into the thruster channel will be considered, through a porous backplate to ensure 1-D bulk flow. Figure 4.1 shows the general configuration of the inlet region. Since the hypothesis of this work is that back-diffusion of electron-ion pairs sustains ignition, the characteristic scale length of the ionization region is expected to be the back diffusion length, $l_D \ll L$, defined below.

4.1 The Constant Speed Isothermal Case in Argon

In this section, the simplest case of 1-D injection (for example, this is injection through a porous backplate) is assumed. In addition, constant temperature and constant speed are assumed. While these assumptions are somewhat restrictive, the model does yield interesting results which have some bearing on more realistic models.

It is assumed that the ions reach the inlet wall moving upstream at the Bohm velocity, and enter a sheath, which will not be modeled here. This is the key assumption in this analysis, as it makes the ionization region a "pre-sheath". It will also be assumed that, far downstream (on the diffusion length-scale) that there is a uniform plasma, which is approached asymptotically. These two assumptions set the boundary conditions for the problem.

In this case, the bulk speed, u is constant, and the overall continuity equation is

$$(n_e + n_a)u = n_g u = G = \frac{\dot{m}}{Am_i} \tag{4.1}$$

where n_g is the total number density of of nuclei, (n_g is the total number density of heavy (ion and atom) particles; for constant speed, n_g is also constant), n_a is the number density of atoms, n_e is the number density of electrons and u is the bulk speed. The mass flow rate is $\dot{m}$, the channel area is A, and the nucleus mass is m_i. The ionization fraction is defined as $\alpha \equiv n_e/n_g$. Since this is a quasi-neutral plasma, and only singly ionized species are assumed to exist, $n_e = n_i$, where n_i is the number density of the ions. The ion continuity equation is

$$\frac{dn_e u}{dx} = -\frac{dn_e V_i}{dx} - \frac{D_a n_e}{h^2} + \dot{n}_e \tag{4.2}$$

where $n_e V_i$ is given generally by equation 2.22. In equation 4.2, the transverse ambipolar diffusion, $\frac{D_a n_e}{h^2}$, is included (with an assumed parabolic distribution of n_e in the transverse direction so that h is actually $\frac{1}{\sqrt{12}}$ of the actual channel height, $H \approx 0.02m$.) in order to allow a balance to be struck far downstream of the ionization layer. For the nonaccelerating case, axial ion-slip is characterized by Fick's Law, equation 2.21:

$$\frac{d\alpha}{dx} = -\frac{n_e V_i}{C_a} \equiv \frac{\Gamma}{C_a} \tag{4.3}$$

The ion continuity equation (with $n_e = n_i$) is then:

$$u\frac{dn_e}{dx} = D_a \frac{d^2 n_e}{dx^2} + \dot{n}_e - \frac{D_a n_e}{h^2} \tag{4.4}$$

The ionization fraction varies from some small value at the wall to its asymptotic value (on the order of unity) as $\xi \to \infty$. It is therefore convenient to use α as the independent variable. Dividing 4.4 by equation 4.3 leaves the following form of the ion continuity equation:

$$\frac{d\Gamma}{d\alpha} = G - \frac{D_a n_g}{\Gamma} n_g \alpha \left(S_{ac} n_g (1-\alpha) - S_{ca} n_g^2 \alpha^2 - \frac{D_a}{h^2} \right) \tag{4.5}$$

nondimensionalizing equation 4.5, with $\gamma = \Gamma / G$, results in

$$\frac{d\gamma}{d\alpha} = 1 - \frac{\Lambda_1 \alpha [(1-\alpha) - \alpha^2 \Lambda_2 - \Lambda_3]}{\gamma} \tag{4.6}$$

where the factors Λ_1, Λ_2, and Λ_3 are

$$\Lambda_1 = \frac{C_a S_{ac} n_g^2}{G^2} = \frac{C_a S_{ac}}{u^2} = \frac{l_D}{l_{ion}} \tag{4.7}$$

$$\Lambda_2 = \frac{S_{ca} n_g}{S_{ac}} = \frac{n_g}{S(1, T_e)} = \frac{1-\alpha_{eq}}{\alpha_{eq}^2} \tag{4.8}$$

$$\Lambda_3 = \frac{C_a}{S_{ac}(n_g h)^2} = \frac{l_D l_{ion}}{h^2} \tag{4.9}$$

The parameter Λ_1 is a Damkohler number, the ratio of the diffusion time scale to the ionization time scale [23], or of the length scales, if the same characteristic speed applies (as it does here: the characteristic axial speed). Frozen flow is represented by a Damkohler coefficient of zero, and equilibrium flow is approached when the Damkohler coefficient is infinite. Note that in equation 4.6, the transverse diffusion term appears amongst the terms multiplied by Λ_1 so that $\Lambda_1 \to \infty$ forces the balance $(1 - \alpha - \alpha^2 \Lambda_2 - \Lambda_3) = 0$ rather than the equilibrium balance: $(1 - \alpha - \alpha^2 \Lambda_2) = 0$. However, large Damkohler numbers are caused by large temperatures and/or low speeds, and since S_{ac} varies faster with T_e than C_a, and low speed is high density for fixed $G = n_g u$, large Λ_1 implies small Λ_3.

As will be shown, Λ_1 should be of roughly $O(1)$ or greater for ignition in a finite distance. The diffusion length is thus a good choice for the characteristic length of the ionizing region.

The parameter Λ_2 was found first in section 3.1 to be the single parameter which determines the equilibrium ionization fraction. The last parameter, Λ_3 represents the transverse diffusion loss term, and $\Lambda_1 \Lambda_3 = l_D^2 / h^2$, the square of the ratio of the axial to transverse length scales.

As discussed above, at the inlet wall, it is assumed that the ions approach the wall at the Bohm velocity (in the negative streamwise direction). This is: $n_e u_i = n_e(u + V_i) = -n_e v_B$, or, using Fick's law, equation 2.21, for the slip $(n_e V_i = \Gamma)$:

$$\Gamma = n_e(u + v_B) \tag{4.10}$$

In the nondimensional variables, this is

$$\gamma = \alpha\left(1 + \frac{v_B}{u}\right) \tag{4.11}$$

which sets α at the inlet wall, and indeed fixes the location of the inlet wall relative to the uniform plasma downstream. Recall the constraint that the sum of the ion and neutral slip fluxes is zero which was imposed in the derivation of the ion slip flux in section 2.2.1. This then fixes the neutral slip at the inlet wall, which includes the injected neutrals and neutrals newly formed by recombination at the inlet wall of ions with electrons.

The second boundary condition comes from the requirement that the derivative be smooth as the downstream uniform plasma is approached so that the numerator of the fraction in equation 4.6 is zero at the $\xi = \infty$, $\gamma \to 0$ singularity, or

$$1 - \alpha_\infty - \alpha_\infty^2 \Lambda_2 - \Lambda_3 = 0 \tag{4.12}$$

which sets α_∞. Physically, this means that the balance, $\dot{n}_e = \frac{D_a n_e}{h^2}$, is approached smoothly as $\xi \to \infty$, and the asymptotically approached ionization fraction is

$$\alpha_\infty = \frac{1}{2\Lambda_2}\left[\sqrt{1 + 4\Lambda_2(1 - \Lambda_3)} - 1\right] \tag{4.13}$$

As reference, for the equilibrium balance (collisional ionization equals collisional recombination), the ionization fraction is similar:

$$\alpha_{eq} = \frac{1}{2\Lambda_2}\left[\sqrt{1 + 4\Lambda_2} - 1\right] \tag{4.14}$$

When $\Lambda_2(1 - \Lambda_3)$ is small (recombination not significant), in equation 4.13, then $\alpha_\infty \approx (1 - \Lambda_3)$, which is a transverse-ambipolar-diffusion driven balance (collisional ionization balanced by transverse diffusion). This occurs generally at low n_g. If $\Lambda_3 \ll 1$, then $\alpha_\infty = \alpha_{eq}$.

Now, using the information at the downstream boundary, equation 4.6 may be rewritten as

$$\frac{d\gamma}{d\alpha} = 1 + \frac{\Lambda_1 \alpha}{\gamma}[(\alpha - \alpha_\infty) + \Lambda_2(\alpha^2 - \alpha_\infty^2)] \tag{4.15}$$

The results above may be recast in order to emphasize that there are families of trajectories which are functions of a modified Damkohler coefficient. Rescaling both γ and α by α_∞ will mean that all of the trajectories will have the same endpoint. Defining the new variables, $a \equiv \alpha/\alpha_\infty$, $g \equiv \gamma/\alpha_\infty$, and the parameters $\tilde{\Lambda}_1 = \Lambda_1\alpha_\infty$, and $\tilde{\Lambda}_2 = \Lambda_2\alpha_\infty$, then equation 4.15 becomes

$$\frac{dg}{da} = 1 + \frac{\tilde{\Lambda}_1 a((a-1) + \tilde{\Lambda}_2(a^2-1))}{g} \tag{4.16}$$

Singularities occur when $g = 0$, and correspond physically to: $a = 0$ (which will actually occur outside the channel, before the physical inlet, as we will see) and $a = 1$ (which is the asymptotically approached uniform plasma boundary). Near to the $a = 0$, $g = 0$ singularity (which should not lie inside the actual channel), define $k_g = \frac{dg}{da}$, so that $g \approx k_g a$, and equation 4.16 becomes, for small a:

$$k_g = 1 + \frac{-\tilde{\Lambda}_1(1+\tilde{\Lambda}_2)}{k_g}$$

or, solving for k_g,

$$\left(\frac{dg}{da}\right)_o = k_g = \frac{1}{2} \pm \sqrt{\frac{1}{4} - \tilde{\Lambda}_1(1+\tilde{\Lambda}_2)} \tag{4.17}$$

If $\tilde{\Lambda}_1(1+\tilde{\Lambda}_2)$ is smaller than $\frac{1}{4}$, there will be two such real slopes, and the trajectories approach the $a = g = 0$ point along the smaller of them. In that case, the wall condition (rewriting equation 4.10 in nondimensional form), which is now

$$g = a\left(1 + \frac{v_B}{u}\right)$$

can be differentiated to become

$$\left(\frac{dg}{da}\right)_o = 1 + \frac{v_B}{u} \tag{4.18}$$

The condition that, starting from the $a = g = 0$ singularity, the two trajectories defined by the slopes from equations 4.17 and 4.18 match near the singularity is then only met at the origin itself. In this case, the ion density approaches zero exponentially on the upstream side, and an infinite ionization length is implied. (Note that $u \ll v_B$ in this case).

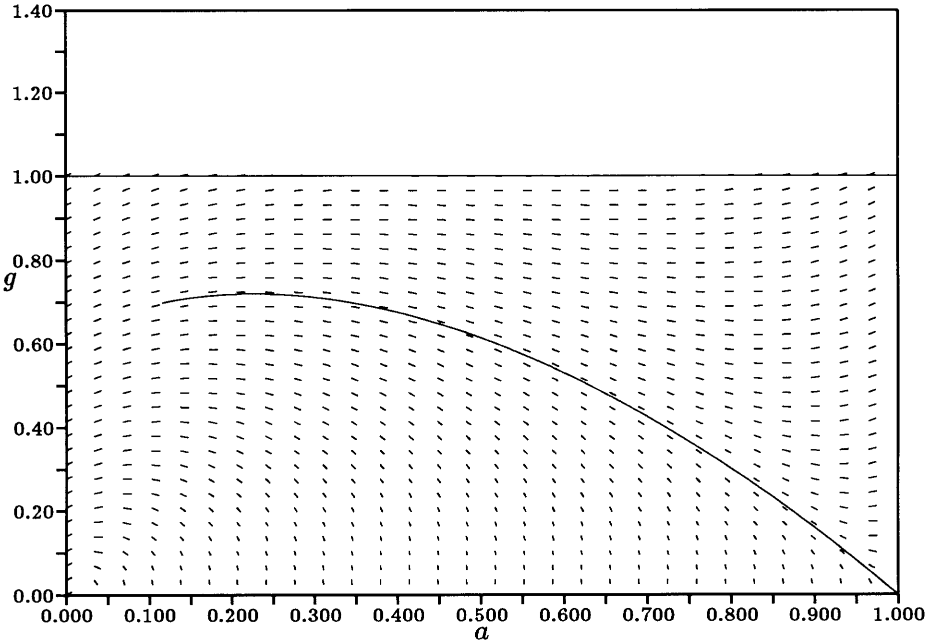

Figure 4.2: g vs a for $\tilde{\Lambda}_1 = 3.5$ $\tilde{\Lambda}_2 = 0.14286$, $v_B/u = 5$.

On the other hand, when $\tilde{\Lambda}_1(1+\tilde{\Lambda}_2) > \frac{1}{4}$, the singularity becomes a spiral point, and the trajectory arriving from the downstream singularity crosses the wall condition (eq. 4.18) at finite a and g, which corresponds to a finite ionization layer thickness (from $dx = \frac{C_a}{\Gamma} d\alpha$).

This is illustrated in the following figures, which show the calculated trajectory superimposed onto the g-a phase plane with isoclines shown (the isoclines are the slopes, from equation 4.16). In figure 4.2, $\tilde{\Lambda}_1(1+\tilde{\Lambda}_2) > \frac{1}{4}$, the $g = a = 0$ singularity is a spiraling singularity, and the wall condition is satisfied at finite g (the inlet location is where the trajectory ends moving towards low a). In figure 4.3, however, $\tilde{\Lambda}_1(1+\tilde{\Lambda}_2) < \frac{1}{4}$, the $g = a = 0$ singularity is approached directly, and the wall condition is only satisfied at $a = g = 0$.

The condition for successful ignition is then

$$\frac{1}{4} < \tilde{\Lambda}_1(1+\tilde{\Lambda}_2)$$

which is

$$\frac{1}{4} < \Lambda_1(\alpha_\infty + \Lambda_2 \alpha_\infty^2)$$

or, using equation 4.12,

$$\frac{1}{4} < \Lambda_1(1-\Lambda_3) \tag{4.19}$$

Now, using equations 4.7 and 4.9, the condition for "ignition in a finite distance" is that the speed be below a "blowoff value", defined as:

$$u < 2\sqrt{\frac{C_a S_{ac}}{1 + \frac{4C_a^2}{(Gh)^2}}} = u_{bo} \tag{4.20}$$

Physically, the blowoff speed is the fastest injection speed for which the back-diffusion can transport ions and electrons to the inlet wall, and meet the wall condition that the ions reach the wall at the Bohm velocity. When the flow speed is above the blowoff speed, ions and electrons may diffuse back from the uniform downstream plasma, but can not reach the inlet. In this case, no ions can actually make it to the wall so that the wall condition is met by a zero ion flux to the wall at zero ionization fraction. If the flow speed were $-v_B$, then there would be no need for the pre-sheath which accelerates the ions towards the wall, since all ions reach the wall at the Bohm velocity.

Equation 4.20 makes use of the assumption of a downstream ionization-diffusion balance only when $Gh \gg 2C_a$ is not satisfied. By the same token, it leaves the sensitive ionization rate function S_{ac} unspecified, and then indicates that the flow velocity in the ionization region (presumably before significant magnetic acceleration) should be below a temperature-dependent limit. This maximum speed is independent of the flow rate, G, only for $Gh \gg 2C_a$. The maximum speed as indicated by equation 4.20 is plotted in figure 4.4, for $\theta = 0.3333$ and varying G, with constant $h = \frac{.02}{\sqrt{12}} m$.

Note that the u_{bo} in equation 4.20 indicates that extinction results whenever the injected neutrals convect many diffusion lengths before they ionize. Since $n_g = G/u$, if the speed is picked to be some value below the maximum (extinction value), $u = \epsilon u_{bo}$, and

$$\epsilon = \frac{u}{u_{bo}}$$

where $0 < \epsilon < 1$, then the parameters (Λ_1, Λ_2, Λ_3) are as shown in table 4.2. (Note that the ignition condition, equation 4.19, is automatically satisfied both when $GH \gg 2C_a$ and in the diffusion driven case, when $GH \ll 2C_a$, so long as $\epsilon < 1$.)

The ionization fraction at ∞ calculated using equation 4.13 can now be considered a function of G, temperature, and ϵ, if h is fixed. Figure 4.5 is a plot of α_∞ vs T_e with $\epsilon = 0.5$ and $T_e = 2T_H$. The diffusion effects are strongest at lower G and higher temperatures. For $Gh \ll 2C_a$, diffusion effects are strong, and at temperatures high enough to make Λ_2 small,

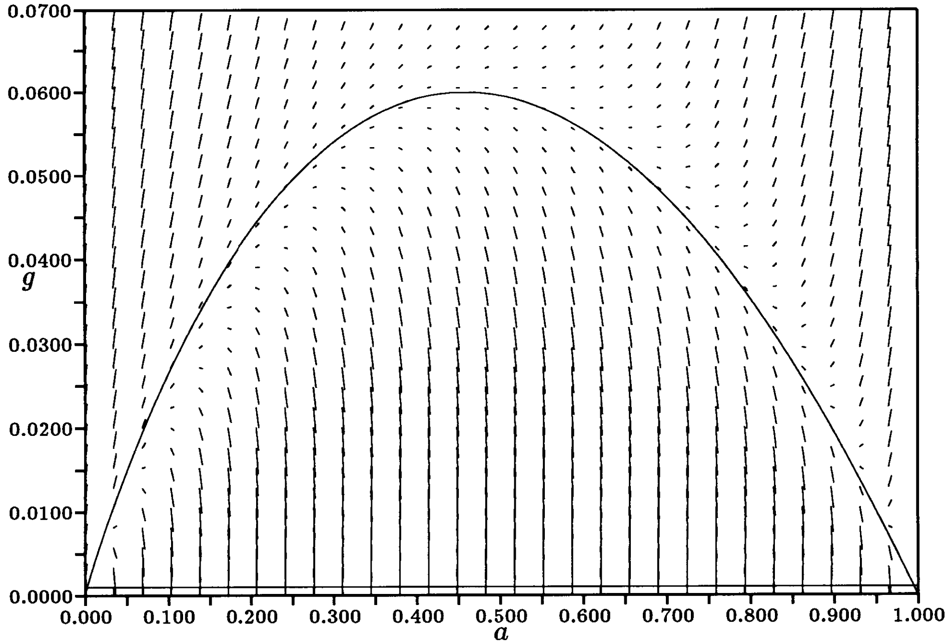

Figure 4.3: g vs a for $\tilde{\Lambda}_1 = 0.2$ $\tilde{\Lambda}_2 = 0.14286$, $v_B/u = 5$.

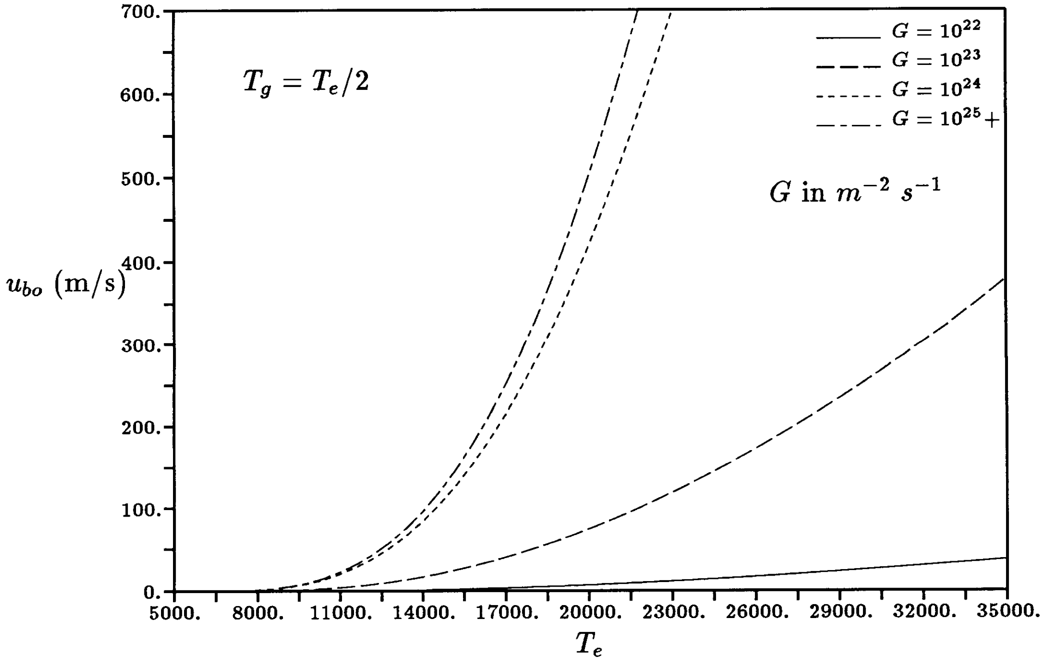

Figure 4.4: u_{bo} (m/s) vs T_e for argon gas, at various values of G. $(T_e = 2T_g)$ Speeds below each curve represent ignition, above is extinction. At high G, u_{bo} is no longer a function of G.

		$Gh \ll 2C_a$
Λ_1	$\frac{1+4(\frac{C_a}{Gh})^2}{4\epsilon^2}$	$\left(\frac{C_a}{\epsilon Gh}\right)^2$
Λ_2	$\frac{G\sqrt{1+4(\frac{C_a}{Gh})^2}}{2\epsilon S(1,T_e)\sqrt{C_a S_{ac}}}$	$\frac{\sqrt{C_a}}{\epsilon h S(1,T_e)\sqrt{S_{ac}}}$
Λ_3	$\frac{4C_a^2\epsilon^2}{(Gh)^2(1+4(\frac{C_a}{Gh})^2)}$	ϵ^2

Table 4.2: The parameters of the constant speed and temperature model with atomic injection, as functions of ϵ.

the ionization fraction at ∞ is $\alpha_\infty = 1 - \epsilon^2$, which is the case seen in figure 4.5, where α_∞ approaches $1 - \epsilon^2 = 0.75$ as $\frac{Gh}{2C_a} \to 0$. Note that a typical Gh for a plasma accelerator is $\approx 4.6 \times 10^{22} m^{-1} s^{-1}$ and $2C_a = 5.405 \times 10^{19}\sqrt{T_e} m^{-1} s^{-1}$ for $T_e = 2T_g$ in argon.

The ignition condition (equation 4.20) can be rewritten in two ways:

$$Gh < 2C_a\sqrt{\frac{\alpha_\infty}{1-\alpha_\infty}}$$

$$u < 2\sqrt{\alpha_\infty C_a S_{ac}} = u_{bo} \tag{4.21}$$

Where u_{bo} is again the "blowoff" speed. As seen in figure 4.4, for small G, u_{bo} is reduced, as indicated here (since $\alpha_\infty < 1$, and, in fact approaches $1 - \epsilon^2$.) If the diffusion-driven limit (low Gh) is approached, then using the definitions of G and h, and $\dot{m} = m_i G A$ is the mass flow rate,

$$\frac{\dot{m}}{w} < m_i C_a\sqrt{48\frac{\alpha_\infty}{1-\alpha_\infty}} \tag{4.22}$$

where w is the depth (along $\vec{B}$). For typical values of $\frac{\dot{m}}{w}$ and of m_i and $C_a = D_a n_g$, satisfaction of equation 4.22 requires α_∞ to be fairly close to unity. Heimerdinger [27] noted in his experiments that, with a wide inlet, and low field, there was no ignition. This corresponds to low α_∞. Reducing H, which increased the electric field, E, solved the problem.

In order to be able to tie a and g to the axial length variable, ξ, the nondimensional form of equation 4.3,

$$\frac{d\alpha}{d\xi} = \gamma$$

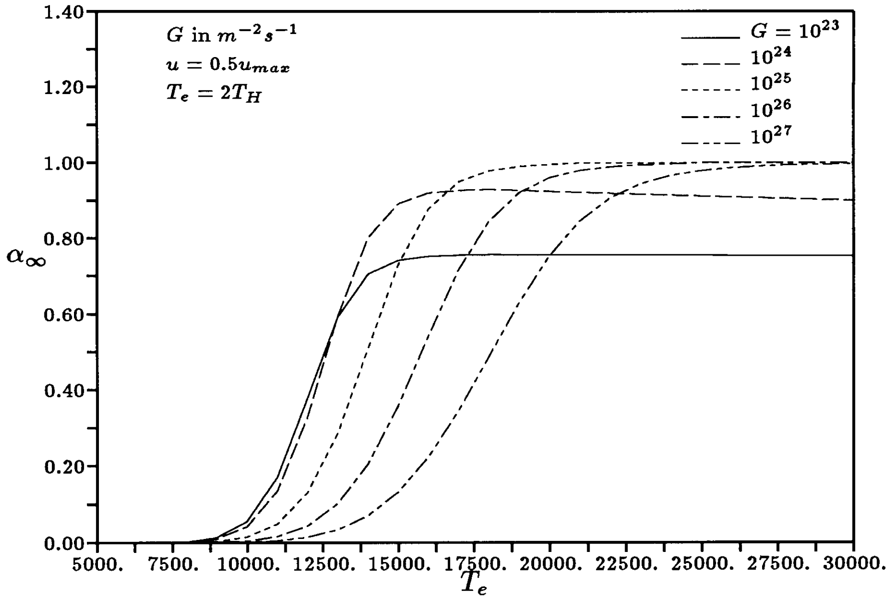

Figure 4.5: α_∞ vs T_e for various values of G. ($\epsilon = 0.5$, $T_e = 2T_g$) When $Gh \ll 2C_a$, then $\alpha_\infty < \alpha_{eq}$ and α_∞ approaches the value $(1 - \epsilon^2)$. ($\epsilon = 0.5$ in this case.) The high-G curves are basically the Saha equilibrium results for different total nuclei number density n_g.

is divided through by α_∞ and inverted to obtain the equation for $\xi(a)$:

$$\frac{d\xi}{da} = \frac{1}{g} \tag{4.23}$$

This differential equation is integrated, with $\xi_o = 0$ along with equation 4.16. (recall that $\xi = x/l_D$)

Equation 4.16 is solved for $g(a)$, subject to the boundary conditions that the wall condition (equation 4.11) be met, and that the second $g = 0$ singularity be approached smoothly: $g = 0$ at $a = 1$. The COLSYS relaxation package [3] is used which solves for the $g(a)$ trajectory, $\xi(a)$, and the unknown a_o simultaneously as a function of the parameters. The details of the approach used for this problem are outlined in section A.2.2.

Figure 4.6 is a plot of calculated g vs a trajectories for various values of $\tilde{\Lambda}_1$, and shows two things. First, increasing $\tilde{\Lambda}_1$ increases the value of a at the inlet: $a_o = \alpha_o/\alpha_\infty$. Second, increasing $\tilde{\Lambda}_1$ results in larger g_o, and larger g in general, which, by equation 4.23, indicates lesser ξ. These two observations are coupled by the inlet wall boundary condition. Shown in figure 4.7 are the corresponding a vs $\xi = x/l_D$ trajectories for the same $\tilde{\Lambda}_1$. The decreasing width of the ionizing front with increasing $\tilde{\Lambda}_1$ can be seen in this graph, along with the

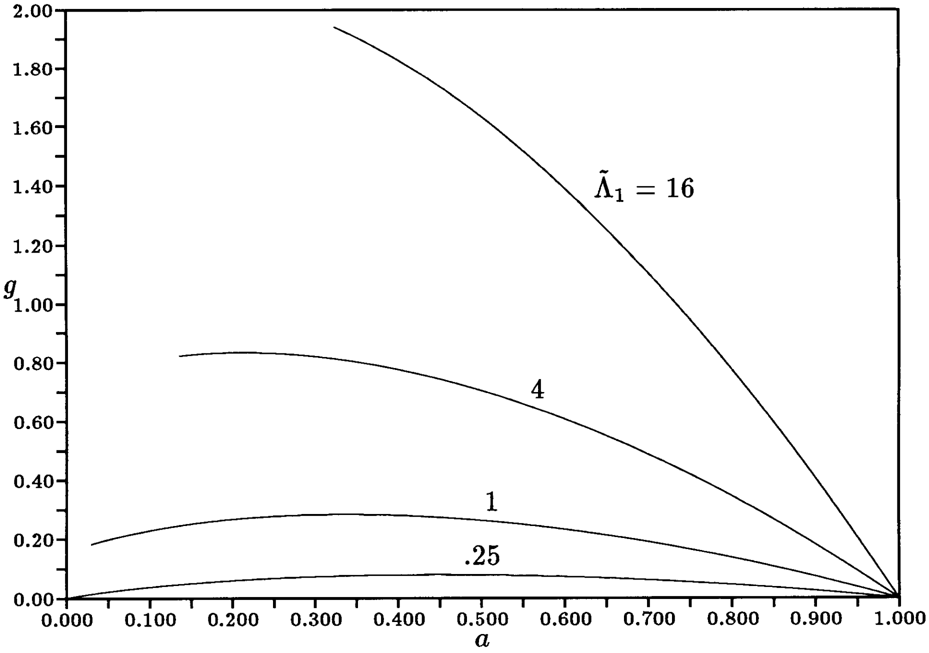

Figure 4.6: g vs a for $\tilde{\Lambda}_2 = 0.2$, $v_B/u = 5$.

ionization delay or lag which occurs when $\tilde{\Lambda}_1$ is small.

Some typical results of this model (using the original nondimensional variables) are presented graphically for a realistic G ($G = n_g u = 7.5 \times 10^{24} m^{-2} s^{-1}$.) Figure 4.8 shows a typical ignition trajectory for $T_e = 20000K$, $\epsilon = 0.5$. Plotted is the $\gamma(\alpha)$ trajectory on a background of local isoclines ($\frac{d\gamma}{d\alpha}$). The trajectory ends at low α when the wall condition is met. Note that the isoclines show that trajectories even slightly off of the actual one will diverge moving in the direction of increasing ionization fraction, while trajectories moving in the direction of decreasing ionization fraction tend to converge onto the actual one.

Figure 4.9 shows three α vs x trajectories for the same conditions and varying constant average speed. The speeds chosen correspond to the typical range found numerically by Niewood [51] and in various experiments at Princeton's Electric Propulsion Laboratory [22] and recently reported by [59]. The range of inlet speeds is roughly 100 to 500 m/s. Note that lower speeds result in shorter ionizing regions, and higher values of α_o.

There must be an axial electric field, to counter the tendency of electrons to move upstream under their own pressure gradient. The field can be calculated through the use of the electron momentum equation (Ohm's Law), which is, for zero axial current: [14]

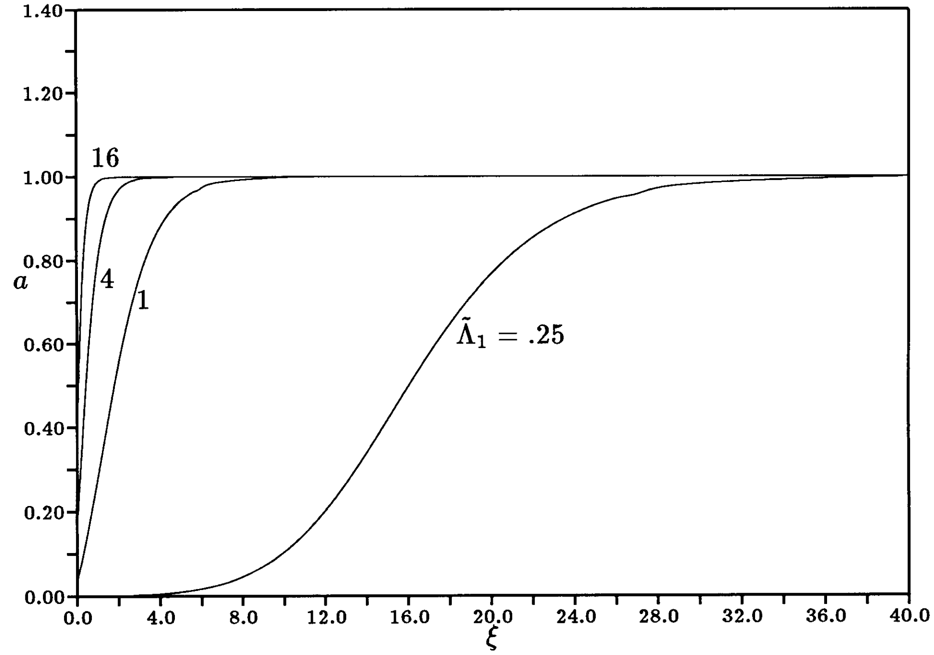

Figure 4.7: a vs ξ for $\tilde{\Lambda}_2 = 0.2$, $v_B/u = 5$.

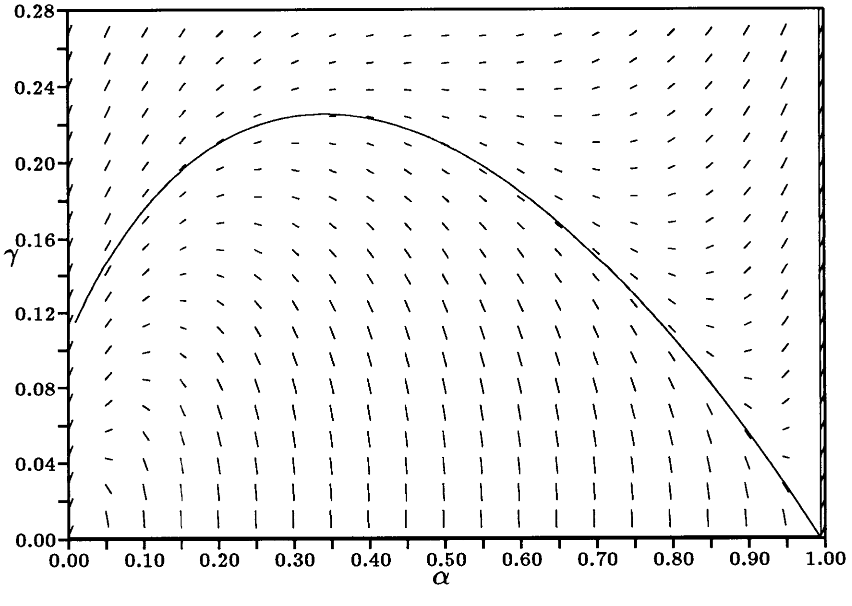

Figure 4.8: γ vs α phase-plane diagram for $T_e = 20000K$, $\epsilon = 0.5$, $T_e = 2T_H$, $G = 7.5 \times 10^{24} m^{-2} s^{-1}$. $\alpha_\infty = 0.9948$, $\alpha_o = 0.01050$, $u_{bo} = 500 m/s$.

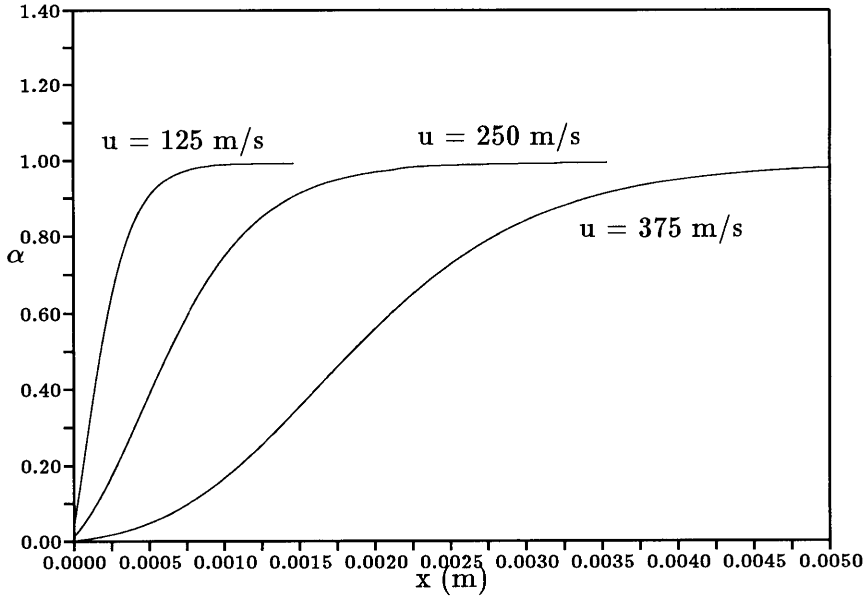

Figure 4.9: α vs x plots for $T_e = 20000K$, $\epsilon = 0.25, 0.5, 0.75$, $T_e = 2T_H$, $G = 7.5 \times 10^{24} m^{-2} s^{-1}$.

$$en_eE_x = -\frac{dp_e}{dx}$$

The electron pressure is $p_e = n_e k_B T_e$, so that, for constant electron temperature,

$$E_x = -\frac{k_B T_e}{e}\frac{d\ln n_e}{dx}$$

For a constant speed, constant temperature case [49], and using $\phi = -\int E dx$, the potential difference between the plasma at ∞ and the backplate wall is

$$\phi = \frac{k_B T_e}{e}\ln\left(\frac{\alpha_\infty}{\alpha_o}\right)$$

which indicates that the wall is at a negative potential, as required by the boundary condition that the wall be ion-attracting. This is the potential drop due to the ambipolar diffusion which is present even in the absence of current flow [49].

Figure 4.10 shows the variation of this potential difference with both temperature and $\epsilon = u/u_{bo}$. These results are similar to those found by Burton and Tiliakos [14], who noted that the axial potential difference was roughly the ionization potential for argon (15.8 V). At lower ϵ (lower speed), the potential is seen to be substantially less, though

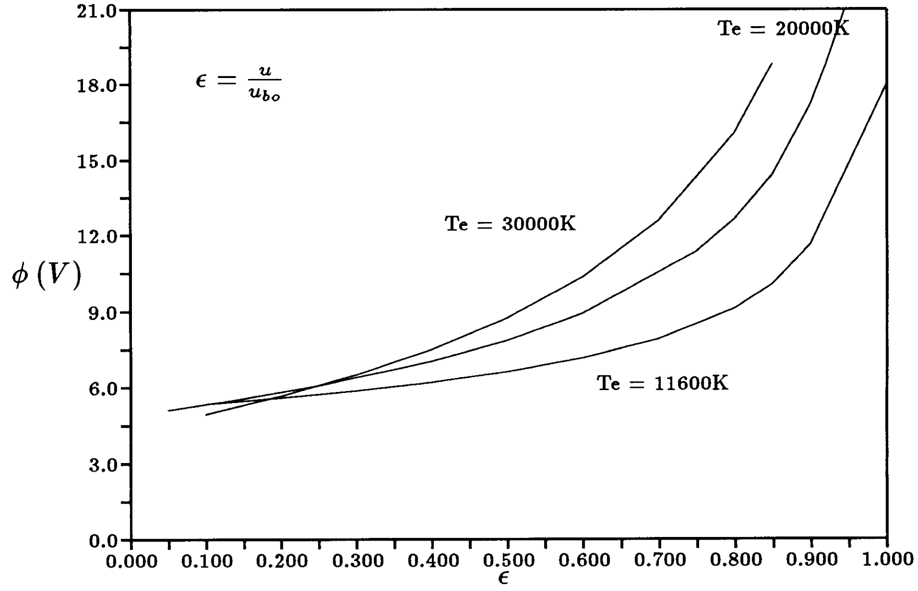

Figure 4.10: ϕ vs $\epsilon = \frac{u}{u_{bo}}$ for $T_e = 11600K$, $T_e = 20000K$, and $T_e = 30000K$, $G = 7.5 \times 10^{24} m^{-2} s^{-1}$.

always greater than the gap between the first excited state and the continuum, which is just over 4 V for the argon atom. This may be due to the fact that, as shown in Chapter 3, at higher temperatures, much of the net ionization rate is due to the transition between the ground state, the first excited level and the continuum; i.e., a three level model is roughly appropriate at these temperatures.

These results satisfy the goal of explaining mm-scale ionizing regions in channels, but are subject to the very stiff assumption of constant speed. The next section will investigate the effect of temperature variation effects in the ionizing region, and then the influence of self-field MPDT acceleration will be analyzed.

4.2 Atomic Injection with Varying T_e

In this section T_e is allowed to vary (finite thermal conductivity) to investigate the effects on the ignition criterion. The electron energy equation, including axial heat conduction, Ohmic heating, and energy loss due to the endothermic ionization process, and neglecting both pressure work and transverse heat conduction, is

$$\frac{3}{2}k_B\frac{dn_g u\alpha T_e}{dx} = \frac{d}{dx}\left(K_e\frac{dT_e}{dx}\right) + \frac{j^2}{\sigma} - E_{ac}\dot{n}_e \tag{4.24}$$

where T_e is the electron temperature, and E and j are the electric field and current density, respectively. This energy equation is modified by the assumption that $j \approx \sigma E$, and defining the heat flux as

$$q \equiv K_e\frac{dT_e}{dx} \tag{4.25}$$

so that the resulting energy equation is

$$\frac{3}{2}Gk_B\frac{d\alpha T_e}{dx} = \frac{dq}{dx} + \sigma E^2 - E_{ac}\dot{n}_e$$

or

$$\frac{dq}{dx} = \frac{3}{2}Gk_B\frac{d\alpha T_e}{dx} - \sigma E^2 + E_{ac}\dot{n}_e \tag{4.26}$$

which has a form very similar to the ion continuity equation (less the convective term), with a source and a sink which balance at infinity. Thus, the solution for q may be expected to be similar to that found for the ion slip flux, Γ.

The recombination rate term will be dropped from now on in the analysis since its influence on the ignition criteria was found to be weak, coming only through the determination of α_∞. The downstream boundary conditions for this model will be simplified in this case. The new nondimensional forms of equations 4.3, 4.6 (modified for non-constant temperature), 4.25, and 4.26 are then, respectively:

$$\frac{d\alpha}{d\xi} = \gamma \tag{4.27}$$

$$\frac{d\gamma}{d\xi} = \gamma - \alpha\Lambda_1[\bar{S}(1-\alpha) - \Lambda_3] \tag{4.28}$$

$$\frac{d\tau}{d\xi} = Q \tag{4.29}$$

$$\frac{dQ}{d\xi} = Le\left(\alpha Q + \tau\gamma - \bar{\sigma}\Pi + \Theta_{ac}\alpha\Lambda_1[\bar{S}(1-\alpha)]\right) \tag{4.30}$$

where the length is nondimensionalized as $\xi = x/l_D$, where $l_D = C_a/G$ is the back-diffusion length, the nondimensional slip is $\gamma = \Gamma/G$, and the electrical conductivity is $\bar{\sigma} = \sigma/\sigma_{ref}$. The nondimensional parameters are the Damkohler coefficient for ionization $\Lambda_1 = l_D/l_{ac}$, Λ_2, and Λ_3 as in the constant T_e case, evaluated at the reference temperature:

$$\Lambda_1 = \frac{C_a S_{ac}}{u^2}$$

$$\Lambda_2 = n_g \left(\frac{n_a}{n_e^2}\right)^* \qquad \Lambda_3 = \frac{C_a}{S_{ac}(hn_g)^2}$$

plus the nondimensional forms for the ohmic heating and ionization potential energy terms:

$$\Pi = \frac{C_a \sigma_{ref} E^2}{\frac{3}{2} k_B T_{ref} G^2} \qquad \Theta_{ac} = \frac{E_{ac}}{\frac{3}{2} k_B T_{ref}}$$

The nondimensional ionization coefficient is $\bar{S}(\tau) = S_{ac}/S_{ac}^{ref}$, and S_{ac}^{ref} is evaluated at T_{ref}, the electron temperature at $\xi = \infty$:

$$\bar{S} = \frac{S_{ac}}{S_{ac}^{ref}} = \frac{S_{ca}\ S(s,1,T_e)}{S_{ca}^{ref}\ S(s,1,T_{ref})}$$

All of the temperature-dependent quantities in these parameters are evaluated at $T_e = T_{ref} = T_{e\infty}$.

The Lewis number is the ratio of the diffusion length scale to the thermal conductivity length scale, and is discussed in section 2.3.2. It is

$$Le = \frac{3}{2}\frac{k_B n_g D_a}{K_e} = \frac{l_D}{l_{cond}}$$

and is typically $O(10^{-2})$ for the conditions of interest here. When $Le \to 0$, then the electron temperature varies on a scale much longer than the ambipolar diffusion scale, although, as the results show, there may be an axial boundary layer close to the inlet. For $Le = O(1)$, the temperature varies on a scale similar to l_D, and for large Le, the temperature length scale is the critical small scale.

This is another asymptotic problem, where $\xi \to \infty$ at the downstream boundary. Choosing α as a more convenient independent variable again, the equations for constant speed, finite thermal conductivity, and atomic injection (equations 4.28, 4.29, and 4.30, respectively), all divided by equation 4.27 are the new equations of motion:

$$\frac{d\gamma}{d\alpha} = 1 - \frac{\Lambda_1 \alpha[\bar{S}(1-\alpha) - \Lambda_3]}{\gamma} \tag{4.31}$$

$$\frac{d\tau}{d\alpha} = \frac{Q}{\gamma} \tag{4.32}$$

$$\frac{dQ}{d\alpha} = Le\left(\tau + \frac{-\bar{\sigma}\Pi + \Theta_{ac}\alpha\Lambda_1\bar{S}(1-\alpha) + \alpha Q}{\gamma}\right) \tag{4.33}$$

The boundary conditions are again the wall condition, repeated from equation 4.11, which serves to set the ionization fraction at the inlet:

$$\gamma = \alpha\left(1 + \frac{v_B}{u}\right)$$

In addition, all singularities must be resolvable if they are physically reasonable, so that all of the derivatives most be smooth at the asymptotic limit: $\gamma_\infty \to 0$. One such condition will be the same as equation 4.12, except without the collisional recombination term,

$$1 - \alpha_\infty - \Lambda_3 = 0 \tag{4.34}$$

Note that $\bar{S} = \bar{\sigma} \equiv 1$ at $\xi = \infty$, since that is where the reference values are taken. In addition, $Q_\infty = 0$, and the numerator of the fraction in the electron energy equation must go to zero at ∞:

$$\Pi - \Theta_{ac}\alpha_\infty\Lambda_1[1 - \alpha_\infty - \alpha_\infty^2\Lambda_2] = 0 \tag{4.35}$$

The combination of equations 4.34 and 4.35 is usually used to solve for α_∞ and $T_{e_\infty} = T_{ref}$ as a function of (n_g, h, T_g, E). In this case, the specified values are (G, T_{ref}, u, h) (u is arbitrary since no momentum balance is used), so that $(\alpha_\infty, E) = f(n_g(u, G), h, T_g, T_{ref})$, and

$$\Pi = \Theta_{ac}\Lambda_1\Lambda_3\alpha_\infty \qquad E = \sqrt{\frac{E_{ac}C_a\alpha_\infty}{\sigma_{ref}h^2}}$$

Finally, it is assumed that the electrons do not heat the inlet wall, so that the initial electron heat flux is zero: $Q_o = 0$. This condition fixes the inlet electron temperature given all of the other parameters.

Local analysis near $\alpha = \gamma = 0$ results in a similar ignition criterion as in the constant T_e case, except it is evaluated at the inlet temperature:

$$u < 2\sqrt{\frac{C_a S_{ac}(0)}{1 + \frac{4C_a^2}{(Gh)^2}}} = u_{bo} \tag{4.36}$$

This problem was solved by space-marching from $\alpha = \alpha_\infty$ to the wall and iterating to satisfy the inlet conditions. A variable-step Runge-Kutta routine was used. Local analysis near the asymptotic boundary condition was used to determine the values of the derivatives there. Defining $\Delta\alpha = \alpha - \alpha_\infty$, then, near to the asymptotic boundary, the variables may be expressed as

$$\gamma \approx m_\gamma \Delta\alpha \qquad \tau \approx 1 + m_\tau \Delta\alpha \qquad Q \approx m_Q \Delta\alpha$$

where m_γ, m_τ, and m_Q are the local slopes near $\alpha \approx \alpha_\infty$ for γ, τ, and Q, respectively. Substituting these into equations 4.31, 4.32, and 4.33 yields

$$\left(\frac{d\gamma}{d\alpha}\right)_\infty \equiv m_\gamma = 1 - \frac{\Lambda_1 \alpha_\infty [-1 + \bar{S}_\tau m_\tau (1 - \alpha_\infty)]}{m_\gamma}$$

$$\left(\frac{d\tau}{d\alpha}\right)_\infty \equiv m_\tau = \frac{m_Q}{m_\gamma}$$

$$\left(\frac{dQ}{d\alpha}\right)_\infty \equiv m_Q = Le\left(-1 + \frac{\bar{\sigma}_\tau m_\tau \Pi - \Theta_{ac}\Lambda_1 \alpha_\infty [-1 + \bar{S}_\tau m_\tau] - \alpha_\infty m_Q}{m_\gamma}\right)$$

where $\bar{S}_\tau = \frac{d\bar{S}}{d\tau}$ and $\bar{\sigma}_\tau = \frac{d\bar{\sigma}}{d\tau}$ evaluated at $\alpha = \alpha_\infty$. These three equations are solved simultaneously for the slopes near $\alpha \approx \alpha_\infty$, and an initial step is taken from α_∞ to $\alpha_\infty + \Delta\alpha$ using a small negative $\Delta\alpha$. A Runge-Kutta space marching routine is then used to integrate from $\alpha_\infty + \Delta\alpha$ in the negative α direction (towards the inlet wall).

Table 4.3 outlines the most significant parameters of three cases presented here from the varying temperature model. Note that for these cases, a lower flow rate of $G = 7.5 \times 10^{23}\ m^{-2} s_{-1}$ was used since the combination of downstream boundary conditions tended

Case	T_{eo} (K)	$T_{e\infty}$ (K)	u (m/s)	Λ_1	Le	Π	E (V/m)	Θ_{ac}
T1	23482	20000	409.30	0.375	.056	0.857	217	9.14
T2	29060	25000	835.42	0.472	.036	0.862	195	7.32
T3	42499	40000	2499.0	0.970	.018	1.067	172	4.57

Table 4.3: Cases for the varying electron temperature runs displayed here.

to drive the number density down, and thus would resulted in extremely high speeds, for fixed $G = un_g$.

Figure 4.11 shows the calculated profiles for the trajectory corresponding to case T1 shown in table 4.3. The relative size of the the terms in the nondimensional electron energy equation (in the form given by equation 4.30) is shown in figure 4.12. The heating term is $(Le\bar{\sigma}\Pi)$ and the ionization loss term is $-(Le\ \Theta_{ac}\Lambda_1\bar{S}\alpha(1-\alpha))$. As can be seen, the combination of low T_e and n_e at the inlet keeps the ionizational loss term low, so that the ohmic heating term dominates until the ionization process begins. Combined with the boundary condition that there is no electron heat conduction into the wall, this raises the temperature at the inlet, with the only heat conduction in the downstream direction.

Figures 4.13 and 4.14 are the corresponding plots for case T2. The Ohmic heating term still dominates near to the inlet, but not as much as in case T1 since both the inlet ionization fraction and temperature is higher. Keep in mind that the nondimensional length scale is $\xi = x/l_D$, where $l_D = \frac{C_a}{G}$ is the axial diffusion scale, which decreases with increasing temperature. A higher temperature case - T3 - is depicted in figures 4.15 and 4.16. In this case, the ionization loss term quickly rises to match the Ohmic heating term, so very little heating occurs.

Note that these plots show that, as the electron temperature increases, the ion slip term, $\gamma = -n_e V_i/G$, increases in magnitude (and therefore the ionization length scale is shorter) and the heat flux term, $Q = q/q_{ref}$ decreases in magnitude (so that there is less temperature variation). As found in the constant speed and temperature model, increasing Λ also tends to increase the inlet ionization fraction.

These results show that, if the temperature variation has any effect on the initiation of ionization, it is a positive one. Since the blowoff speed is a function of T_e, and the temperature rises near the inlet wall, ignition is more likely. Therefore, at the level of detail

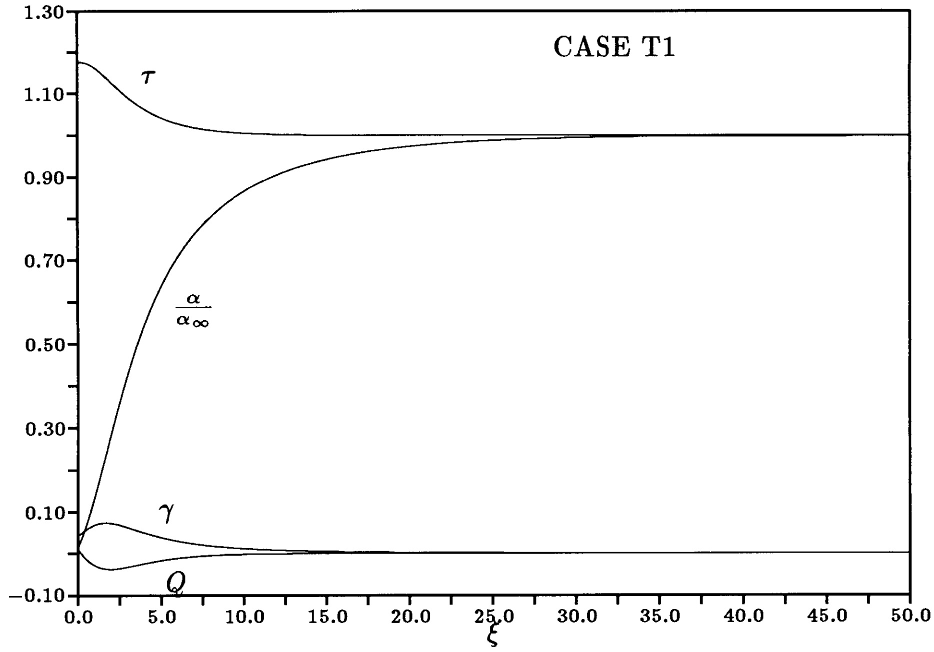

Figure 4.11: Constant speed ignition with atomic injection and varying temperature, case T1: α/α_∞, τ, γ, and Q.

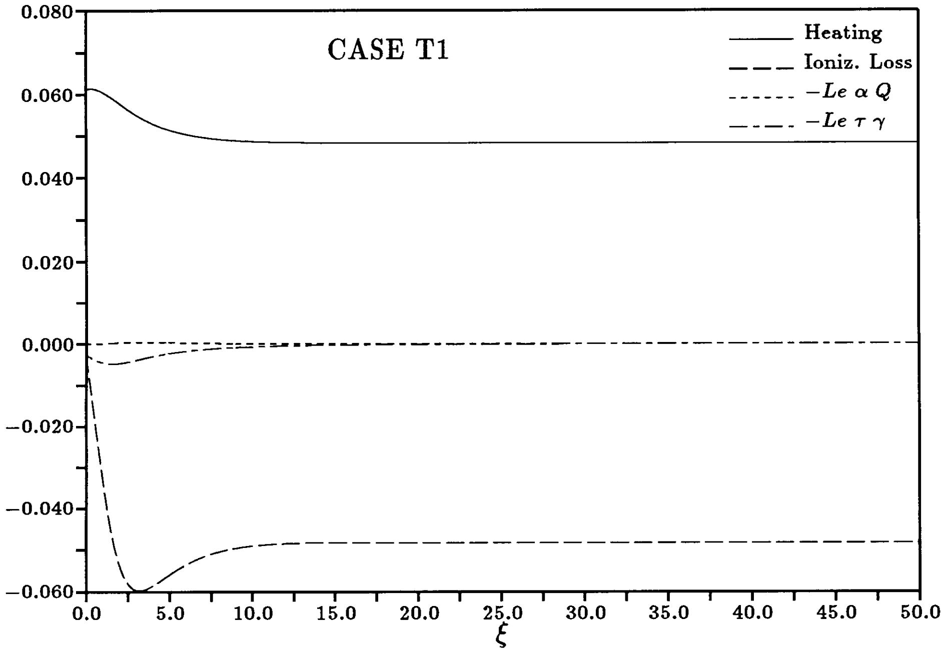

Figure 4.12: Constant speed ignition with atomic injection and varying temperature, case T1. Comparison of the terms in the electron energy equation.

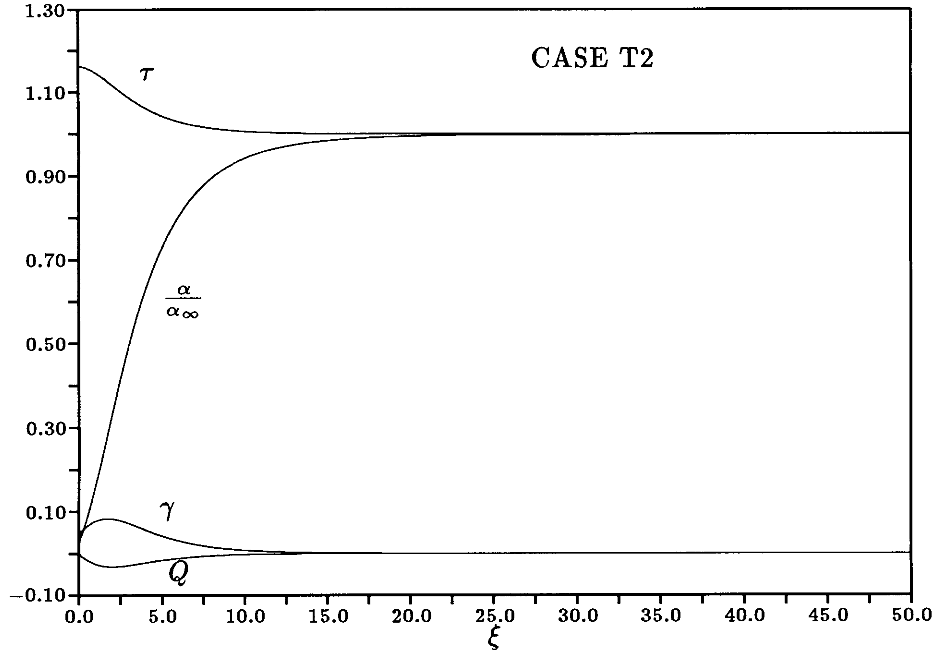

Figure 4.13: Constant speed ignition with atomic injection and varying temperature, case T2: α/α_∞, τ, γ, and Q.

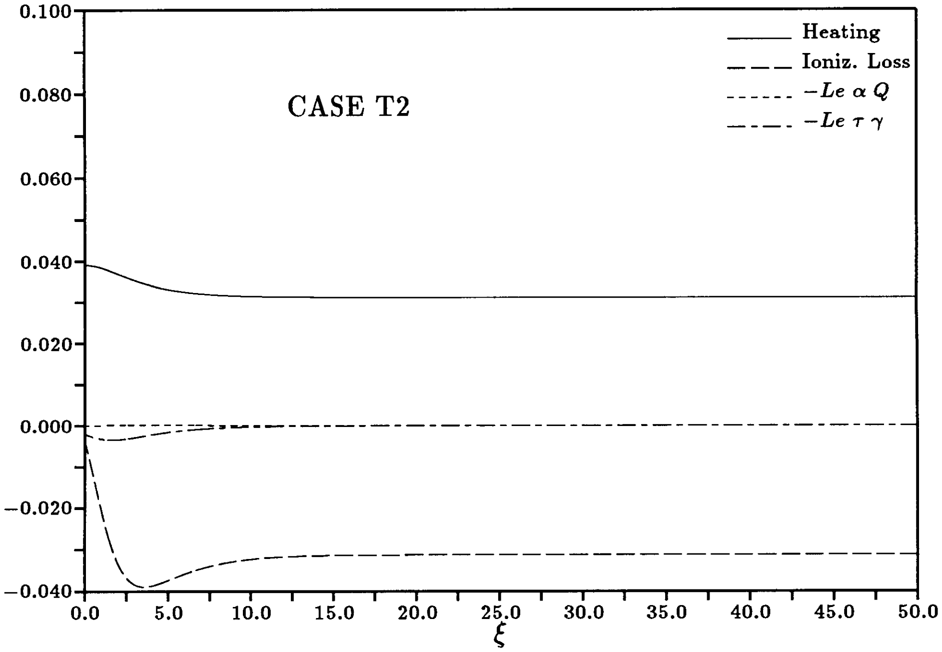

Figure 4.14: Constant speed ignition with atomic injection and varying temperature, case T1. Comparison of the terms in the electron energy equation.

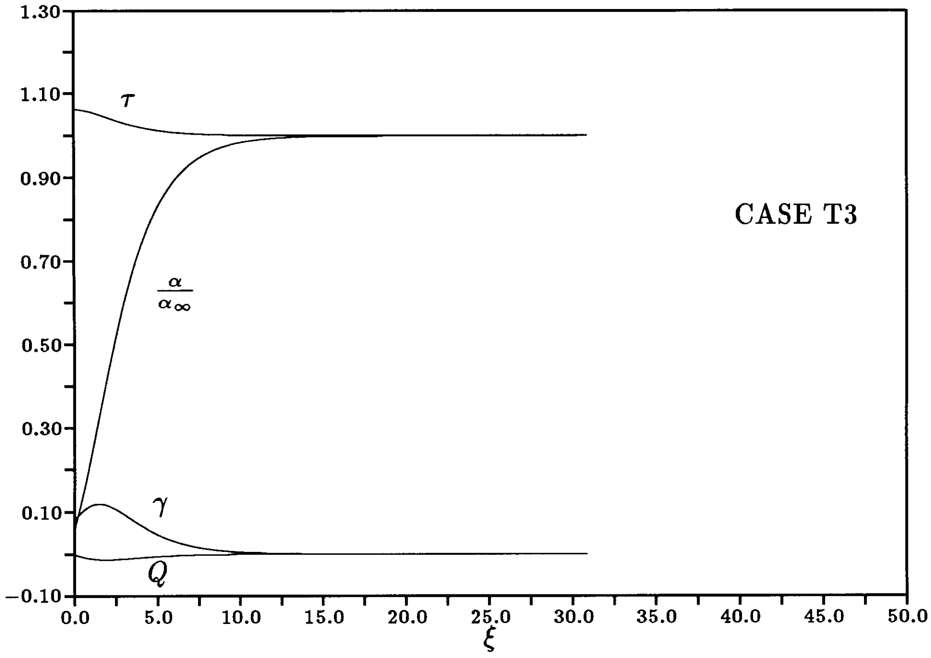

Figure 4.15: Constant speed ignition with atomic injection and varying temperature, case T3: α/α_∞, τ, γ, and Q.

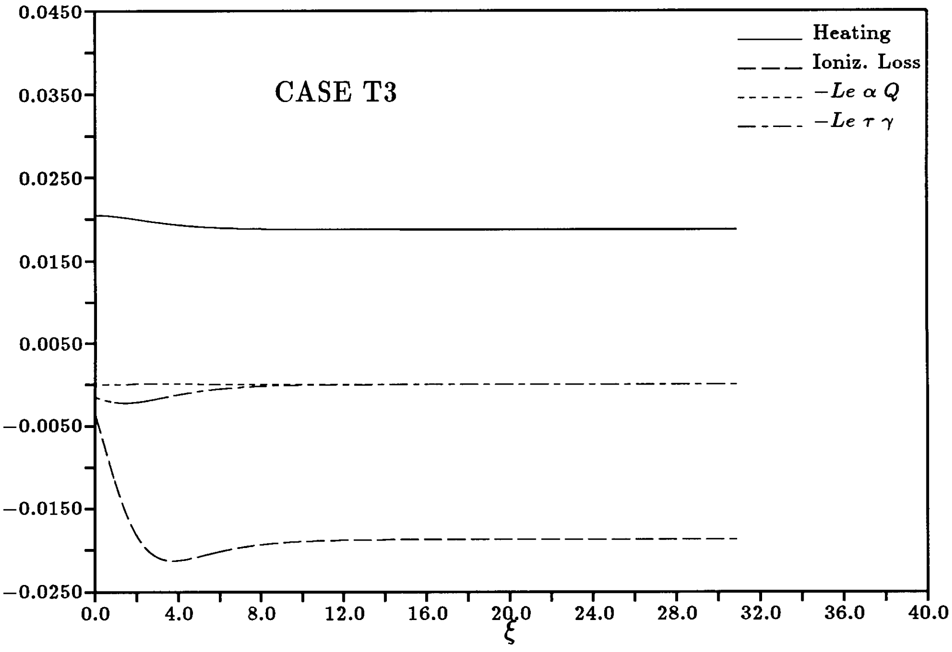

Figure 4.16: Constant speed ignition with atomic injection and varying temperature, case T1. Comparison of the terms in the electron energy equation.

of this analysis, temperature variation is a positive effect. However, it should be kept in mind that the energy balance at infinity assumed here, while reasonable, is not tied to any thruster parameters except the electrode gap (recall that the electric field is a derived quantity), so that other effects which may set lower temperatures are not included. Some discussion of such effects can be found at the end of the section on ignition in accelerating flows.

4.3 Ignition in Accelerating Flows: Non-local Energy Balance

We now drop the assumption of constant speed, but maintain the constant electron temperature assumption, following from the results of the previous section. This allows for analysis of the interaction between the behavior of the magnetic field and the ionization process. The problem is treated here as two inner-outer problems. First, there is a an inner region with both acceleration and magnetic diffusion which reaches from the wall out to a "back-emf dominated" boundary condition, and then an ideal outer region which is solved analytically into the channel and to the throat.

The ionization zone is found to be entirely embedded in the magnetic diffusion (inner) layer, and consists of an inner ambipolar diffusion layer, near the wall, and an intermediate layer, where ambipolar diffusion plays no significant role, although magnetic diffusion still plays a role. The first subsection following describes the model, and the second presents results.

A schematic of the regions to be considered is shown in figure 4.17. The labels refer to the following regions: w is the wall, from w to 1 is the inner ionization layer, from 1 to 2 is the inner magnetic region (here and for the rest of the channel an outer ionization layer), from 2 to 3 is the outer magnetic layer, and from 3 to 4 (the exit) is the exit magnetic layer. The electron temperature is taken as a constant ($K_e \to \infty$). Its value is an important parameter for ignition and will be determined in a consistent manner by an overall energy balance in the inlet region.

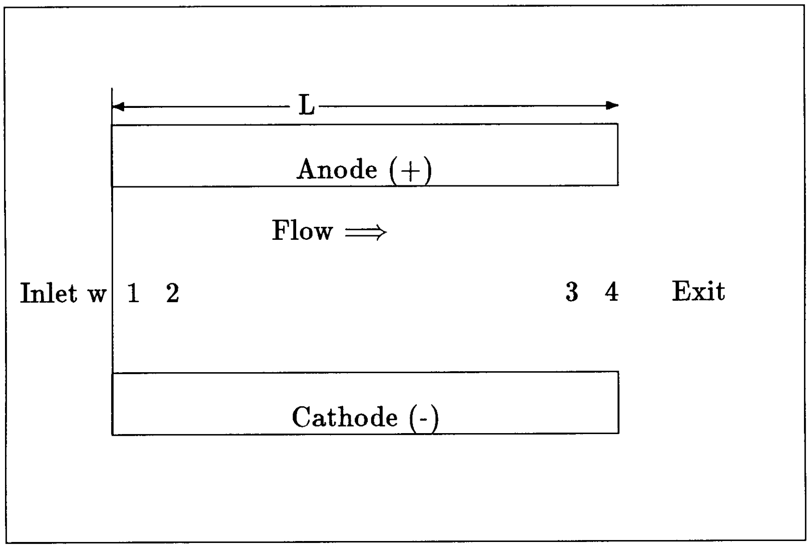

Figure 4.17: Regions in an MPD Channel

4.3.1 Formulation

We start with $G = \frac{\dot{m}}{m_i A_t}$ = constant in the ionization zone. The integrated total momentum equation, including pressure and magnetic (Lorenz) forces and neglecting friction, is

$$m_i n_g u^2 + p + \frac{B_z^2}{2\mu_o} = F \tag{4.37}$$

where p is the pressure, B is the magnetic field, m_i is the ion mass, and F is a constant of the flow. The magnetic field is governed by the following equation

$$\frac{dB}{dx} = -\mu_o j = -\mu_o \sigma [E - uB] \tag{4.38}$$

The differential form of the momentum equation (4.37) will also be used:

$$m_i G \frac{du}{dx} = \frac{d}{dx}\left[p + \frac{B^2}{2\mu_o}\right] \tag{4.39}$$

where the pressure for a two temperature, electrically neutral plasma is

$$p = m_i n_g v_B^2 (\alpha + (1 - \alpha)\theta) \tag{4.40}$$

Here, because of the acceleration, the alternative version for the ion slip flux is used, so that, from equation 2.22, we can define the flux, $\Gamma = -n_e V_i$, from

$$\frac{d\alpha}{dx} = \frac{\Gamma}{C_a \theta} + (1-\alpha)(\frac{u^2}{\theta v_B^2} - 1)\frac{1}{u}\frac{du}{dx} \tag{4.41}$$

This equation, along with the following three, constitute the equations of motion for the quasi-one-dimensional isothermal flow problem. Starting with equation 4.39, and using equations 4.40, 4.41, the momentum equation becomes [63]

$$\frac{du}{dx} = \frac{-\frac{v_B^2(1-\theta)\Gamma}{C_a u} + \frac{\theta B}{m_i G}\sigma(E - uB)}{1 - \alpha(1-\theta) - \frac{\theta v_B^2}{u^2}} \tag{4.42}$$

Equation 4.2 may be rewritten as:

$$\frac{d\Gamma}{dx} = G\frac{d\alpha}{dx} + \frac{C_a \alpha}{h^2} - S_{ac} n_g^2 \alpha(1-\alpha) \tag{4.43}$$

and the final equation is the magnetic field equation, equation 4.38.

Nondimensionalizing these equations will allow us to analyze them parametrically. Defining reference values $u_{ref} = \frac{B_o^2}{2\mu_o m_i G}$, and $l_{ref} = \Lambda_m = \frac{1}{\mu_o \sigma u_{ref}}$, then the new variables are $\bar{u} = \frac{u}{u_{ref}}$, $\gamma = \frac{\Gamma}{G}$, $b = \frac{B}{B_o}$, $\bar{E} = E/(u_{ref} B_o)$ and $\xi = \frac{x}{\Lambda_m}$. The resulting nondimensional equations of motion are:

$$\frac{d\bar{u}}{d\xi} = \frac{-\frac{\beta(1-\theta)\gamma}{\epsilon_D \bar{u}} + \frac{2\theta b}{f}}{1 - \alpha(1-\theta) - \frac{\theta\beta}{\bar{u}^2}} \tag{4.44}$$

$$\frac{d\alpha}{d\xi} = \frac{\gamma}{\epsilon_D \theta} + (1-\alpha)(\frac{\bar{u}^2}{\theta\beta} - 1)\frac{1}{\bar{u}}\frac{d\bar{u}}{d\xi} \tag{4.45}$$

$$\frac{d\gamma}{d\xi} = \frac{d\alpha}{d\xi} + \alpha\left(\epsilon_w - \frac{\lambda(1-\alpha)}{\bar{u}^2}\right) \tag{4.46}$$

$$\frac{db}{d\xi} = -\frac{\bar{E} - \bar{u}b}{1 + (\frac{1}{\alpha} - 1)q} \tag{4.47}$$

where for convenience we define

$$f = \frac{1 + (\frac{1}{\alpha} - 1)q}{\bar{E} - \bar{u}b} = -\left(\frac{db}{d\xi}\right)^{-1}$$

In addition to the parameters defined previously,

$$\epsilon_D = \frac{(C_a)\mu_o \sigma_{ref} u_{ref}}{G} \approx \frac{(l_d)_{\|}}{\Lambda_m}$$

$$\lambda = \frac{S_{ac} G}{u_{ref}^3 \mu_o \sigma_{ref}} \approx \frac{\Lambda_m}{L_{ac}}$$

$$\epsilon_w = \frac{C_a \Lambda_m}{G h^2}$$

$$\beta = \frac{v_B^2}{u_{ref}^2}$$

The first far downstream ($\xi \to \infty$) boundary condition will be that $\bar{E} = \bar{u}b$, which implies an infinite length and hence an infinite magnetic Reynolds number. This motivates us to choose the magnetic field itself as the independent variable. Dividing the three other equations of motion (4.44, 4.45, 4.46) by equation 4.47, we arrive at the following set of equations:

$$\frac{d\bar{u}}{db} = \frac{f\beta(1-\theta)\frac{\gamma}{\epsilon_D \bar{u}} - 2\theta b}{1 - \alpha(1-\theta) - \frac{\theta\beta}{\bar{u}^2}} \tag{4.48}$$

$$\frac{d\alpha}{db} = -f\frac{\gamma}{\epsilon_D \theta} + (1-\alpha)\left(\frac{\bar{u}^2}{\theta\beta} - 1\right)\frac{1}{\bar{u}}\frac{d\bar{u}}{db} \tag{4.49}$$

$$\frac{d\gamma}{db} = \frac{d\alpha}{db} - f\alpha\left(\epsilon_w - \frac{\lambda(1-\alpha)}{\bar{u}^2}\right) \tag{4.50}$$

The second downstream (∞) boundary condition is the same balance between transverse ambipolar diffusion and ionization used in the constant speed case, which is now:

$$1 - \alpha_\infty = \frac{C_a u_\infty^2}{S_{ac} G^2 h^2} = \frac{\epsilon_w \bar{u}_\infty^2}{\lambda} \tag{4.51}$$

Additional boundary conditions are the conditions at the injector wall, and the internal boundary conditions at the sonic passage point. The injector wall condition (4.10) still holds, except in the nondimensional form it is now

$$\gamma_o = \alpha_o\left(1 + \frac{\sqrt{\beta}}{\bar{u}_o}\right) \tag{4.52}$$

where the speed at the inlet wall, $\bar{u}_o$, is now a result of the calculation, rather than a freely chosen value, as was the case in the constant speed problem.

If subsonic injection is assumed, then smooth passage through a "sonic point" [46] is required in the steady state. The sonic point is characterized as a singularity that occurs when the denominator of $\frac{d\bar{u}}{db}$ (equation 4.48) is zero at some $b = b_s$. In order to be physically possible, the numerator must be zero at the same b_s. This poses a difficulty in the full set of equations, since trajectories diverge rapidly near this singularity.

Therefore an "outer" set of equations is used "far" from the wall (on the ambipolar diffusion scale), but still within the acceleration layer - and the sonic point is found to be embedded in this intermediate layer. Since $\epsilon_D \ll 1$, diffusion is dropped ($\frac{d\gamma}{db} \approx 0$) and the combination γ/ϵ_D is eliminated from equations 4.48 and 4.49, arriving at the nondiffusive layer equations:

$$\frac{du}{db} = \frac{\beta(1-\theta)\frac{f\alpha}{\bar{u}}\left(\frac{\lambda(1-\alpha)}{\bar{u}^2} - \epsilon_w\right) - 2b}{1 - \frac{\theta\beta}{\bar{u}^2}\left(1 + \frac{\alpha(1-\theta)}{\theta}\right)} = \frac{N}{D} \tag{4.53}$$

where N and D are shorthand for the numerator and denominator, and

$$\frac{d\alpha}{db} = -f\alpha\left(\frac{\lambda(1-\alpha)}{\bar{u}^2} - \epsilon_w\right) \tag{4.54}$$

The ion slip flux may be obtained from post-processing as:

$$\frac{\gamma}{\epsilon_D} = -\frac{\theta}{f}\left[\frac{d\alpha}{db} - (1-\alpha)\left(\frac{\bar{u}^2}{\theta\beta} - 1\right)\frac{1}{\bar{u}}\frac{d\bar{u}}{db}\right] \tag{4.55}$$

The variables at sonic point (where the denominator of equation 4.53 is zero) may all be found explicitly by setting both the numerator and denominator of equation 4.53 equal to zero,

$$N = \beta(1-\theta)\frac{f_s\alpha_s}{\bar{u}_s}\left(\frac{\lambda(1-\alpha_s)}{\bar{u}_s^2} - \epsilon_w\right) - 2b_s = 0$$

$$D = 1 - \frac{\theta\beta}{\bar{u}_s^2}\left(1 + \frac{\alpha_s(1-\theta)}{\theta}\right) = 0$$

and using the integrated momentum equation (eqn. 4.37), evaluating the constant, F once $\bar{E}$ and b_∞ are chosen:

$$\frac{F}{m_i G u_{ref}} = b_\infty^2 + \bar{u}_\infty + \frac{\beta(\theta + \alpha_\infty(1-\theta))}{\bar{u}_\infty} = b_s^2 + \bar{u}_s + \frac{\beta(\theta + \alpha_s(1-\theta))}{\bar{u}_s}$$

These last three equations may then be solved for b_s, α_s, and u_s. The derivatives at the sonic point are evaluated as follows. L'Hopital's Rule is applied to equation 4.53:

$$\left[\frac{d\bar{u}}{db}\right]_s = \left[\frac{\frac{dN}{db}}{\frac{dD}{db}}\right]_s$$

These non-diffusive equations are used to march back toward the wall (using a Runge-Kutta variable-step routine) from the sonic point (and also from the sonic point out to ∞ for the magnetic diffusive layer) until the slip γ becomes positive, and then patched with the diffusive solution, equations 4.48 to 4.50, are to get to the wall itself. The diffusive set is required to meet the boundary condition on the slip.

At this point, we have solved the problem from the wall ($b = 1$) to the end of the magnetic diffusion layer (where $\bar{E} = \bar{u}_\infty b_\infty$). This process yields a family of $b_\infty(\bar{E})$ for each $\bar{E}$, each of which satisfies the boundary conditions. Thus, there is one remaining degree of freedom. The problem is closed via an idealized channel downstream (the "outer" magnetic problem), where the flow is assumed to be constant temperature, frozen (at $\alpha = \alpha_\infty$), and "back-emf dominated" ($\bar{E} - \bar{u}b \ll \bar{E}$). The magnetic field is then a function of the area of the channel, and we look for the throat. [46] In this outer region, (switching to dimensional variables), $\phi = EH$ is a constant, so that the speed and density ($m_i n_g = \dot{m}/(uA)$) are

$$u = \frac{\phi}{BH} \qquad m_i n_g = \frac{B}{\phi}\frac{\dot{m}}{w}$$

and the pressure, from equation 4.40 is

$$p = \frac{B}{\phi}\frac{\dot{m}}{w} v_B^2(\theta + \alpha_\infty(1-\theta))$$

so that the momentum equation, becomes

$$d\frac{u^2}{2} + \frac{1}{m_i n_g}\left(dp + d\frac{B^2}{2\mu_o}\right) = 0 \tag{4.56}$$

Using the expressions for u, $m_i n_g$, and p above, and the nondimensional variables and parameters already defined, plus the nondimensional potential,

$$\bar{\phi} = \frac{\phi}{E_{ref} H_t}$$

then equation 4.56 may be recast and integrated to obtain the following expression:

$$\frac{H_o}{H} = b\sqrt{\frac{1}{b_\infty^2} + \frac{2\beta(\theta + \alpha_\infty(1-\theta))\ln(\frac{b_\infty}{b})}{\bar{\phi}^2} + \frac{4(b_\infty - b)}{\bar{\phi}}} \tag{4.57}$$

We then find the throat, given b_∞ and $\bar{E}$, by evaluating this expression for decreasing b until H_o/H is minimized. In practice, the contraction ratio, H_o/H_t is taken as a given, and equation 4.57 gives another relationship between $\bar{E}$ and b_∞.

This closes the problem for a given set of the parameters, at a fixed value of the electron temperature. The numerical integrations are solved using a Runge-Kutta space-marching scheme, starting at the sonic point (non-diffusive equations), and marching out both towards b_∞ and b_o. The diffusive (equations 4.48, 4.49, and 4.50) and non-diffusive (equations 4.53 and 4.54) solutions are patched just after the outer, non-diffusive set value for γ is small and positive (> 0.001), and then the diffusive inner set is integrated to the wall. Note that γ is positive and of order unity near to the wall (ions lagging the bulk flow, as required by the inlet boundary condition), but becomes small and negative (ions leading) downstream of the diffusion layer. and that the patch is made near to the crossover.

4.3.2 Results with T_e as a Parameter

Following are results from the inner-outer approach to the accelerating ignition problem as described above. The plots vs ξ have been truncated so as to show the ionization layer more clearly. A "standard" set of parameters is defined in this work corresponding to roughly $T_e \approx 20000K$, $H = 0.02m$, $G \approx 7.5 \times 10^{24}\ m^{-2}/s$: $\lambda = 2$, $\epsilon_D = 0.005$, $\epsilon_w = 0.1$, $\beta = 0.05$, $\theta = 0.10$, and $q = 0.001$. Since the ionization rate coefficient varies the most dramatically with temperature of the parameters, as can be seen in figure 4.18, λ will be varied while the other parameters are fixed. For reference, figure 4.19 shows the behavior of both ϵ_D and q vs electron temperature, and figure 4.20 shows the variation of ϵ_w.

A summary of the results from several runs using the "standard" parameters is listed in table 4.4. Note that increasing contraction ratio ($\frac{H_o}{H_t}$) decreases b_∞, which means that less current is drawn in the ionizing region. Table 4.5 shows the ($\bar{E}$, b_∞) pairs calculated for

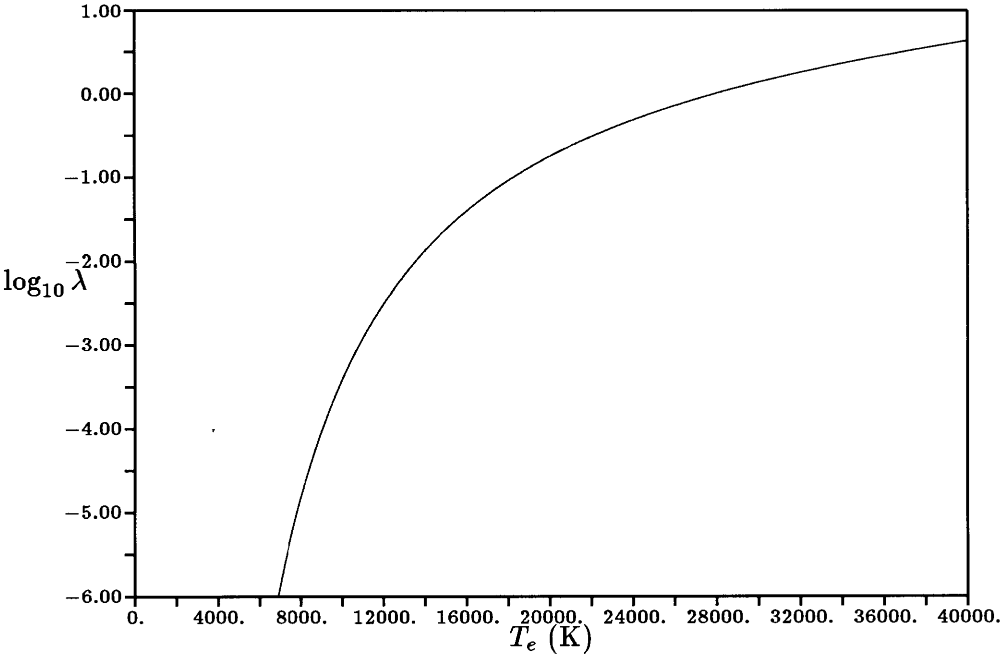

Figure 4.18: The parameter λ vs. T_e.

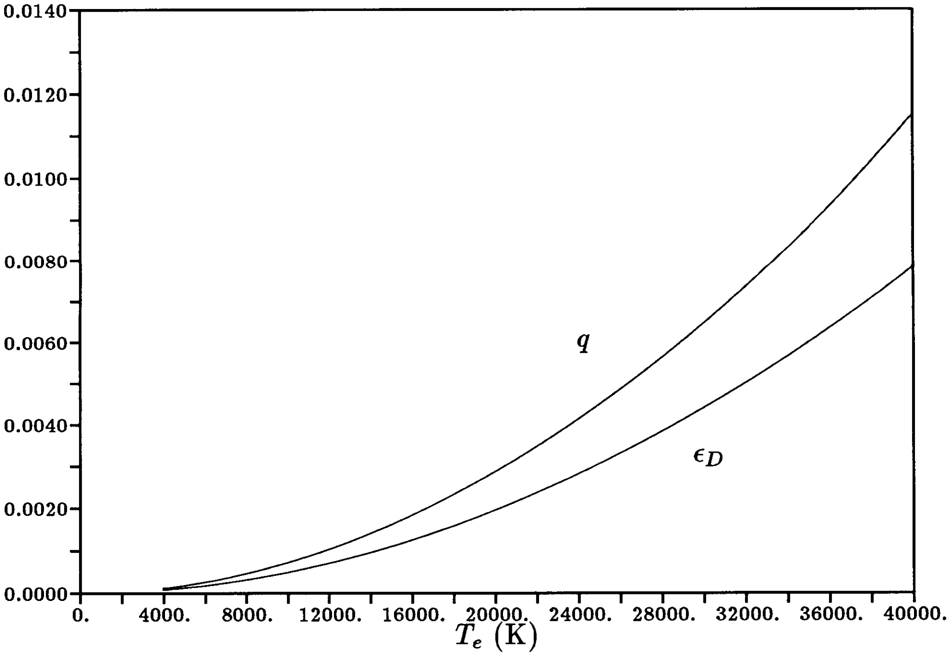

Figure 4.19: The parameters ϵ_D and q vs. T_e.

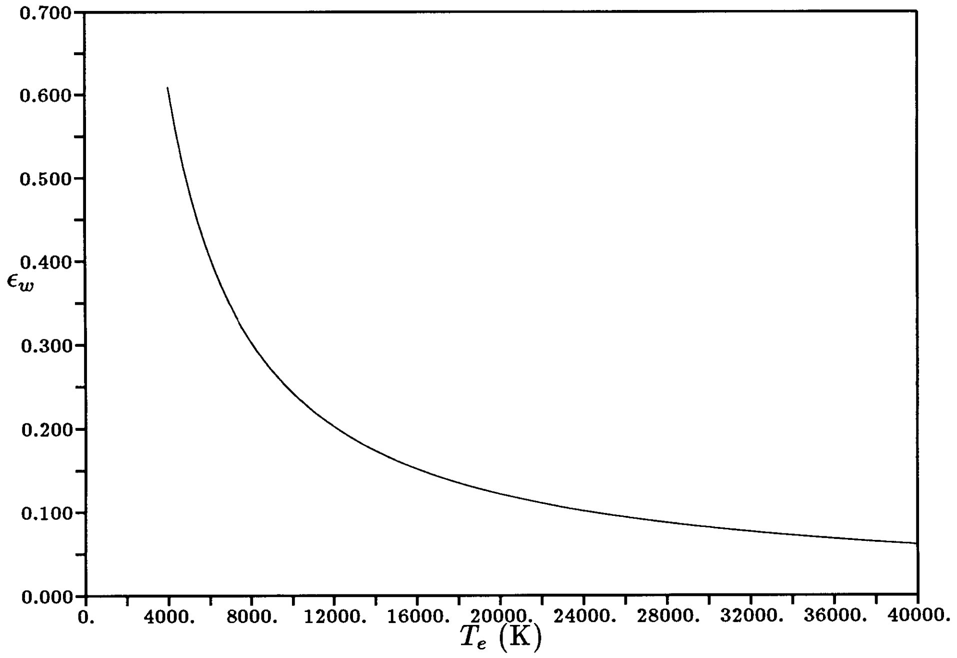

Figure 4.20: The parameter ϵ_w vs. T_e.

varying values of the parameter λ, keeping the other "standard" parameters fixed, and contraction ratio of 1 (constant area). Lower λ means lower electron temperature, and results in lower power drawn which is $2\bar{E}_o(1 - b_\infty)$ in the accelerating zone, and correspondingly smaller $u_\infty = \bar{E}_o/b_\infty$.

Figure 4.21 shows the trajectory on the γ,α phase plane for the standard set of parameters, and a contraction ratio of one ($\bar{E}_o = 0.6019$, $b_\infty = 0.6583$). The diffusive and non-diffusive solutions are patched at $\gamma = 0.0036$, $\alpha = 0.5592$, and the sonic point is at $b = 0.9854$, $\alpha_s = 0.9029$. The isoclines are for the diffusive inner set at $b = 1$, using equation 4.37 to solve for $u(\alpha)$ and are evaluated as

$$\frac{d\gamma}{d\alpha} = \frac{\frac{d\gamma}{db}}{\frac{d\alpha}{db}}$$

Note that, although the inner equations diverge as $\gamma \to 0$ (as can be seen from the isoclines), the outer set passes through smoothly, and the two sets patch quite well at a small positive γ, as can also be seen from the isoclines.

Figure 4.22 shows the ionization fraction, α, vs the nondimensional length, $\xi = x/\Lambda_m$, for the "standard" parameters, except that λ (basically the ratio of the acceleration to the ionization lengths) is varied as discussed above. Note that for small λ, the ionizing scale

$\bar{E}_o$	b_∞	$\frac{H_o}{H_t}$	$\bar{\phi}$
0.6019	0.65828	1.000	0.6019
0.5500	0.80658	1.078	0.5929
0.5000	0.86227	1.157	0.5784
0.4500	0.90275	1.243	0.5595
0.4000	0.93459	1.341	0.5364
0.3500	0.95983	1.453	0.5087
0.3000	0.97913	1.586	0.4758
0.2500	0.99181	1.748	0.4370

Table 4.4: Summary of results from the "standard" case.

λ	$\bar{E}_o = \bar{\phi}$	b_∞
4.00	0.6136	0.67116
2.00	0.6019	0.65828
0.50	0.5560	0.65633
0.30	0.5280	0.64731
0.20	0.4978	0.63030

Table 4.5: Summary of results, standard case, except varying λ, constant area $(H_o/H_t = 1)$.

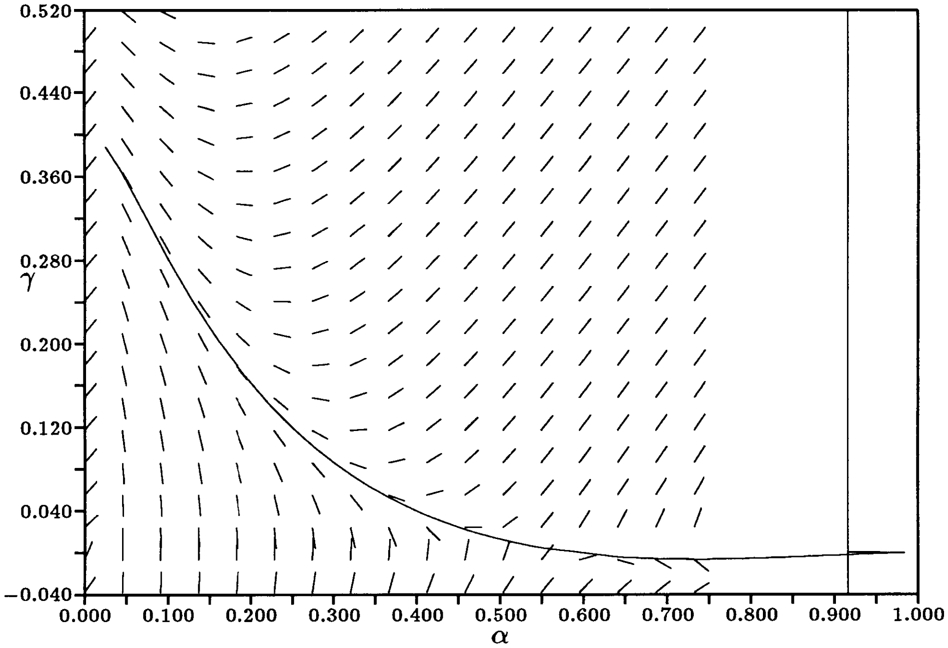

Figure 4.21: γ vs α, with inner-set isoclines, for the "standard conditions".

approaches that of the magnetic scale ($\xi \approx 1$). At higher λ, the ionizing scale is decidedly smaller than the magnetic scale, approaching $\xi \approx \epsilon_D$. As found with the constant speed case, again higher λ yields a higher α_o.

Using equation 4.40 in the integrated momentum equation (equation 4.37), and with constant $G = n_g u$ in the ionization zone, and using the nondimensional variables and parameters defined above,

$$\bar{u} + \frac{\beta(\alpha + (1-\alpha)\theta)}{\bar{u}} + b^2 = \frac{F}{m_i G u_{ref}} \tag{4.58}$$

For small ("subsonic") speeds, $\bar{u}^2 \ll \beta(\alpha + (1-\alpha)\theta)$, the acceleration comes mostly from the pressure gradient (which is strongly dependent on the gradient of α in this model), so that

$$\frac{\beta(\alpha + (1-\alpha)\theta)}{\bar{u}} \approx \frac{F}{m_i G u_{ref}} \tag{4.59}$$

which depends strongly on the ionization process, and hence on the value of λ. For large $\bar{u}$ ("supersonic"), the acceleration comes chiefly from the changing magnetic field:

$$\bar{u} + b^2 \approx \frac{F}{m_i G u_{ref}} \tag{4.60}$$

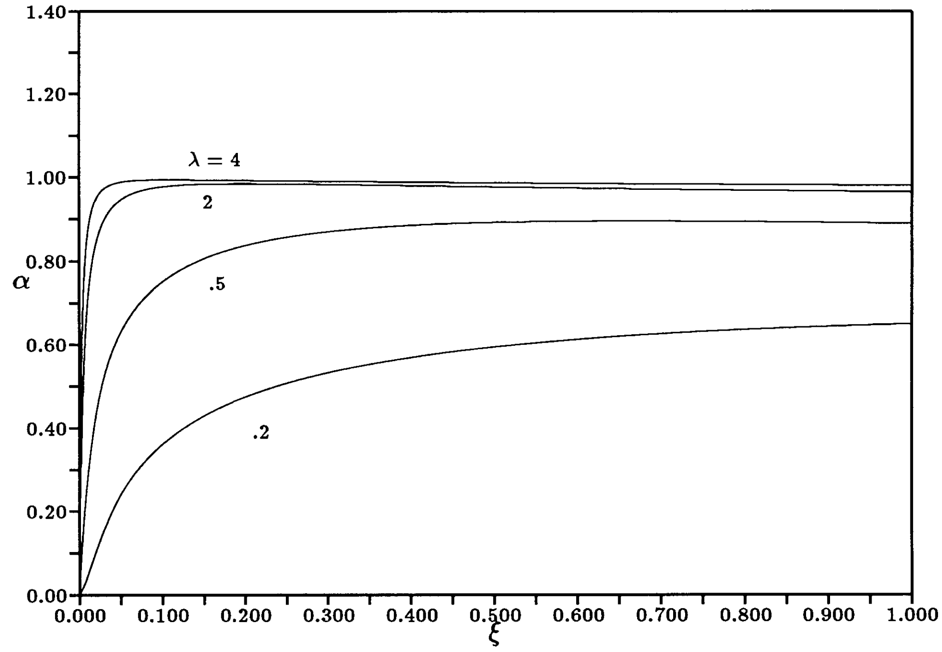

Figure 4.22: Ionization fraction α vs ξ for the "standard" parameters, except for varying λ.

which does not depend very strongly on λ so long as the entire ionization region is Coulomb dominated. Figure 4.23 shows the speed vs ξ for the same conditions as in figure 4.22, and, as discussed above, the differences in the accelerations near to the inlet are attributable to the variation in λ.

Note also on figure 4.23 that $\bar{u}_\infty$ (the asymptotic value of the speed) increases with λ. Since b_∞ has been found to not vary as much as $\bar{u}_\infty$, this means that the electric field will increase with λ as well. This agrees with the findings of Lawless and Subramaniam [42], who state that the back-EMF in a one dimensional self-field MPDT channel increases with the ionization rate at the sonic point. Figure 4.24 shows this in a plot of the calculated $\bar{\phi}$ vs the ratio $\frac{H_o}{H_t}$ for various λ. The ideal values are taken from Martinez [46].

An ignition criterion similar to the one for constant speed and temperature is again a constraint on the Damkohler coefficient for ionization, $\Lambda_1 \approx \epsilon_D \lambda$, and $4\epsilon_D \lambda > \bar{u}_o^2$.

The speed at the inlet wall, $\bar{u}_o$, can be estimated from equation 4.59, where F is evaluated at the ∞ end of the magnetic diffusion layer:

$$\frac{F}{m_i G u_{ref}} = \bar{u}_\infty + \frac{\beta}{\bar{u}_\infty} + b_\infty^2$$

so that, from equation 4.59, the inlet speed can be estimated as

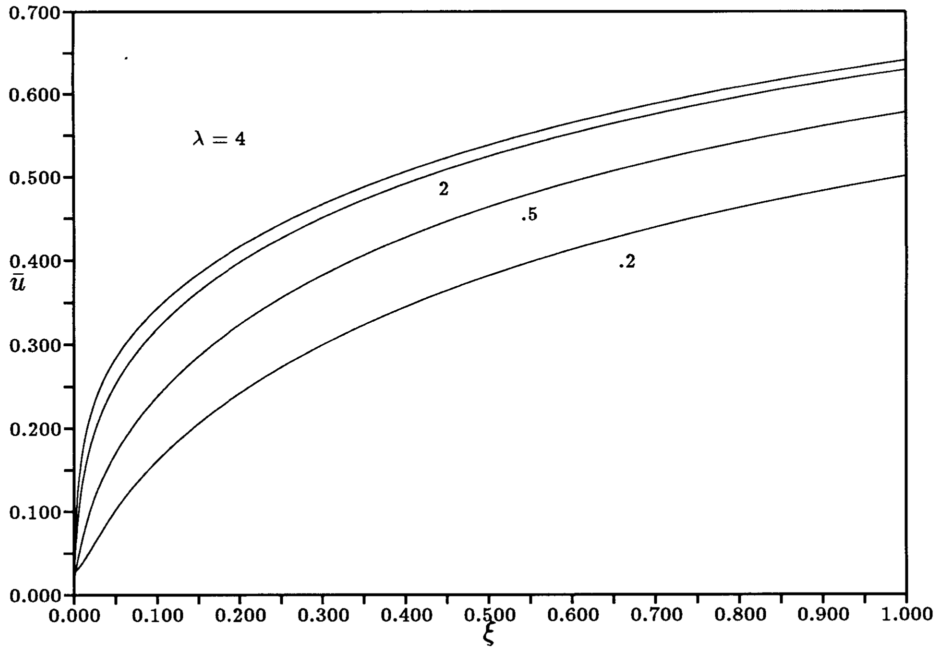

Figure 4.23: Plasma speed $\bar{u}$ vs ξ for the "standard" parameters, except for varying λ.

$$\bar{u}_o \approx \frac{\bar{u}_\infty}{\frac{\bar{u}^2+b_\infty^2\bar{u}_\infty}{\beta} + (\alpha_\infty + (1-\alpha_\infty)\theta)}$$

For large $\frac{\bar{u}^2+b_\infty^2\bar{u}_\infty}{\beta}$ (or large $\bar{u}_\infty$, if β is fixed), then

$$\bar{u}_o \approx \frac{\beta}{\bar{u}_\infty}$$

which is likely to be small enough to meet the rough ignition criterion (unless the temperature is very low), $4\epsilon_D\lambda > \bar{u}_o^2$, which is

$$\left(\frac{E}{B_\infty}\right)^2 = u_\infty^2 > \frac{v_B^4}{4C_aS_{ac}}$$

Although $E/B_\infty = u_\infty$ drops as the contraction ratio increases, the inlet speed changes little, and in fact drops with increasing contraction ratio. Therefore this can be only considered as a rough explanation, that the ionizing scale is smaller than the magnetic diffusion or acceleration scale when Thus this model is not yet in line with Heimerdinger's experimental findings [27], which indicated that there is an ignition-driven limit on the contraction ratio. In order to obtain a more clear ignition criterion, an energy balance is necessary, as outlined in the next section.

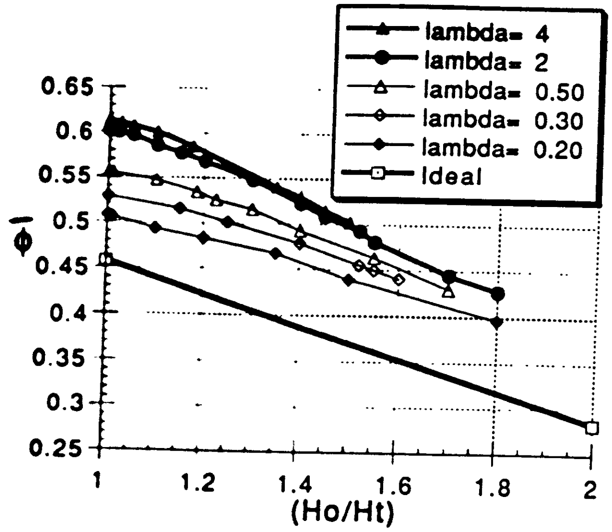

Figure 4.24: ϕ vs $\frac{H_o}{H_t}$

4.3.3 Overall Energy Balance

Figure 4.24 shows the overall results of the accelerating model; however, the electron temperature, and therefore the parameters of the problem (namely λ for this figure) are functions of the contraction ratio. This means that, for fixed channel throat dimensions and flow rate, there may be only one λ for each contraction ratio. This is caused by the energy balance in the ionization zone. Adding an energy balance to this model therefore makes it self-consistent and will indicate a more definite ignition criterion.

Assuming infinite thermal conductivity, which implies a constant electron temperature, and is consistent with the constant temperature assumption made previously, the integrated energy equation, as reported by Lawless and Subramanian [41] is

$$m_{,}G\left[h + \frac{u^2}{2}\right] + \frac{EB}{\mu_o} = C$$

which is valid for the constant area region assumed for the ionization-acceleration zone. C is a constant of the flow, and the enthalpy, h, is defined as

$$h = \alpha\left(\frac{5}{2}\frac{k_B T_e}{m_i} + \frac{eV_i}{m_i}\right)$$

for frozen heavy species temperature, T_g. The energy balance, for constant temperature, and using the nondimensional variables and parameters, is now:

$$2\dot{E}(1 - b_\infty) = (\alpha_\infty - \alpha_o)\left(\frac{5}{2}\beta(1-\theta) + \delta\right) + \frac{1}{2}(\bar{u}_\infty^2 - \bar{u}_o^2)$$

where

$$\delta \equiv \frac{eV_i}{m_i u_{ref}^2}$$

and $\delta = 0.59$ for the argon atom, and the u_{ref} defined here. This depends on conditions, of course. In fact, $\delta \to 1$ is a rough onset criteria; i.e., the flow kinetic energy approaches the ionization potential energy of the atom.

If $\alpha_\infty \gg \alpha_o$, and $\bar{u}_\infty \gg \bar{u}_o$, which has been generally found in the results of the accelerating ignition model, then

$$2\bar{E}(1 - b_\infty) = \alpha_\infty \left(\frac{5}{2}\beta(1-\theta) + \delta\right) + \frac{\bar{u}_\infty^2}{2}$$

Since, from the far-downstream condition,

$$\alpha_\infty = 1 - \frac{\epsilon_w \bar{u}_\infty^2}{\lambda}$$

and $\bar{u}_\infty = \bar{E}/b_\infty$

$$2\bar{E}(1 - b_\infty) = \left(1 - \frac{\epsilon_w \bar{E}^2}{\lambda b_\infty^2}\right) \left(\frac{5}{2}\beta(1-\theta) + \delta\right) + \frac{1}{2}\frac{\bar{E}^2}{b_\infty^2}$$

or, rearranging,

$$2\bar{E}(1 - b_\infty) - \frac{1}{2}\frac{\bar{E}^2}{b_\infty^2} = \left(1 - \frac{\epsilon_w \bar{E}^2}{\lambda b_\infty^2}\right) \left(\frac{5}{2}\beta(1-\theta) + \delta\right)$$

Which is now a function of the temperature-dependent parameters, and the $(\bar{E},\ b_\infty)$ solution pair. This condition sets the electron temperature, and an iterative process has to be carried out in order to satisfy it. It indicates that there must be enough energy left over after the acceleration to overcome the frozen losses due to the ionization.

Note that $2\bar{E}(1 - b_\infty) - \frac{1}{2}\frac{\bar{E}^2}{b_\infty^2}$ decreases with increasing contraction ratio, H_o/H_t, as shown by table 4.6. Physically, this means that more of the available energy is converted into accelerating the fluid. However, this leaves less energy available for the ionization process.

Table 4.7 lists a set of self consistent results obtained by iteration. They show that increasing the contraction ratio does indeed lower λ, corresponding to a lower electron temperature. Note that varying the contraction ratio from 1 to 1.08 results in an approximately 10 percent decrease in the electron temperature.

$\bar{E}$	b_∞	$\frac{H_o}{H_t}$	$2\bar{E}(1-b_\infty)-\frac{1}{2}\frac{\bar{E}^2}{b_\infty^2}$
0.4746	0.6272	1.00	0.0676
0.4630	0.6892	1.02	0.0621
0.4100	0.7940	1.13	0.0356
0.3500	0.8620	1.27	0.0147

Table 4.6: Results using $\lambda = 0.15$, $\epsilon_w = 0.3$, $\beta = 0.02$.

λ	$\bar{E}$	b_∞	$\frac{H_o}{H_t}$	T_e(K)
0.199	0.4862	0.62844	1.000	20440
0.150	0.4630	0.68922	1.020	19450
0.125	0.4420	0.71907	1.044	18910
0.100	0.4112	0.74651	1.080	18220

Table 4.7: Self-consistent results, for $\epsilon_w = 0.3$, $\beta = 0.02$.

As seen earlier, decreasing λ leads to longer ionizing regions. This then is the key to an ignition criterion for the accelerating ignition which is consistent with the assumptions made for the model. Increasing the contraction ratio decreases the uniform electron temperature, thereby decreasing λ, and increasing the ionization region's width. If the contraction ratio is increased continuously, at some point the ionizing region will grow to be of the same scale or larger than the acceleration scale. After this point, increasing the contraction ratio will result in extinction, that is, the ionizing front will exit from the thruster, or it may be considered to have been "blown out" of the channel by convection.

Figure 4.25 shows the ionization fraction profiles for the low and high temperatures in table 4.7.

4.4 Summary

These models show that the assumption that back-diffusion of electrons to the inlet wall can explain ignition is valid, and also explain why ignition may fail under some conditions. This explanation is purely based on convective and diffusive transport and volumetric production by inelastic collisions, and does not require any significant non-consistent assumptions, other

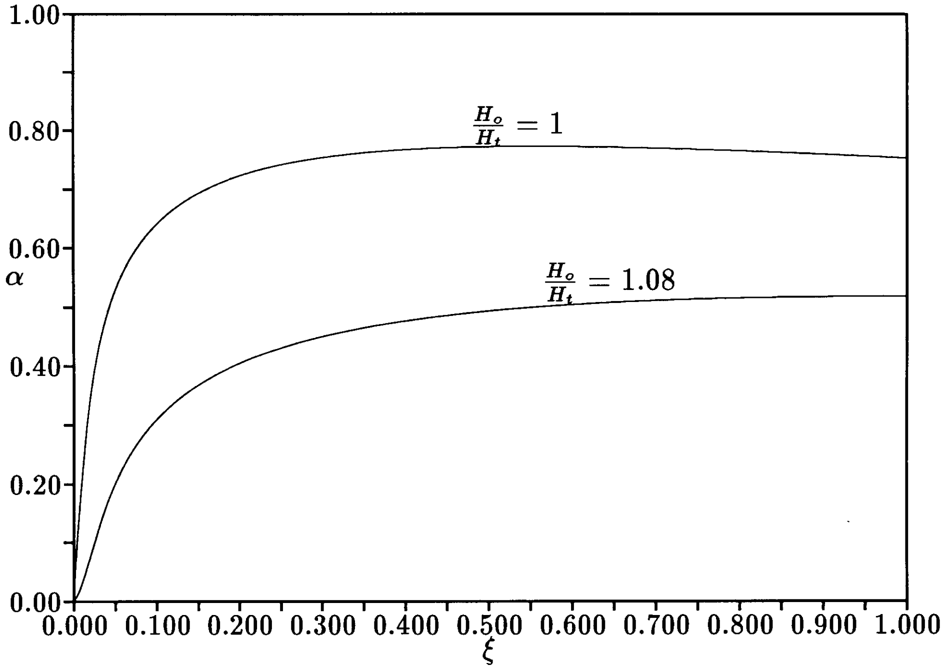

Figure 4.25: Energy consistent ionization fraction α vs ξ corresponding to the high and low temperature cases from table 4.7

than that the electrons are Maxwellian (other distributions would effect the calculation of the rate coefficients).

For atomic injection, the general ignition criteria is based on the ionization Damkohler number, and is that the flow speed must be lower than the blowoff speed characterized by the ambipolar diffusion coefficient (multiplied by the overall density) and the electron-atom ionization rate coefficient at the inlet:

$$u_o < u_{bo} = 2\sqrt{C_a S_{ac}(0)}$$

which is a function of the electron temperature. In the accelerating case, both the inlet velocity and the electron temperature are determined consistently.

Chapter 5

Discussion

5.1 Summary

In this section, the findings and contributions of this thesis will be summarized and discussed. The summary will be broken up into the two topics of nonequilibrium ionization modeling and inlet ignition.

5.1.1 Nonequilibrium Ionization Rate Modeling

A great deal of research has been published on the topic of nonequilibrium ionization, and on the modeling of nonequilibrium ionization rates. The study of multi-level finite-rate ionization in this thesis extends this work by reformulating the standard model in a way that both isolates and highlights the effects of individual levels, which allows for calculation of overall effects in a straightforward manner. The assumptions that allow this reformulation are checked throughout to ensure that they are applicable to the conditions typically found in MPDTs. The ability to calculate two-step (ground state and ion) overall rate coefficients - both with and without radiative effects - which include the effects of the more realistic multi-level (excited levels) structure of the atom or ion is a valuable tool for calculating, diagnosing, and/or understanding the state of the plasma in an MPDT.

The nonequilibrium ionization models developed in this thesis utilize a reformulation of the standard collisional-radiative rate equations to calculate the population distribution of the excited states of an atom and/or ion. Once the excited state population distribution is known, the overall ionization and recombination rate coefficients may be calculated. These may be used in channel flow models of magnetoplasmadynamic thrusters. While the most relevant result of this study to this thesis is the calculation of the overall rate coefficients, the population distribution of the excited states is studied using a simple model for a variety of conditions.

A realistic ionization model for both hydrogen and argon atoms and the argon first ion (and the structure to extend to additional atoms and ions) is developed which allows us to go back and look at the details of the excited state population densities - a critical need for considering line radiation, or spectroscopic diagnostics (emission). These models are based on the the atom or ion as a ground state, its excited states, and the continuum, or next higher ion. Rate equations which include collisional and radiative (in parametric form) transitions amongst these states are written in a standard collisional-radiative (CR) form. The standard form is rewritten using the relative degree of nonequilibrium of each level rather than the level population as the variable. This modified CR model is more convenient for the analysis that follows.

Analysis using the full multi-level argon atom modified CR model indicates that the excited states will relax much faster than does the ground state, which is tied to the mechanical flow time scales (which may be convective and/or diffusive). This is shown in this work to be so both in the bulk channel flow of an MPDT and in the inlet regions of an accelerator where axial diffusion may be significant. This leads to the quasi-steady-state-solution (QSSS) approach. Starting with this assumption, the excited state population distribution may be characterized by two coefficients for each excited level, one of which is mostly determined by collisional effects, and one mostly determined by radiative effects. Each excited level's population is then given as a function of these two coefficients and the ground state degree of nonequilibrium.

It was shown that the overall rate coefficients for both the atom and ion may be calculated as functions of T_e alone, if the plasma is not radiatively affected, and as functions of the electron temperature and density and the radiative escape factors when it is. Simple 3-level (ground, excited state, continuum) argon and hydrogen atomic models were then used to analyze the radiative effects on both the population of the excited state and the overall recombination rate coefficient. Using the QSSS assumption, the effect of radiative decay is to raise the recombination rate coefficient, both by direct radiative recombination, and through radiative influence on the excited state populations. Overall microreversibility is found to be valid only when radiative processes are negligible; this occurs when the escape factors are small, the temperatures are very high, and/or the electron density is high. Note that overall microreversibility also fails when the quasi-steady-state approximation cannot be used.

Two distinct regimes were identified in the calculation of the overall collisional rate coefficients (neglecting radiation). At temperatures below roughly $T_e = 20000\ K$, the most significant contribution to the overall recombination rate coefficient came from the excited levels, while above the $T_e = 20000\ K$, the most significant contribution came from the ground state. In fact, the three-level model results matched well with the multi-level results at high electron temperatures. This means that the rigor of the full multi-level model is not necessary at high temperatures if the goal is to calculate overall rates since the net rate of production of ions from each of the excited levels is much less than the net rate from the ground and first excited levels.

The overall collisional rate coefficients for the argon atom and the hydrogen atom presented here were developed primarily for use in the analysis of the ignition problem in this thesis. They are also applicable as volumetric source terms in continuity equations in other computational models of plasma accelerators. In these cases, the recombination rate coefficients calculated in Chapter 3 from the multi-level model with no radiative effects is used, and overall microreversibility applies in calculating the overall ionization rate coefficient. Niewood [51] has used the argon atom ionization model of this work in a detailed computational study of MPDTs. Miller [48] used the hydrogen ionization model in a computational study of arcjet thrusters, including multifluid nonequilibrium effects. In both cases, accurate calculation of the ionization fraction, far out of equilibrium under some thruster conditions, is necessary for those transport properties sensitive to ionization fraction, and for determining the frozen losses due to the endothermic ionizing reaction.

These uses, plus the use of the ionization models in the ignition analysis of this thesis are indications that the overall rate coefficient model developed is compatible with a variety of numerical flow applications, and is practical, since the two-step form includes the effects of the excited levels without requiring any new, and most likely stiff, continuity equations to be added. Another advantage is that the effects of production of the second ion of argon could now be added to a model such as Niewood's [51] by using the model presented here, since argon second ions have been observed in MPDT experiments [36]. Although radiation effects were not included in the overall coefficient model here, they could be added parametrically if a consistent method for determining the radiative escape factors is used.

5.1.2 Inlet Ignition

The formulation and solution of the problem of ionizational ignition in this thesis represents the first published attempt to explain the sustained initiation of ionization in a self-field MPDT in a consistent and physically reasonable manner. The analysis uses the ionization rate model developed earlier in this thesis and considers subsonic injection into a flowing channel, with both local and non-local (gradient-driven) magnetoplasmadynamic effects. The models are all one dimensional, which limits the conclusions to be drawn. In the context of other work on this topic, which may treat the ionization front as a jump condition [12] [39], explain ignition in a spatially non-consistent manner [18], or use an unrealistic one-dimensional model of a self-field MPDT inlet [14], this level of analysis is justified as a reasonable proof that diffusion-driven ignition is possible, and as giving practical ignition criteria.

The hypothesis of the ignition analysis is that diffusion of electron-ion pairs back to the inlet wall provides enough electrons to initiate ionization. This is based on diffusion flames and diffusion-reaction models in general, where reactants mix primarily by diffusion. It is assumed that the injected propellant is essentially at zero ionization fraction, so the back-diffused electrons are the only ones available for initiating the ionization process. When back-diffusion is not sufficient for supplying the electrons to the wall, which occurs at higher injection speeds, then the ionization front is stretched and displaced downstream, or "blown off" of the inlet wall. At the inlet wall, the boundary condition that the ions enter a sheath (not modeled here) at the Bohm velocity is imposed, which makes the ionizing region a "pre-sheath".

In the simplest case considered, that of constant speed and temperature, ignition was characterized solely by a blowoff speed criterion. That is, if the speed is below the blowoff speed, then the back-diffusion of electron-ion pairs supplies enough electrons at the inlet wall to meet the inlet condition and result in a large enough ionization rate to sustain the front at the inlet wall (the inlet wall condition is met at ionization fractions generally greater than $\alpha \approx 0.001$). If the flow speed is above the blowoff speed, the ionization front was blown downstream (actually, stretched out, since the boundary condition used here was that some level of ionization occurs in the asymptotic limit), and the inlet wall condition is met at virtually zero ion density, since the back-diffusion cannot supply enough electrons near the inlet. The blowoff speed depends on both the overall ionization rate coefficient and the product of the ambipolar diffusivity and the overall density (note that the ambipolar diffusion coefficient is proportional to one over the overall density, so the blowoff speed is independent of the density), and so depends on the propellant choice. As expected, a large ionization rate coefficient is an advantage, but now high diffusivity is also a premium in choosing a propellant.

When temperature variation was accounted for in the constant speed model, there was a quantitative change in the ignition criterion, in that the inlet temperature is used in the evaluation of the blowoff speed, but no qualitative difference. In fact, since the inlet temperature was always higher than the downstream temperature, the addition of temperature variation to the model actually made ignition more likely, for equal downstream temperatures and injection speeds.

The final atomic injection case considered here was the constant temperature, atomic injection, accelerating model. This model was more difficult to solve due to the internal singularity (the sonic passage), and was broken up into two sets of coupled inner-outer problems, with the entire ionization region embedded in the magnetic inner layer. An overall energy balance, still assuming constant temperature, was needed to both make the problem self-consistent and to pin down an ignition criterion. This criterion is that, for a given set of physical constraints on the thruster, increasing the contraction ratio will eventually quench the ionization process by lowering the inlet temperature, the inlet ionization fraction.

Overall, the results indicate that back-diffusion of electrons and ion to the inlet wall against the bulk flow can explain the mm-scale ionization regions that have been observed in the past in MPDT experiments. Also, the "blow-off" criterion identifies the conditions under which ignition will fail. Since this criterion depends on the product of the ambipolar diffusion coefficient and the ionization rate coefficient (in atoms), propellants with small ionization potentials and/or masses will ignite most effectively.

5.2 Recommendations for Additional Work

One of the conclusions of this research, in fact, most research, is that there are many questions yet to be answered. Following, therefore are my recommendations for possible future research in each of the main topics of this thesis: nonequilibrium ionization modeling and inlet ignition.

5.2.1 Nonequilibrium Ionization Rate Modeling

As additional experimental interpretation is made and new analytical and computational techniques are used, the cross-section and rate models for individual transitions amongst the states are steadily improving. In particular, experimental verification of collisional cross-sections for state to state transitions between higher excited states is necessary to reduce the great uncertainties which come from applying models developed for lower state transitions. The more accurate recent cross-section and/or rate coefficients may be applied to the models of this thesis to increase the confidence in the results.

A more self-consistent approach would include the possibility of non-Maxwellian electrons in the plasma. This may result in higher rate coefficients (S_{ac}), as found by Chouieri, et al. [18], due to a superthermal tail in the elecron distribution. This additional level of realism would require that a very consistent and accurate accounting of the processes occurring in an MPDT be made in order to have confidence in the electron distribution obtained.

One way to extend the model developed in this thesis would be to apply the model to additional species of interest to MPDT and electric space propulsion in general. Some species which have been used in experiments and may be of interest are nitrogen and oxygen molecules, and lithium, helium, xenon and neon atoms. More complex molecules which have been used as propellants in electric propulsion devices, such as ammonia, water, and hydrazine, may also be modeled, but may require additional analytic tools. The extension of the ionization model to additional molecular species brings up the question of whether a similar methodology could be applied to the dissociation process as well. The goal would be to utilize the QSSS assumption to develop simple overall (two-step) dissociation/recombination models which still retain the influences of the vibrationally excited levels.

5.2.2 Inlet Ignition

In this thesis, ignition has been analyzed with one atomic species. Ignition with a wide variety of propellants, both atomic and molecular could be analyzed using the same simple models used in this thesis. In fact, the normalizations used allow the parameters to be easily varied to represent different species of interest.

The molecular injection problem should also be addressed. The main difference between this case and the atomic one is that now atoms are made available for ionization at the inlet only through the dissociation process, and since the dissociation rate coefficient is lower than the ionization rate coefficient for hydrogen, dissociation is the limiting process. Since electrons are present at the inlet only because of back-diffusion, the role of axial ambipolar diffusion is still significant.

Radiative effects were not included in the ignition model due to the short absorption length scales. However, as Burton and Tiliakos [14], Liberman and Velikovich [44], and much of the ionizing shock research done in the past has shown, radiation may have an effect on ionization at very low ionization fractions. Therefore some methodology for including radiative effects accurately in the ignition process when α is very low may be of great interest. As found in Chapter 4, this would occur as the Damkohler number approaches the critical value, or when the hypothesis that ignition is caused by back-diffusion begins to break down.

Though it seems improbable in a realistic MPD thruster, both from computational and experimental findings, supersonic injection has not been addressed in this work, and it remains to be seen whether it is possible. What physical processes influence ignition in this case? This may be similar to ionizing shock work, where several different processes act. For example, radiation may have an effect far ahead of the shock, while collisions will have their effect nearest to the shock itself.

A full 1-D model of ignition would be of an accelerating propellant, with full energy equations for electrons and heavy particles, and for both atomic and molecular propellant injection. Second, and perhaps third ions of argon may also be included, since they have been observed by their spectroscopic signature in experiments. The ignition model(s) should also be coupled with a more realistic MPDT model. The caveat here is that the ionizing zone in a successful ignition may much smaller than the other scales of interest in the thruster, so that an axial boundary layer representing the initial ionizing region may be patched onto the "outer" flow, similar to what was done in the accelerating model used here.

Consideration of more realistic 2 or 3 dimensional cases is necessary in order to truly understand how inlet the ionization works. This means tackling the problem of either slit or jet injection, along with the complications which may occur; for example, azimuthal electrical currents may be caused as the current avoids the low-conductivity injection jets.

Finally, the ignition models must be verified experimentally. In order to correspond to the 1-D assumption, a long channel with a small interelectrode gap should be used, similar to the recent work of Tahara, et al. [66]. Spectroscopic diagnostics would allow for nonintrusive measurements and the excited state population distribution may be estimated from the flow models, as shown in Appendix D. To test the models, mass flow rate, contraction ratio, may be varied and the resulting changes in the ionizing region width compared to the changes predicted by the analysis presented in this thesis.

Appendix A

Methods Used for Solving Flow Problems

The flow problems that are of interest to this thesis are mostly of the diffusion-reaction type. The problems are formulated such that at one or both ends of the range of the one-dimensional independent variable there is a singularity, and the downstream conditions are always approached asymptotically. In the accelerating flow case, there is also an internal resolvable singularity - the sonic point.

A.1 Using A Runge-Kutta Method to solve BVPs

One of the simplest ways to solve the 1-D steady flow problems addressed in this thesis is to employ a Runge-Kutta space marching scheme. Runge-Kutta methods are fairly standard multi-step time marching schemes, and are found extensively in the literature [56] [19]. In this case, a variable step size routine is used throughout. The boundary value problems of this work are then solved by a shooting method, if so required. For example, in the constant speed, constant temperature model of Chapter 4, any trajectory that connects the uniform downstream plasma to the inlet wall condition on the ion flux entering the sheath is a good solution. However, for the varying temperature case, another wall condition must be met simultaneously: that there is no electron heat conduction to the wall, and since this model was solved by the Runge-Kutta method, an iterative shooting process was used to find satisfactory solutions. That is, the integration starts at some point at which at least one guess is required to calculate all quantities, and then a check is made to see if the integration meets all of the boundary conditions. The guess is then refined until the conditions are met.

For the constant speed problems, the integrations start at "infinity" (the asympotically approached uniform downstream plasma) and end at the wall, where the presheath wall condition is checked as a figure of merit. In problems where there is acceleration, there is an internal singularity (sonic passage) which must be resolved, and two integrations are initiated at this internal singularity: one directed towards the wall, and one out to "infinity", as described in the accelerating ignition formulation in Chapter 4.

A.2 Using the *COLSYS* Relaxation Subroutine to Solve BVPs

The *COLSYS* package [3, 2, 6] was designed to solve boundary-value problems (BVPs) for ODES in one dimension, and has been used to solve many problems. (The package, in an updated form known as *COLNEW*, is available through NETLIB) The package solves a "mixed-order system of ODE's, subject to separated, multipoint boundary conditions" [3]. For the ignition prblem that the relaxation scheme was used for, the problem is a two-point boundary value problem (the downstream and inlet conditions).

A.2.1 Solving Problems with Unknown Bounds on the Independent Variable

For some of the cases considered in this work, solutions will be sought in which one of the endpoints for the independent variable is not known apriori. For example, in the constant speed ignition cases, the ionization fraction is used as the independent variable, and the ionization fraction at the inlet is unknown.

A method found in *Numerical Recipes* [56] was used to solve for this unknown boundary along with the dependent variables. Assuming that the independent variable is x, and the final value is known (x_f), then a new equation may be added, using the unknown initial value, x_o:

$$\delta = x_f - x_o \tag{A.1}$$

Note that δ is a constant, so that, equivalently, a new differential equation has been added:

$$\frac{d\delta}{dx} = 0 \tag{A.2}$$

Now the independent variable can be changed to t, defined as:

$$x = x_f - t\delta$$

The derivatives are rewritten using the new independent variable, t, with

$$\frac{dz(i)}{dt} \equiv f(i) = -\delta \frac{dz(i)}{dx}$$

Schematically, if the initial set of N differential equations to be solved over the domain, $x_o \leq x \leq x_f$ (x_o unknown apriori, and there must be $N+1$ boundary conditions), is

$$\frac{d}{dx}\begin{bmatrix} z(1) \\ \vdots \\ z(N) \end{bmatrix} = \mathbf{f}(x, z(1), \ldots, z(N)) \tag{A.3}$$

then the final set of $N+1$ differential equations, to be solved using the *COLSYS* package over the domain $0 \leq t \leq 1$, is

$$\frac{d}{dt}\begin{bmatrix} z(1) \\ \vdots \\ z(N) \\ \delta \end{bmatrix} = -\delta * \mathbf{f}'(x, z(1), \ldots, z(N), \delta) \tag{A.4}$$

where $\mathbf{f}'$ is the same as $\mathbf{f}$ with the addition of equation A.2, and $\delta = x_f - x_o$.

The user inputs to the COLSYS routine are, first, the set of derivatives, $f(i)$, plus the partial derivatives of each derivative w.r.t. each variable, denoted by $\frac{\partial f(i)}{\partial z(j)} = df(i,j)$. The boundary condition information is input in the form of $g(z(i),t) = 0$, and the partial derivative of $g(z(i),t)$ with repect to $z(j)$ is $dg(j)$. Finally, an initial guess for the solution is input as $z(i)(t)$, and the derivatives $dmval(j) = \frac{dz(i)(t)}{dt}$.

A.2.2 Example: The Constant Speed and Temperature Atomic Ignition Model

As an example of the method described above, it will be applied to the constant speed and temperature atomic injection ignition model from section 4.1.

Equation 4.16 is repeated below for convenience:

$$\frac{dg}{da} = 1 + \frac{\tilde{\Lambda}_1 a((a-1) + \tilde{\Lambda}_2(a^2-1))}{g} \tag{A.5}$$

In this case, the extra unknown is the value of a at the inlet: a_o. The stretch variable (see equation A.1) is chosen to be $\delta = 1 - a_o$, so that the variables

$$z(1) = \xi \qquad z(2) = g \qquad z(3) = 1 - a_o$$

so that $a = 1 - z(3)t$
where t is a new variable introduced: $0 < t < 1$. The derivatives w.r.t. t are $\frac{dz(i)}{dt} = f(i)$:

$$f(1) = -z(3)/z(2) \qquad f(2) = -z(3)(1 + \frac{\tilde{\Lambda}_1 a((a-1) + \tilde{\Lambda}_2(a^2-1))}{z(2)}) \tag{A.6}$$

$$f(3) = 0 \tag{A.7}$$

and the partial derivatives of each derivative w.r.t. each variable are denoted by $\frac{\partial f(i)}{\partial z(j)} = df(i,j)$:

$$df(1,1) = 0 \qquad df(1,2) = z(3)/z(2)^2 \qquad df(1,3) = -1/z(2)$$

$$df(2,1) = 0 \qquad df(2,2) = z(3)\frac{\tilde{\Lambda}_1 a((a-1)+\tilde{\Lambda}_2(a^2-1))}{z(2)}$$

$$df(2,3) = -1 - \frac{\tilde{\Lambda}_1(-2b+3b^2+\tilde{\Lambda}_2(9b^2-4b^3-4b))}{z(2)}$$

$$df(3,1) = 0 \qquad df(3,2) = 0 \qquad df(3,3) = 0$$

where $b = z(3)t$

The boundary conditions are, at $t = 0$ (the downstream asymptotic limit), $\gamma \to 0$, so that:

$$g = z(2) \qquad dg(2) = 1$$

while at $t = 1$ (the inlet), the boundary conditions are that the wall condition on the backflowing ions holds (see equation 4.11):

$$g = z(2) - (1 - z(3))(1 + v_B/u)$$

$$dg(2) = 1 \qquad\qquad dg(3) = (1 + v_B/u)$$

and that, also at $t = 1$ (the inlet), the axial coordinate is zero:

$$g = z(1) \qquad\qquad dg(1) = 1$$

In this case, the initial guess chosen was

$$z(1) = 1 - t \qquad z(2) = 0.25 - 0.249(1 - t) \qquad z(3) = 0.95$$

$$dmval(1) = 1 \qquad dmval(2) = 0.249 \qquad dmval(3) = 0$$

The inputs described above define the problem. Convergence was never a problem except at very high speeds where the wall boundary condition was met at $g = a = 0$, when more iterations were required. This method was used for the constant speed, constant temperature models with either atomic or molecular injection. The results from the atomic case, the approach outlined in this section, are given in Chapter 4.

A.2.3 Solving Problems With Internal (resolvable) Singularities using a Relaxation Method

Consider in general the problem of numerically solving a steady-state flow problem which includes a sonic passage (and therefore a resolvable singularity: the $\frac{d\bar{u}}{d\xi}\frac{0}{0}$ derivative at the sonic point). The 1-D, one fluid model of Martinez discussed above will be used as an illustrative example. The purpose of including this model here is to illustrate the use of a two-region approach to solve a steady-state problem with an internal singularity and to give the reader a reference for the types of variations expected in a magnetoplasmadynamic thruster. This approach would be helpful in simplifying the solution of the accelerating ignition model developed in Chapter 4, and make it a more practical analytic tool.

The set of differential equations for a 1-d self-field MPDT constant-area channel flow can be written as the set [50] [46]

$$\frac{d\bar{u}}{dx} = \frac{N(\xi, \bar{u}, b)}{D(\xi, \bar{u}, b)} \tag{A.8}$$

$$\frac{db}{dx} = f(\xi, \bar{u}, b) \tag{A.9}$$

where the denominator of the first derivative must pass through zero, $D(x, u, b) = 0$, somewhere in the solution domain. If this is a physically reasonable problem, then the numerator must also equal zero at this same point (smooth sonic passage), in order for a finite derivative to exist at the singularity. The boundary conditions are that $b = 1$ at $\xi = 0$ and $b = 0$ at $\xi = 1$.

This problem, as stated, must have two eigenvalues which are free, and are used to find the correct solution, subject to the boundary conditions [46]. These eigenvalues of the problem are necessary to fulfill the internal conditions that both the numerator and denominator reach zero at the same time. In this case, the eigenvalues may be the electric field and the sonic passage location. (alternatively, they could be an initial Mach number and the electric field)

The technique adopted here to solve such problems follows comments on solving BVP with internal singularities in the work of London and Flannery [45], and in *Numerical Recipes* (Press, Flannery, etal [56]) and the suggestion of Chanty [15]. The first step is to break the problem up into two domains, before and after the singularity. The internal singularity becomes a boundary condition for both domains, along with matching requirements. Also, since the location of the singularity is, in general, unknown, the location is another variable in the problem.

Thus the set of equations to solve could be written as the set of two differential equations

$$\frac{d\bar{u}}{d\xi} = \frac{N(x, \bar{u}, b, E, \xi_s)}{D(x, \bar{u}, b, E, \xi_s)} \tag{A.10}$$

$$\frac{db}{dx} = f((x, \bar{u}, b, E, \xi_s) \tag{A.11}$$

plus the two new differential equations for the unknown constants, ξ_s and $\bar{E}$:

$$\frac{d\xi_s}{d\xi} = 0 \tag{A.12}$$

$$\frac{d\bar{E}}{d\xi} = 0 \tag{A.13}$$

subject to the original boundary conditions, plus the following boundary conditions, at the unknown sonic position, x_s:

$$N(\xi, \bar{u}, b) = 0$$

$$D(\xi, \bar{u}, b) = 0$$

The physical domain is broken up into two subdomains, one from the inlet to the sonic point (the "upstream domain"), and the second from the sonic point to the exit (the "downstream domain"). A new nondimensional independent variable, t, is introduced, $0 \leq t \leq 1$, so that both subdomains may be solved simultaneously. Therefore, in the upstream subdomain, the axial position is $\xi = \xi_s t$, so that $t = 0$ is the inlet, and $t = 1$ is the sonic point. In the downstream domain, $\xi = 1 - (1 - \xi_s)t$, so that $t = 0$ is the exit, and $t = 1$ is again the sonic point.

Separate sets of differential equations A.10 - A.13 are set up for each subdomain, and the domains are solved as coupled boundary value problems.

A.3 The 1-D One-Fluid MPD Channel Flow of Martinez

As an introduction to both self-field MPD thruster behavior and the solution method adopted here for problems with either or both boundary singularities or internal resolvable singularities, the simple one-fluid, 1-D model of Martinez [46] is used. Defining the following reference values:

$$u_{ref} = \frac{B_o^2}{2\mu_o}\frac{A^*}{\dot{m}} \qquad E_{ref} = u_{ref}B_o \qquad \rho_{ref} = \frac{\dot{m}}{A^* u_{ref}}$$

The nondimensional variables of Martinez [46] are:

$$U = \frac{u}{u_{ref}} \qquad \mathcal{E} = \frac{E}{E_{ref}} \qquad \bar{\rho} = \frac{\rho}{\rho_{ref}}$$

$$\bar{p} = \frac{pA^*}{u_{ref}\dot{m}} \qquad \bar{h} = \frac{h}{u_{ref}^2} \qquad b = \frac{B_z}{B_o}$$

$$J = \frac{j\mu_o L}{B_o} \qquad a = \frac{A}{A^*} \qquad \vec{\xi} = \frac{\vec{r}}{L}$$

Using these variables, then the nondimensional overall continuity, momentum, and magnetic field equations are

$$\bar{\rho}\bar{u}a = 1 \tag{A.14}$$

$$\bar{\rho}\bar{u}\frac{d\bar{u}}{d\xi} + \frac{d}{d\xi}(\bar{p} + b^2) = 0 \tag{A.15}$$

$$\frac{db}{d\xi} = -R_m(\bar{E} - \bar{u}b) \tag{A.16}$$

and the integrated energy equation is:

$$\bar{h} + \frac{\bar{u}^2}{2} + 2\bar{E}b = \bar{h}_{t0} + 2\bar{E} \tag{A.17}$$

where the total inlet enthalpy is:

$$\bar{h}_{t0} = \bar{h}_0 + \frac{u_0^2}{2} \tag{A.18}$$

(Martinez used a total inlet enthalpy corresponding to a total temperature of $400K$, in the nondimensional variables, this is $\bar{h}_{t0} = 0.003267$ [46]) These equations can be combined to obtain two differential equations for the magnetic field, which is simply equation A.16 and for the speed:

$$\frac{d\bar{u}}{d\xi} = \frac{-2R_m(\bar{E} - \bar{u}b)(\bar{E} - \frac{5}{2}\bar{u}b)}{\frac{5}{2}\bar{p}(M^2 - 1)} = \frac{N(\bar{u}, b)}{D(\bar{u}, b)} \tag{A.19}$$

where the Mach number is:

$$M^2 = \frac{\bar{u}^2}{\bar{c}_s^2}$$

the nondimensional pressure is

$$\bar{p} = \frac{2}{5}\bar{\rho}(\bar{h}_{t0} + 2\bar{E} - \frac{\bar{u}^2}{2} - 2\bar{E}b)$$

and the nondimensional sonic speed, $c_s = \gamma\bar{p}/\bar{\rho}$ is

$$\bar{c}_s^2 = \frac{2}{3}(\bar{h}_{t0} + 2\bar{E} - \frac{\bar{u}^2}{2} - 2\bar{E}b)$$

These equations are subject to the single parameter, R_m, the magnetic Reynolds number. Space-marching these equations forward from a subsonic inlet is be complicated by a smooth sonic passage condition [46]:

$$\frac{5}{2}\bar{u}_s b_s = \bar{E}$$

when $M = 1$. (the subscript "s" refers to the sonic point) Combining these equations results in the following expression for the sonic speed as a function of $\bar{E}$:

$$u_s^3 - \frac{1}{2}(\bar{h}_{t0} + 2\bar{E})u_s + \frac{2}{5}\bar{E}^2$$

and the three real roots (provided that $(\bar{h}_{t0} + 2\bar{E})^3/216 - \bar{E}^4/25 \geq 0$) can be found from $(i = 1, 2, 3)$ are:

$$u_{si} = -2\sqrt{\frac{\bar{h}_{t0} + 2\bar{E}}{6}} \cos\left(\frac{\theta + (i-1)2\pi}{3}\right)$$

where the argument θ is

$$\theta = \arccos\left(\frac{E^2/5}{((\bar{h}_{t0} + 2\bar{E})/6)^{3/2}}\right)$$

One of the roots is negative $(i = 1)$, and can be discarded.

From equation A.19, at the sonic point

$$\frac{du}{d\xi} = u' = \frac{N}{D} = \frac{0}{0}$$

where the superscript $'$ denotes a derivative with respect to ξ and will refer to the derivative evaluated at the sonic point in this analysis. From L'Hopital's rule, the derivative can be found from

$$u' = \frac{N_u u' + N_b b'}{D_u u' + D_b b'}$$

which has the solution

$$u' = \frac{N_u - D_b b'}{2D_u}\left[1 \pm \sqrt{1+f}\right] \tag{A.20}$$

where the factor f is defined as

$$f = \frac{4N_b b' D_u}{(N_u - D_b b')^2}$$

and the set of partial derivatives required for Martinez' model are:

$$D_u = 4u$$

$$D_b = 2E$$

$$N_u = 3R_m E u b$$

$$N_b = 3R_m E u^2$$

and

$$f = -\frac{2u_s^2}{Eb} = -\frac{4u}{5b^2}$$

Plugging these results into the L'Hopital's rule format, the derivative of the speed variable is, using $E = 2.5u_s b_s$,

$$u' = \frac{3}{4}R_m E b\left[1 \pm \sqrt{1 - \frac{4}{5}\frac{u}{b^2}}\right] \tag{A.21}$$

One of the two positive real roots of the sonic point equation (the lower value of the two) yields $\frac{4}{5}\frac{u}{b^2} < 1$, which is two positive slopes. The other root yields $\frac{4}{5}\frac{u}{b^2} > 1$, which is a spiraling singularity. This behavior is evident in figure A.1. This is the trajectory of a $R_m = 4.928$ solution superimposed on a map of isoclines on the $u - b$ phase plane. The physically significant sonic point is at $(u, b) = (0.2465, 0.8925)$, and the solution passes through smoothly. The two slopes calculated at this sonic point are shown as well. The other singularity is at $(u, b) = (0.588, 0.)$, and the isoclines clearly indicate the spiraling singularity centered there.

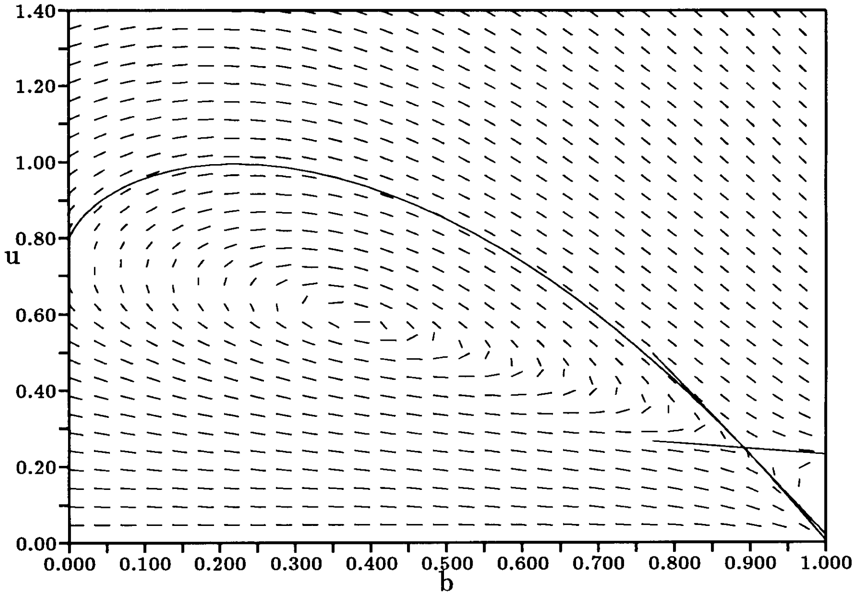

Figure A.1: u-b phase plane, $R_m = 4.928$

Martinez [46] solved this problem by a shooting method, starting at the inlet, and trying to thread through the sonic point, with the initial Mach number and the electric field as the eigenvalues. This author solved the same problem by starting at the sonic point, with the slopes as in A.21, and integrating in both directions, using the position of the sonic point and the electric field as eigenvalues. In both cases, the solution had to be searched for. This problem is solved here using the *COLSYS* relaxation package, which is faster, and avoids the problems of integrating through a singularity. The solution approach is described in the subsections below, and then results for the model of Martinez' are presented.

Note also, that the integrated form of the momentum equation is available.

$$F = \rho u^2 + p + b^2$$

along with the integrated energy equation:

$$H = h + \frac{u^2}{2} + 2Eb$$

combining these two expressions, a momentum equation which relates u and b can be obtained:

$$F = \frac{4}{5}u + \frac{2}{5}\frac{H - 2Vb}{u} + b^2 \tag{A.22}$$

At low u, then the balance is basically

$$F - b^2 \approx \frac{2}{5}\frac{H - 2Vb}{u}$$

so that decreasing b at low speed (i.e., subsonic) increases u, via the pressure term. At high speed (supersonic), the balance is

$$F - b^2 \approx \frac{4}{5}u$$

which again is increasing u with decreasing b.

Both sets of boundary conditions are shown in table A.1. For the upstream domain, $\xi = 0$, where $t = 0$, and, at the sonic point, $\xi = \xi_s$, where $t = 1$. Similarly, for the downstream variables $\xi = 1$ is also $t = 0$ in the downstream case, and, at the sonic point, $\xi = \xi_s$, again $t = 1$.

t	upstream condition	downstream condition
0	$b = 1$ (inlet)	$b = 0$ (exit)
1 (sonic point)	$M = 1$	$M = 1$
1 (sonic point)	$\frac{5}{2}\bar{u}_s b_s = \bar{E}$	$\frac{5}{2}\bar{u}_s b_s = \bar{E}$

Table A.1: Boundary conditions for both domains

To close out the problem, two more conditions are necessary. They are that the length of the channel is 1, and a continuous magnetic field slope across the sonic point:

$$\xi_s + \xi_u = 1$$

$$\left(\frac{db}{d\xi}\right)_1 = \left(\frac{db}{d\xi}\right)_2$$

The set of eight equations and eight boundary conditions may be solved simultaneously now, using the *COLSYS* routine described above.

Note that the sonic point boundary conditions ensure that all of the smoothness requirements are met between the two subdomains (where the jump in values at the sonic point $\| u \| = (u_d - u_u)$ evaluated at $t = 1$)

$$\|\bar{u}\|= 0, \quad \|b\|= 0, \quad \|\bar{E}\|= 0, \quad \|\bar{u}'\|= 0, \quad \|b'\|= 0$$

Having discussed the solution method, the next section briefly presents the results for this test case.

A.3.1 Numerical Results for Martinez' Model

Martinez presented results for $R_m = 4.928$ (a "low" R_m case. the channel is nearly choked at the exit plane) and $R_m = 47$ (a "high" R_m case.), and the results from this work are shown for these cases.

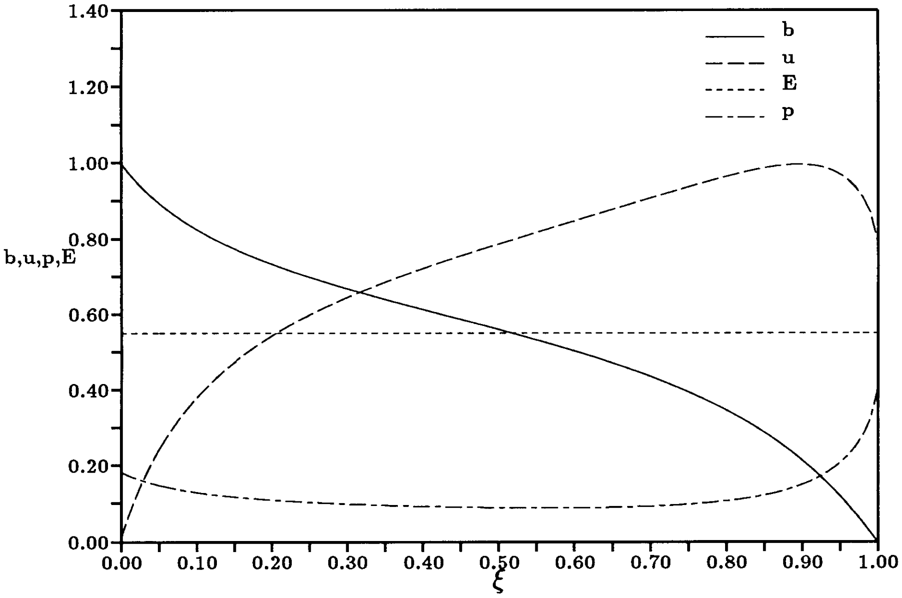

Figure A.2: b, u, E, p at $R_m = 4.928$. $\bar{E} = 0.54992$ and $\xi_s = 0.0518$. There are 40 intervals in each subdomain.

A.3.2 Discussion of Solution Methods for Flow Problems

The constant speed ignition problem is solved as a case of a flow problem with unknown bounds on the independent variable (usually the ionization fraction is chosen).

The solution method outlined above for flow problems involving an internal singularity will be applied to the accelerating inlet ignition problem.

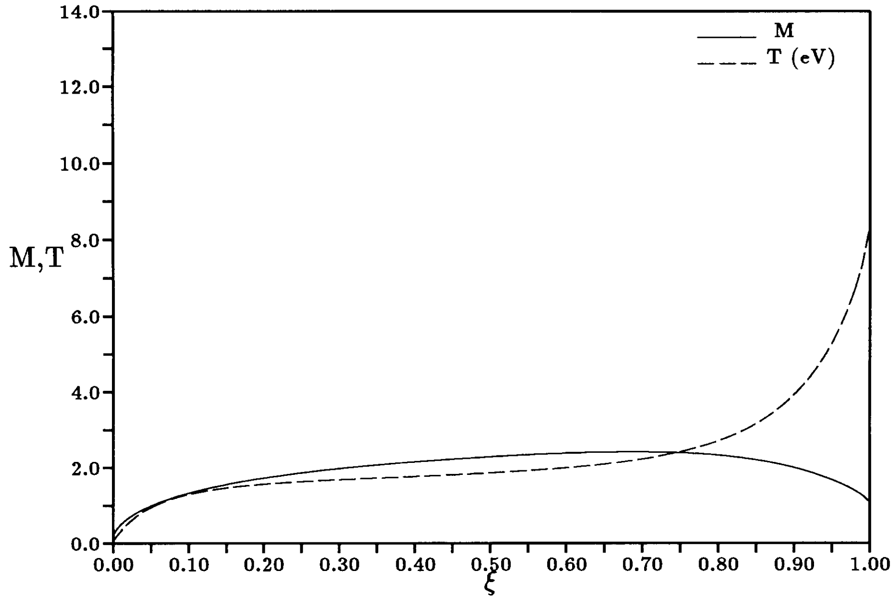

Figure A.3: M, T (eV) at $R_m = 4.928$. At R_m below about 4.8, the exit is thermally choked and there may be shocks in the channel.

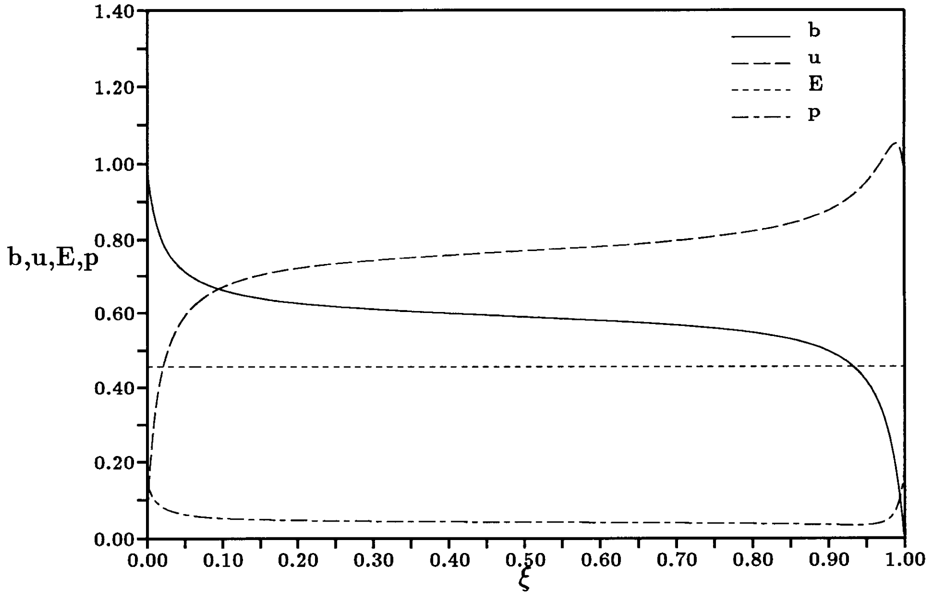

Figure A.4: b, u, E, p at $R_m = 47.68$. $\bar{E} = 0.4549$ and $\xi_s = 0.00499$. There are 160 intervals in each subdomain.

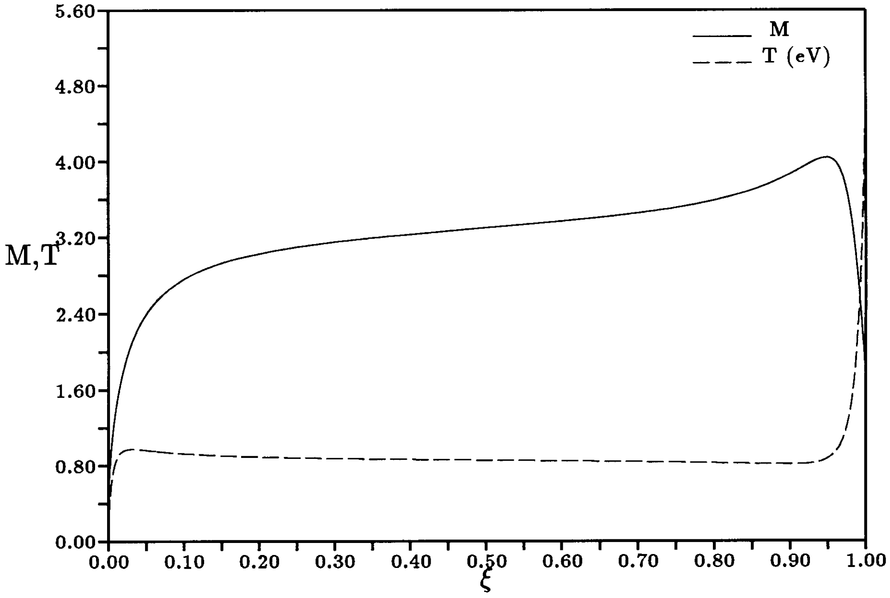

Figure A.5: M, T (eV) at $R_m = 47.68$

Appendix B

Atomic and Ion Properties

B.1 Lumping Levels Together

In order to make reasonable collisional-radiative analysis possible and because close-lying levels are likely to be very closely coupled via collisions, various energy levels are "lumped" together. Lumping levels together appears to be the most practical compromise between including details and keeping the model reasonable.

Levels are lumped together by multiplet. Such lumped levels are also suggested by Katsonis [35] and Gomes [24]. Values associated with each level: the energy and oscillator strength or transition probability, are averaged, weighted by the degeneracies of the "sub-levels", and a new, large degeneracy - the sum of the degeneracies of the constituents - is used. Thus, the lumped energy and transition probabilities are averaged as:

$$\text{Average Value} = \frac{\sum g_i Value_i}{\sum g_i}$$

The lumped degeneracies are:

$$\bar{g}_k = \sum g_i$$

Where the sums in the two previous equations are over the range of energy levels included in the lumped layer.

B.2 The Argon Atom (AI)

B.2.1 Lumped Energy Levels and Degeneracies

Table B.1 shows the lumped levels used for the atomic argon model. These are the same levels used by Gomes [24].

B.2.2 Radiative Einstein Coefficients

Some of the Einstein coefficients for the lumped levels in the argon atomic model were taken from Gomes [24]. Additional coefficients were found in Wiese [75]. These coefficients (1/sec) for the atom are listed in table B.2 below:

B.3 The Argon Ion (AII)

The motivation for looking at the argon ion was to be able to calculate populations of ionic excited states used for spectroscopic diagnostics of plasma accelerators. Kilfoyle used six argon ion lines to determine temperature. The upper energies of these lines range from 19.68 to 22.7 eV, as shown below in table B.3. In order to resolve these levels with some accuracy, levels up to roughly 2 eV above the highest upper level used were formulated.

B.3.1 Lumped Energy Levels and Degeneracies

The first 17 levels are from Gomes [24]. The fifteen additional levels were lumped together from data in Wiese [75], and the additional associated radiative lines were added.

For the argon(II) model, the following lumped levels were used. The ground state and first 16 levels were taken from [24], and are shown in table B.4, while the upper lumped levels ($k > 17$) were compiled using data from [75]. It was assumed that the number density of doubly-ionized argon(III) ions is small compared with the singly ionized argon(II). There is still a significant gap between the uppermost excited state and the doubly ionized argon ion.

The new levels are listed below in table B.5

The Einstein coefficients (1/sec) for the ion are listed in table B.6.

Lumped State:	Level k:	Energy, E_k (eV)	cm^{-1}	Degeneracy g_k
Ground	1	0.0	0	1
1st excited	2	11.648	93857	12
2nd excited	3	13.168	106079	36
3rd excited	4	14.082	113450	60
4th excited	5	14.132	113853	12
5th excited	6	14.566	117349	36
6th excited	7	14.839	119549	60
7th excited	8	14.899	120032	12
8th excited	9	14.962	120540	84
9th excited	10	15.083	121515	36
10th excited	11	15.200	122457	60
11th excited	12	15.238	122763	12
12th excited	13	15.269	123013	84
13th excited	14	15.335	123545	36
14th excited	15	15.393	124012	60
15th excited	16	15.419	124222	12
16th excited	17	15.437	124367	84
17th excited	18	15.474	124665	36
18th excited	19	15.510	124955	60
19th excited	20	15.526	125084	12
Continuum(Ion)	21	15.767	127025	6

Table B.1: Argon atom lumped levels used

```
-----------------------------------------------

A(2,1)=   2.50E8           A(3,2)=   3.37E7
A(6,2)=   2.3E6            A(10,2)=  7.12E5
A(18,2)=  4.738E5          A(4,3)=   1.717E7
A(5,3)=   2.014E7          A(7,3)=   1.78E6
A(8,3)=   6.10E6           A(11,3)=  2.73E6
A(12,3)=  2.73E6           A(15,3)=  1.957E6
A(16,3)=  1.450E6          A(19,3)=  1.58E6
A(20,3)=  9.097E5          A(6,4)=   2.15E6
A(9,4)=   3.51E7           A(10,4)=  6.32E5
A(13,4)=  5.016E7          A(14,4)=  3.024E5
A(17,4)=  2.87E7           A(18,4)=  1.643E5
A(6,5)=   4.08E6           A(10,5)=  4.018E5
A(14,5)=  1.874E5          A(7,6)=   2.145E6
A(8,6)=   4.54E6           A(11,6)=  1.73E5
A(12,6)=  1.564E6          A(15,6)=  2.07E5
A(16,6)=  8.069E5          A(19,6)=  1.766E5
A(20,6)=  5.195E5          A(9,7)=   5.03E5
A(10,7)=  1.0457E6         A(13,7)=  1.077E7
A(14,7)=  4.098E5          A(17,7)=  7.715E6
A(18,7)=  2.214E5          A(10,8)=  9.60E5
A(14,8)=  1.76E5           A(18,8)=  7.97E4
A(12,10)= 3.33E7           A(16,10)= 5.486E5
A(13,11)= 1.136E6          A(17,11)= 1.738E5
A(14,12)= 3.458E5          A(18,12)= 7.808E4

-----------------------------------------------
```

Table B.2: Argon atom radiative lines used

Wavelength (angstroms)	g_u	f	Upper Energy level (eV)
4082.39	6	0.0067	19.68
4481.81	6	0.149	21.50
4072.01	6	0.142	21.50
4079.60	6	0.043	21.50
4076.64	2	0.20	22.70
4076.94	4	0.12	22.70

Table B.3: Argon ion radiative lines used by Kilfoyle

B.4 The Hydrogen Atom (H)

B.4.1 Energy Levels and Degeneracies

The hydrogen levels were found in [75], and are listed in table B.7. Note that [49]

$$E_k = 13.6\left(1 - \frac{1}{k^2}\right)$$

and

$$g_k = 2k^2$$

B.4.2 Radiative Einstein Coefficients

The radiative Einstein coefficients for the hydrogen atom are given in table B.8. The values shown are 10^{-8} times th actual rate coefficients in units of 1/sec.

Lumped	Level	Energy, E_k		Degeneracy
State:	k:	(eV)	cm^{-1}	g_k
Ground (Argon II ion)	1	0.0	0	6
1st excited	2	13.476	108568	2
2nd excited	3	16.420	132286	20
3rd excited	4	16.702	134558	12
4th excited	5	17.177	138385	6
5th excited	6	17.688	142502	28
6th excited	7	18.016	145144	6
7th excited	8	18.300	147432	12
8th excited	9	18.438	148544	10
9th excited	10	18.542	148657	14
10th excited	11	18.697	150630	10
11th excited	12	19.244	155037	12
12th excited	13	19.543	157446	20
13th excited	14	19.707	158767	10
14th excited	15	19.839	159831	6
15th excited	16	19.962	160822	4
16th excited	17	19.967	160862	2
17th excited	18	21.160	170473	14
Argon III ion	33	27.620	222518	12

Table B.4: Argon ion lumped levels from Gomes

Lumped Energy level, k	Configuration	Coalesced Multiplets	Energy (eV)	Degeneracy g_k
18	$3p^4(^1D)4p$	$4p^2F$	21.16	14
19	$3p^4(^1D)4p$	$4p^2P$	21.40	12
20	$3p^4(^1D)4p$	$4p^2D$	21.52	20
21	$3p^4(^3P)5s$	$5s^4P$	22.594	12
22	$3p^4(^3P)4d$	$4d^4D$	22.817	20
23	$3p^4(^3P)4d$	$4d^4F$	23.04	28
24	$3p^4(^3P)4d$	$4d^4P$	23.172	12
25	$3p^4(^3P)4d$	$4d^2F$	23.23	14
26	$3p^4(^3P)4d$	$4d^2P$	23.63	6
27	$3p^4(^3P)4d$	$4d^2D$	23.909	10
28	$3p^4(^1D)5s$	$5s^2D$	24.312	10
29	$3p^4(^1D)4p$	$4d^2G$	24.651	14
30	$3p^4(^1D)4d$	$4d^2P$	24.763	6
31	$3p^4(^1D)4d$	$4d^2D$	24.800	14
32	$3p^4(^1D)4d$	$4d^2F$	24.847	14

Table B.5: Additional argon ionic lumped levels

```
-----------------------------------------------------------------

Ai(2,1)=   2.08E8       Ai(4,1)=   2.83E7       Ai(5,1)=   2.8E9
Ai(12,3)=  4.4E7        Ai(13,3)=  1.15E7       Ai(14,3)=  1.8E6
Ai(15,3)=  7.0E5        Ai(16,3)=  7.3E5        Ai(12,4)=  9.3E7
Ai(13,4)=  1.14E8       Ai(14,4)=  1.13E7       Ai(15,4)=  3.3E5
Ai(16,4)=  9.348E7      Ai(17,4)=  4.5E5        Ai(12,5)=  2.33E4
Ai(13,5)=  3.39E6       Ai(14,5)=  7.9E7        Ai(15,5)=  1.0E8
Ai(16,5)=  1.1E6        Ai(17,5)=  1.10E8       Ai(14,6)=  2.14E6
Ai(14,7)=  2.56E5       Ai(15,7)=  1.18E7       Ai(17,7)=  5.65E6
Ai(13,8)=  1.56E7       Ai(18,9)=  9.1E7        Ai(19,9)=  1.287E8
Ai(20,9)=  1.0165E8     Ai(18,10)= 4.5E6        Ai(20,10)= 6.1E6
Ai(18,11)= 1.533E7      Ai(20,11)= 2.953E7      Ai(21,12)= 1.1E8
Ai(22,12)= 2.915E8      Ai(23,12)= 3.03E6       Ai(24,12)= 2.0E8
Ai(21,13)= 5.0E7        Ai(22,13)= 6.5E7        Ai(23,13)= 3.45E8
Ai(24,13)= 4.535E7      Ai(25,13)= 5.614E6      Ai(21,14)= 2.1E6
Ai(22,14)= 2.46E6       Ai(23,14)= 4.4E6        Ai(24,14)= 1.2E6
Ai(25,14)= 3.9E8        Ai(26,14)= 3.9E7        Ai(21,15)= 7.7E6
Ai(24,15)= 2.5E5        Ai(25,15)= 9.86E5       Ai(26,15)= 2.7E8
Ai(27,15)= 3.56E8       Ai(21,16)= 1.65E7       Ai(23,16)= 5.0E6
Ai(24,16)= 1.5E8        Ai(26,17)= 1.27E7       Ai(27,17)= 7.2E7
Ai(28,18)= 1.4E8        Ai(28,19)= 3.82E7       Ai(28,20)= 3.9E7
Ai(29,18)= 4.0E8        Ai(30,19)= 1.7E8        Ai(30,20)= 3.82E7
Ai(31,18)= 3.1E7        Ai(31,19)= 1.3E8        Ai(31,20)= 1.05E8
            Ai(32,18)= 1.6E8        Ai(32,20)= 2.3E8

-----------------------------------------------------------------
```

Table B.6: Argon ion radiative lines

Lumped State:	Level k:	Energy, E_k (eV)	cm^{-1}	Degeneracy g_k
Ground	1	0.0	0	2
1st excited	2	10.210	82256	8
2nd excited	3	12.101	97490	18
3rd excited	4	12.763	102824	32
4th excited	5	13.069	105289	50
5th excited	6	13.235	106626	72
6th excited	7	13.336	107440	98
7th excited	8	13.401	107964	128
8th excited	9	13.446	108326	162
9th excited	10	13.478	108584	200
10th excited	11	13.501	108769	242
11th excited	12	13.519	108914	288
12th excited	13	13.533	109027	338
13th excited	14	13.544	109116	392
14th excited	15	13.553	109188	450
15th excited	16	13.561	109253	512
16th excited	17	13.567	109301	578
17th excited	18	13.572	109341	648
18th excited	19	13.576	109374	722
Continuum(Ion)	20	13.600	109567	1

Table B.7: Hydrogen Atom levels

```
-----------------------------------------------------------------
A(2,1)= 4.6990         A(3,1)= 0.5575         A(4,1)= 0.1278
A(5,1)= 4.125E-2       A(6,1)= 1.644E-2       A(7,1)= 7.568E-3
A(8,1)= 3.869E-3       A(9,1)= 2.143E-3       A(10,1)= 1.263E-3
A(11,1)= 7.834E-4      A(12,1)= 5.066E-4      A(13,1)= 3.393E-4
A(14,1)= 2.341E-4      A(15,1)= 1.657E-4      A(16,1)= 1.200E-4
A(17,1)= 8.858E-4      A(18,1)= 6.654E-5      A(19,1)= 5.077E-5
A(3,2)= 0.4410         A(4,2)= 8.419E-2       A(5,2)= 2.530E-2
A(6,2)= 9.732E-3       A(7,2)= 4.389E-3       A(8,2)= 2.215E-3
A(9,2)= 1.216E-3       A(10,2)= 7.122E-4      A(11,2)= 4.397E-4
A(12,2)= 2.834E-4      A(13,2)= 1.893E-4      A(14,2)= 1.303E-4
A(15,2)= 9.210E-5      A(16,2)= 6.658E-5      A(17,2)= 4.910E-5
A(18,2)= 3.685E-5      A(19,2)= 2.809E-5      A(4,3)= 8.986E-2
A(5,3)= 2.201E-2       A(6,3)= 7.783E-3       A(7,3)= 3.358E-3
A(8,3)= 1.651E-3       A(9,3)= 8.905E-4       A(10,3)= 5.156E-4
A(11,3)= 3.156E-4      A(12,3)= 2.021E-4      A(13,3)= 1.343E-4
A(14,3)= 9.211E-5      A(15,3)= 6.490E-5      A(16,3)= 4.680E-5
A(17,3)= 3.444E-5      A(18,3)= 2.580E-5      A(19,3)= 1.964E-5
A(5,4)= 2.699E-2       A(6,4)= 7.711E-3       A(7,4)= 3.041E-3
A(8,4)= 1.424E-3       A(9,4)= 7.459E-4       A(10,4)= 4.235E-4
A(11,4)= 2.556E-4      A(12,4)= 1.620E-4      A(6,5)= 1.025E-2
A(7,5)= 3.253E-3       A(8,5)= 1.388E-3       A(9,5)= 6.908E-4
A(10,5)= 3.80E-4       A(11,5)= 2.246E-4      A(12,5)= 1.402E-4
A(7,6)= 4.561E-3       A(8,6)= 1.561E-3       A(9,6)= 7.065E-4
A(10,6)= 3.688E-4      A(11,6)= 2.110E-4      A(12,6)= 1.288E-4
-----------------------------------------------------------------
```

Table B.8: Hydrogen Atom Einstein Coefficients $\times 10^{-8}\ s^{-1}$

Appendix C

Calculating Cross Sections and Level to Level Rate Coefficients

In the calculation of the collisional terms, the oscillator strengths for the transitions are required. From [49, Chapter 2], the relationship between the emission transition probabilities and absorption oscillator strengths (f_{kl}) can be derived. The oscillator strength for absorption is:

$$f_{kl} = \frac{A_{lk}}{\nu_{kl}^2} \frac{g_l}{g_k} \frac{\epsilon_o m_e c^3}{2\pi e^2}$$

and the corresponding emission oscillator strength is:

$$f_{lk} = \frac{g_k}{g_l} f_{kl}$$

Thus, only one of the two is necessary.

C.1 Collisional Rate Coefficients

The collisional rate coefficients for excitations and ionizations (both of which have units of $\frac{m^3}{s}$) are numerically integrated (see [49] for details) from:

$$S_{jk} = \int_{E_{jk}}^{\infty} f_m(E) Q^{j\to k} \frac{8\pi}{m_e^2} E dE \tag{C.1}$$

$$S_{kc} = \int_{E_{kc}}^{\infty} f_m(E) Q^{k\to c} \frac{8\pi}{m_e^2} E dE \tag{C.2}$$

Here $f_m(E)$ is the Maxwellian distribution for electrons, as a function of energy (E):

$$f_m(E) = \left(\frac{m_e}{2\pi k_B T_e}\right)^{\frac{3}{2}} \exp(\frac{E}{k_B T_e}) \tag{C.3}$$

and $Q^{k\to c}$ and $Q^{j\to k}$ (both functions of energy, E) are the ionization and excitation cross-sections.

The deexcitation and recombination rates are then calculated by taking into account that, in full equilibrium, each collisional process must be balanced by its opposite (microreversibility [49] [24] [24]). Thus,

$$\frac{S_{jk}}{S_{kj}} = (\frac{n_k}{n_j})^* = \frac{g_k}{g_j} \exp(\frac{-E_{jk}}{kT_e})$$

and

$$\frac{S_{kc}}{S_{ck}} = (\frac{n_e^2}{n_k})^* = \frac{2g_c}{g_k}(\frac{2\pi m_e k T_e}{h^2})^{\frac{3}{2}} \exp(\frac{-E_{kc}}{kT_e})$$

Where the g's are the degeneracies, c refers to the ion (the continuum), and superscript $*$ refers to the Saha equilibrium value.

C.1.1 Rates via Integrated Drawin Cross-Sections

For the non-elastic excitation (optically allowed transitions) and ionization cross-sectional areas, formulae of Drawin (see [20] and [49, Ch. 2, Sec. 4]) are:

$$Q^{j\to k} = 4\pi a_o^2(\frac{E_{1c}^H}{E_{jk}})^2 f_{jk}\beta_1 g(u) \tag{C.4}$$

$$Q^{k\to c} = 2.66\pi a_o^2(\frac{E_{1c}^H}{E_{kc}})^2 \xi_k \beta_1 g(u) \tag{C.5}$$

u is the nondimensional energy, $\frac{E}{E_{jk}}$ or $\frac{E}{E_{kc}}$ depending on the case. E_{1c}^H is the ionization energy of hydrogen (13.6 eV), a_o is the Bohr radius ($5.292e-11m$), β_1 is an adjustable constant of order unity, ξ_k is the number of equivalent electrons in level k, f_{jk} is the oscillator strength, and the function $g(u)$ is:

$$g(u) = \frac{u-1}{u^2}\ln(1.25\beta_2 u) \tag{C.6}$$

Where β_2 is of order unity.

(The ionization cross-sections have been compared (for $\beta_1 = \beta_2 = 1$) with measurements and, away from the threshold region, the differences are no more than a factor of two. The excitation cross-sections have not been tested as thoroughly, but they appear to be realistically within an order of magnitude of experimental findings [49].)

The numerical integrations are aided by a simplification of the integrals. Combining equations C.1 and C.2 with equations C.4, C.5, and C.6,

$$S_{jk} = \int_{E_{jk}}^{\infty} f_m(E)(4\pi a_o^2(\frac{E^H_{1c}}{E_{jk}})^2 f_{jk}\beta_1)(\frac{u-1}{u^2}\ln(1.25\beta_2 u))\frac{8\pi}{m_e^2}EdE \tag{C.7}$$

or

$$S_{jk} = 32 f_{jk}\beta_1 \left(\frac{\pi a_o E^H_{1c}}{m_e}\right)^2 \left(\frac{m_e}{2\pi k_B T_e}\right)^{\frac{3}{2}} \int_1^{\infty} f_m(u,\theta_{jk})(\frac{u-1}{u^2}\ln(1.25\beta_2 u))udu \tag{C.8}$$

$$f_m(u,\theta_{mn}) = \left(\frac{m_e}{2\pi k_B T_e}\right)^{\frac{3}{2}} \exp(\frac{u}{\theta_{mn}})$$

Similarly,

$$S_{kc} = 8(2.66)\xi_k\beta_1 \left(\frac{\pi a_o E^H_{1c}}{m_e}\right)^2 \left(\frac{m_e}{2\pi k_B T_e}\right)^{\frac{3}{2}} \int_1^{\infty} f_m(u,\theta_{kc})(\frac{u-1}{u^2}\ln(1.25\beta_2 u))udu \tag{C.9}$$

and both of these forms (equations C.8 and C.9) can be expressed as:

$$S_{jk} = 32 f_{jk}\beta_1 \left(\frac{\pi a_o E^H_{1c}}{m_e}\right)^2 \left(\frac{m_e}{2\pi k_B T_e}\right)^{\frac{3}{2}} I_{jk} \tag{C.10}$$

$$S_{kc} = 8(2.66)\xi_k\beta_1 \left(\frac{\pi a_o E^H_{1c}}{m_e}\right)^2 \left(\frac{m_e}{2\pi k_B T_e}\right)^{\frac{3}{2}} I_{kc} \tag{C.11}$$

where the integrals $I_{mn}(\theta_{mn})$ are:

$$I_{mn} = \int_1^{\infty} f_m(u,\theta_{mn})(\frac{u-1}{u^2}\ln(1.25\beta_2 u))udu \tag{C.12}$$

These integrals are evaluated numerically, so that all of the rate coefficients can then be calculated.

Appendix D

Boltzmann Plots of Excited Level Population Distributions from Multi-Level Models

Boltzmann plots are graphs of $\ln \frac{n_k}{g_k}$ vs $E_k(eV)$, and are the common method of displaying excited level population results. Note that, in collisional equilibrium, the levels will be in the Boltzmann distribution, and they lie on a straight line, of slope $\frac{1}{T_e(eV)}$ on a Boltzmann plot. In each of the following Boltzmann plots, the equilibrium solution (pinned down by the calculated ground state density) is shown as the straight line with no symbols. Although mks units have been used throughout this thesis, cgs units will be used for this appendix since this is the standard in CR references to simplify comparisons. Note that the number density conversion factor is $1\ m^{-3} = 10^{-6}\ cm^{-3}$.

D.1 Nonequilibrium Ionization in the Static Stationary Case

In this analysis, a stationary plasma (e.g. a discharge tube) is considered. Here, diffusion may be significant; however, unlike an MPD thruster flow, convection contributions are zero.

The total density balance, neglecting convection, is:

$$\nabla \cdot (n_e \vec{u_e}) = \dot{n}_e \qquad (D.1)$$

$$\nabla \cdot (n_{k=1} \vec{u}_{k=1}) = \dot{n}_{k=1} \tag{D.2}$$

$$\nabla \cdot (n_{k>1} \vec{u}_{k>1}) = \dot{n}_{k>1} \tag{D.3}$$

These continuity equations can be solved along with the other equations of motion in a numerical flow simulation. In the steady state, no flow case the balance is between the terms on the right-hand side, and an algebraic solution for the number densities can be found. Such a case is referred to as a static case.

The standard form of the Collisional-Radiative (CR) equations may be found in several references, amongst which are Bates, Kingston and WcWhirter (1962) [7], Mitchner and Kruger (1973)0 [49], and van der Sijde, van der Mullen and Schram (1984) [71].

The continuum rate equation is the sum of collisional ionization and losses from collisional recombination and radiative recombination:

$$\dot{n}_e = n_e \sum_k n_k S_{kc} - n_e^2 \sum_k (n_e S_{ck} + A_{ck}\beta_{ck}) \tag{D.4}$$

where S_{kc} is the ionization rate coefficient for each level k to the continuum (c), S_{ck} is the collisional (three-body) recombination rate coefficient, and $A_{ck}\beta_{ck}$ represents the net radiative recombination rate through use of the radiative escape factor.

The rate equations for a level k are the sum of: excitation and dexcitation processes with other levels, recombination from the continuum minus ionization, the gain from radiative decays from higher levels minus the loss by radiative decay to lower levels, and radiative recombination:

$$\begin{aligned} \dot{n}_k = {} & n_e \sum_{j<k} n_j S_{jk} - n_k\Big[\sum_{j<k} (n_e S_{kj} + A_{kj}\beta_{kj}) + n_e\Big(\sum_{l>k} (S_{kl}) + S_{kc}\Big)\Big] \\ & + \sum_{l>k} n_l (n_e S_{lk} + A_{lk}\beta_{lk}) + n_e^2 (n_e S_{ck} + A_{ck}\beta_{ck}) \end{aligned} \tag{D.5}$$

where the S_{ck}, S_{kc} and $A_{ck}\beta_{ck}$ terms are as described above, S_{jk}, S_{kj} ($k > j$) and S_{kl}, S_{lk} ($l > k$) are the collisional excitation and deexcitation rate coefficients from and to level k from higher and lower levels, and $A_{kj}\beta_{kj}$, $A_{lk}\beta_{lk}$ are losses due to radiative decay from k down and gain from decays from above k, respectively. These equations are linear in the level densities, n_k. The upper states are assumed to be in dynamic balance (the QSSS assumption considered in Chapter 3), there is no flow, although ambipolar diffusion is allowed. In this case,

$$\nabla \cdot (n_e \vec{u_e}) = D_a \frac{\partial^2 n_e}{\partial y^2} = \frac{D_a n_e}{h^2}$$

so that the equations to be solved for the ground state and excited state densities, for a given electron number density are

$$\begin{aligned} \frac{D_a n_e}{h^2} &= \dot{n}_e && \text{(D.6)} \\ 0 &= \dot{n}_{k>1} && \text{(D.7)} \end{aligned}$$

where $h = H/\sqrt{12}$ for a volume of height H, as shown in section 2.2.2, where the ambipolar diffusion coefficient was also shown to be

$$D_a = \frac{C_a(T_e, T_g)}{n_g} = \frac{C_a(T_e, T_g)}{n_e + \sum n_k}$$

Note that the denominator of this last expression makes the problem nonlinear in the number densities, and the problem is solved iteratively.

D.2 Hydrogen Model

We will but first, a brief discussion of some earlier models of hydrogen will be helpful in putting these results into context.

Bates, McWhirter, and Kingston [7] [8] and Shaw, Mitchner, and Kruger [62] both analyzed steady-state three-level models of the hydrogen atom in both optically thin and optically thick cases. In both works, they calculated the population of the ground state, as well as the overall ionization and recombination coefficients. The results of both research teams agree with one another very well, and the general trends that were shown in Chapter 3 of this thesis were shown as well. That is, the recombination coefficient fell with decreasing escape factor, and rose with decreasing electron number density. However, as was also shown in Chapter 3 here, the upper levels play a significant roll at temperatures below ...

For the 19-level hydrogen model, some results for the stationary case are shown. The cases that will be shown here are listed in table D.1. Figures D.1, D.2, D.3, D.4, and D.5 are Boltzmann plots corresponding to these cases. Note that the uppermost levels approach their equilibrium values under virtually all of the cases, even when the ground state and the lower excited levels are far out of equilibrium.

Case	T_e (K)	n_e (cm^{-3})	H (cm)	β_{n1}
H1	8000	10^{14}	4	0.00
H2	8000	10^{14}	4	0.01
H3	8000	10^{14}	4	0.10
H4	8000	10^{14}	4	1.00
H5	8000	10^{13}	4	0.00
H6	8000	10^{13}	4	0.10
H7	20000	10^{14}	4	0.00
H8	20000	10^{14}	4	0.10
H9	20000	10^{13}	4	0.00
H10	20000	10^{13}	4	0.10
H11	20000	10^{13}	2	0.00
H12	20000	10^{13}	2	0.10

Table D.1: Hydrogen atom, cases shown in Boltzmann plots.

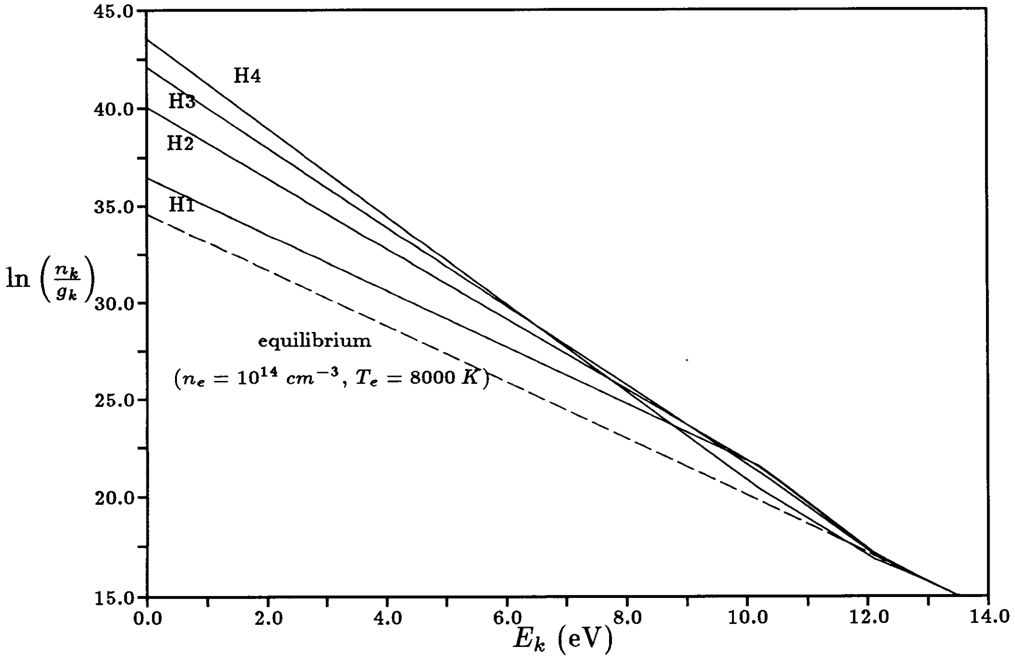

Figure D.1: Hydrogen model, Boltzmann plots for cases H1, H2, H3, H4 from table.

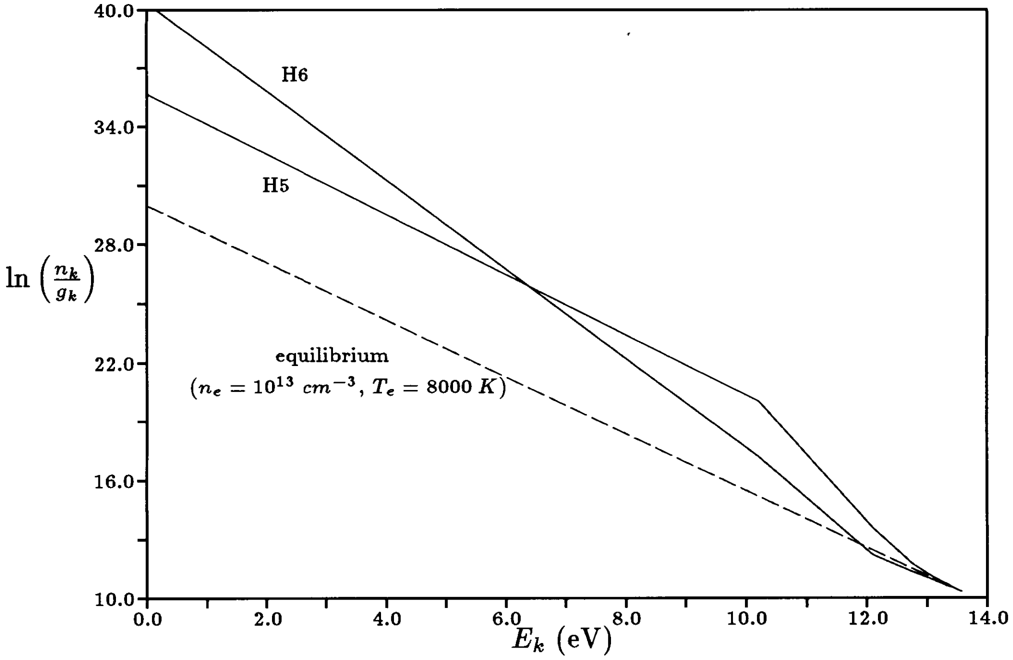

Figure D.2: Hydrogen model, Boltzmann plots for cases H5 and H6 from table.

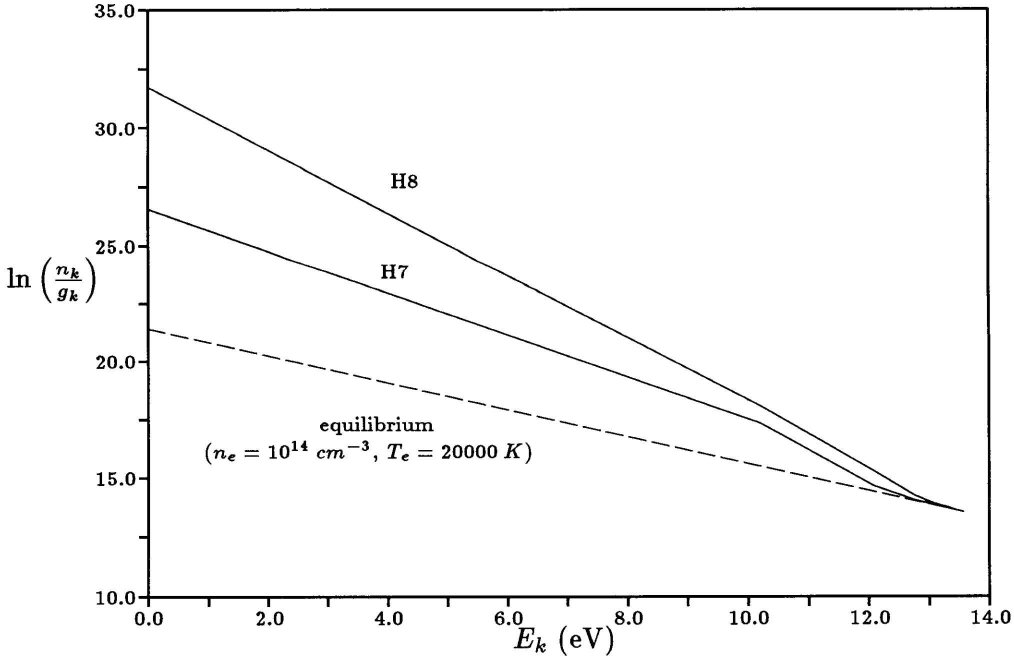

Figure D.3: Hydrogen model, Boltzmann plots for cases H7 and H8 from table.

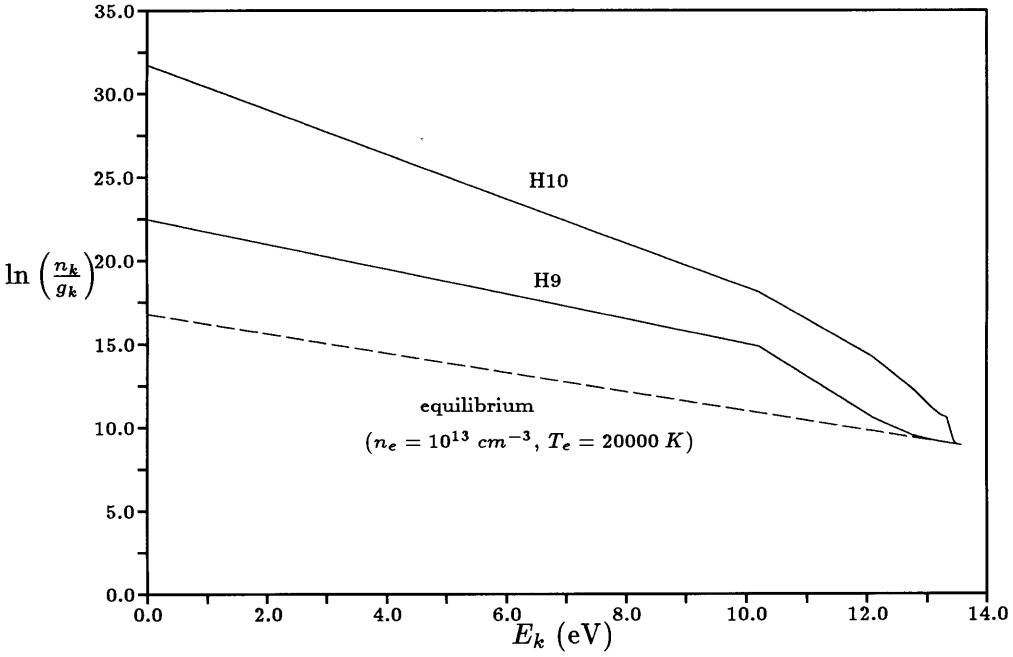

Figure D.4: Hydrogen model, Boltzmann plots for cases H9 and H10 from table.

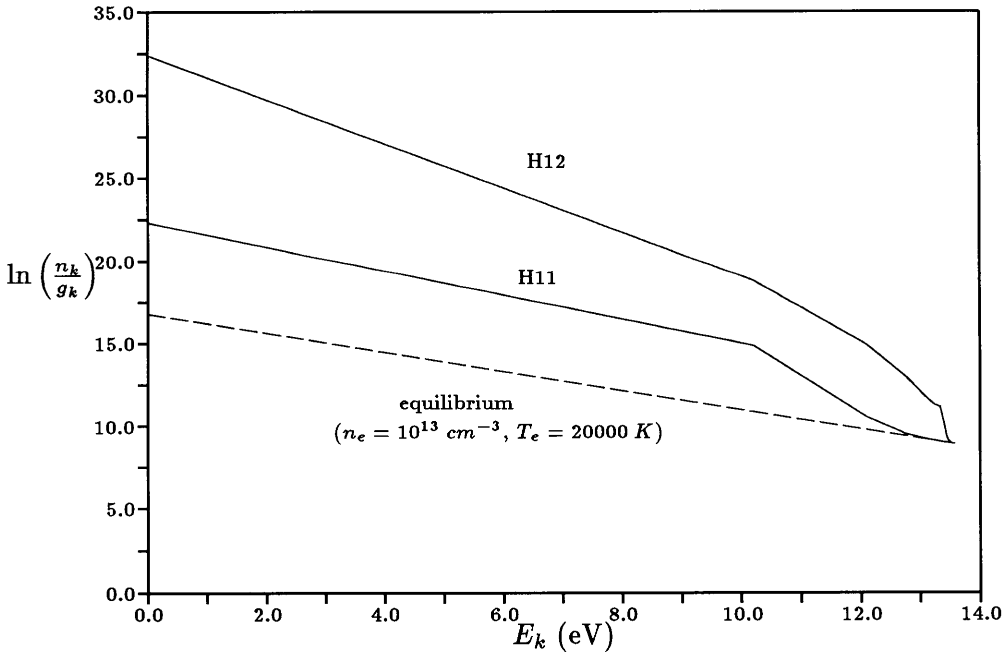

Figure D.5: Hydrogen model, Boltzmann plots for cases H11 and H12 from table.

D.3 Argon Model: Generating Boltzmann Plots for Flow Problems (Ignition)

As observed earlier, one of the advantages of using the QSSS assumption for the excited states to arrive at overall rate coefficients is that the excited state population distribution may be calculated a posteri. This provides a bridge between a computational model of an MPDT channel flow and the interpretation of spectroscopic disgnostic measurements.

The ignition models of Chapter 4 all use the overall coefficients calculated in Chapter 3 for either the argon or hydrogen atom, so that the excited state population distribution may be obtained in post-processing. The electron temperature, T_e, is a known constant, and n_e and n_1 are known everywhere along the solution trajectory (with α as the independent variable). Therefore $\delta_1 = (n_1/n_1^* - 1)$ may be found. The degree of nonequilibrium of each of the excited levels may be expressed as $\delta_k = \chi_k \delta_1$ for this case (no radiative effects). Then the procedure outlined in section 3.3.1 applies, and all of the χ_k values may be calculated. Finally, the number density for each level may be found from the definition of the degree of nonequilibrium:

$$n_k = n_k^*(\delta_k + 1) = n_k^*(\chi_k \delta_1 + 1)$$

This is shown in figures D.6 and D.7 for two cases of constant temperature, constant speed injection of argon. In each figure, plots are included for close to the inlet wall (the lowest α), a moderate ionization fraction ($\alpha = 0.50$), and for near to the asymptotic limit (the largest α). In these cases, the ground state is very overpopulated relative to its equilibrium population, which is characteristic of a strongly ionizing plasma. Because of this, even the uppermost excited levels only approach their equilibrium populations.

These results agree qualitatively with the findings of Takano and Akamatsu [67], who used an argon atomic model with six actual excited states and 9 higher energy hydrogenic excited states (quantum numbers 4 to 9) to analyze a shock-heated plasma. Their model included atom-atom and electron-atom collisions, plus radiation, using calculated radiation escape factors, but the extra processes did not have a great effect.

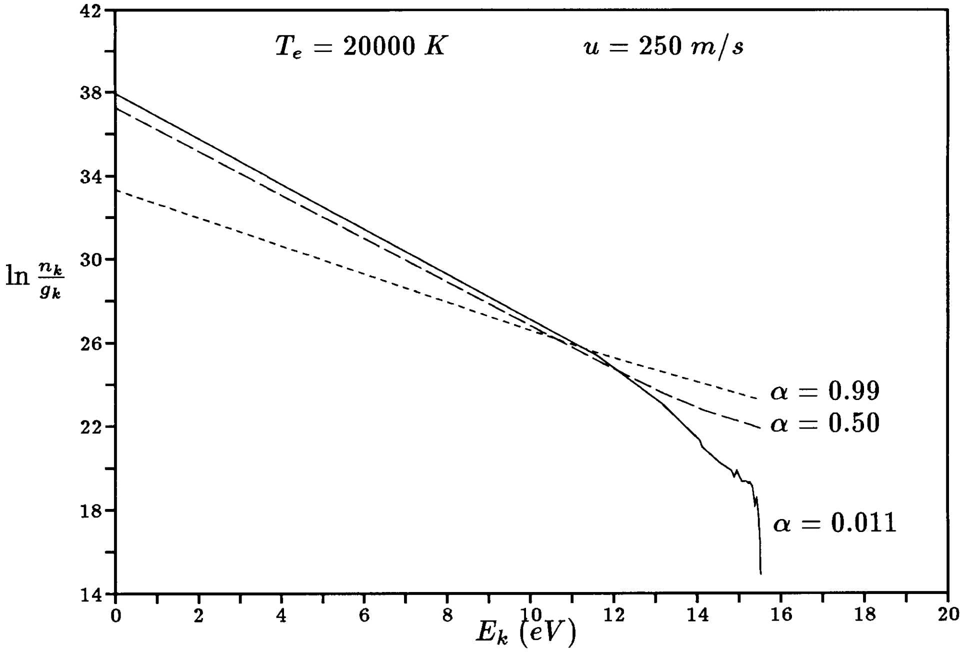

Figure D.6: Boltzmann plots at three different values of α for the constant speed, constant electron temperature model of Chapter 4. Here, $T_e = 20000\ K$ and $u = 250 m/s$.

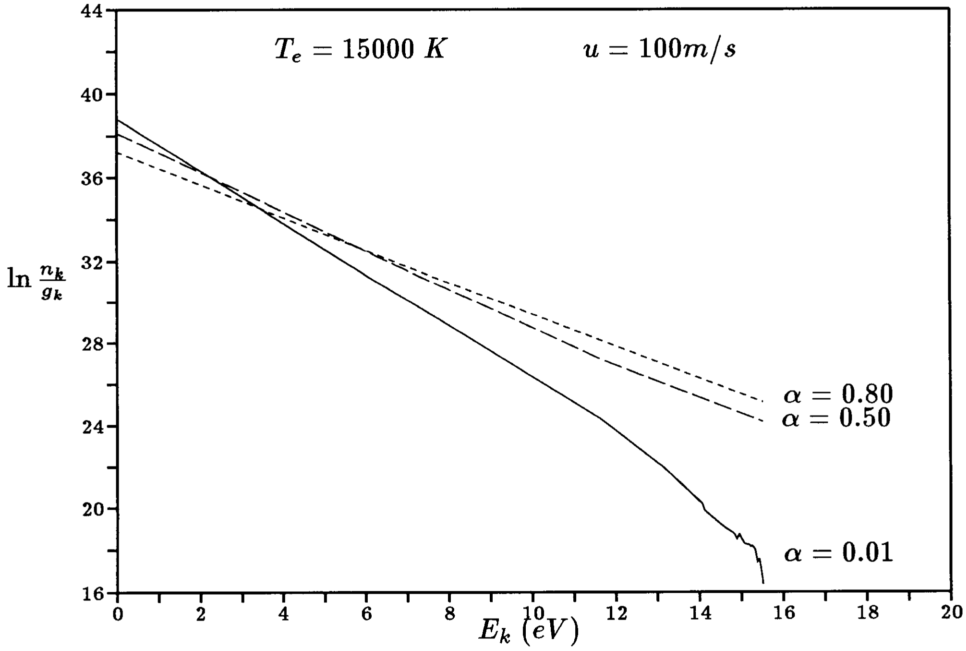

Figure D.7: Boltzmann plots at three different values of α for the constant speed, constant electron temperature model of Chapter 4. Here, $T_e = 15000\ K$ and $u = 100 m/s$.

Bibliography

[1] Abramov. Investigation of Electron Temperature and Plasma Radiation in a Quasi-Stationary High-Current Discharge Between Coaxial Electrodes. In *Proceedings of the 8th Intl. Conf. on Phen. in Ionized Gases*, 1968.

[2] U. Ascher, J. Christiansen, and R. D. Russell. Collocation software for boundary-value odes. *ACM Trans. Math Software*, 7:209–222, 1981.

[3] U. M. Ascher, R. M. M. Mattheij, and R. D. Russell. *Numerical Solution of Boundary Value Problems for Ordinary Differential Equations.* Prentice Hall, Englewood Cliffs, NJ, 1988.

[4] J. Bacri and A. M. Gomes. Influence of atom-atom collisions on thermal equilibrium in argon arc discharges at atmospheric pressure. *J. Phys. D.: Appl. Phys.*, 11:2185–2197, 1978.

[5] J. Bacri, A. M. Gomes, and S. Benzaid. Etude des ecarts a l'ETL dans un arc d'argon (P = 760 Torr). *J. Phys. D.: Appl. Phys.*, 9:1743–1755, 1976.

[6] G. Bader and U. Ascher. A new basis implementation for a mixed order boundary value ode solver. *SIAM J. Sci. Stat. Comp.*, 8:483–500, 1987.

[7] D. R. Bates, A. E. Kingston, and W. P. McWhirter. Recombination Between Electrons and Atomic Ions - I. Optically Thin Plasmas. *Royal Society of London Proceedings, Ser. A*, 267:297–312, May 1962.

[8] D. R. Bates, A. E. Kingston, and W. P. McWhirter. Recombination Between Electrons and Atomic ions - II. Optically Thick Plasmas. *Royal Society of London Proceedings, Ser. A*, 270:155–167, November 1962.

[9] Rodger J. Biasca. Chemical Kinetics of Scramjet Propulsion. Master's thesis, Dept. of Aeronautics and Astronautics, Massachusetts Institute of Technology, Cambridge, Massachusetts, 1988.

[10] J. A. Bittencourt. *Fundamentals of Plasma Physics.* Permagon Press, New York, 1986.

[11] C. G. Braun and J. A. Kunc. Collisional-radiative coefficients from a three-level atomic model in nonequilibrium argon plasmas. *Physics of Fluids*, 30(2):499 – 509, February 1987.

[12] K. V. Brushlinskii, A. M. Zaborov, A. N. Kozlov, A. I. Morozov, and V. V. Savel'ev. Numerical modeling of plasma flow in high-current quasistationary plasma accelerators. *Soviet Journal of Plasma Physics*, 16(2):79 – 85, February 1990.

[13] J. D. Buckmaster, editor. *The Mathematics of Combustion.* SIAM, Philadelphia, 1985.

[14] R. L. Burton and N. Tiliakos. Injected Propellant Ionization in MPD Thrusters. Technical report, 28th Joint Propulsion Conference, 1992. AIAA-92-3295.

[15] J. M. G. Chanty, March 1992. personal communication.

[16] Francis F. Chen. *Introduction to Plasma Physics and Controlled Fusion*, volume 1: Plasma Physics. Plenum Press, New York, 2nd edition, 1984.

[17] E. Y. Choueiri. An Introduction to the Plasma Physics of the MPD Thruster, Nov. 1991. Notes for an invited lecture, MAE, Physics of Electric Propulsion, Princeton, University.

[18] E. Y. Choueiri and H. Okuda. Anomalous Ionization in the MPD Thruster. Technical report, 23rd International Electric Propulsion Conference, 1993. IEPC-93-067.

[19] J. M. A. Danby. *Computing Applications to Differential Equations.* Reston Publishing Co., Reston, VA, 1985.

[20] H. W. Drawin. Zur formelmaBigen Darstellung der Ionisierungsquerschnitte gegenuber ElektronenstoB. *Zeitschrift fur Physik*, 164:513–521, 1961.

[21] E. Fischer, Z. Rozkwitalski, and F. K. Kneubuhl. Self-Field MPD Thruster with Atomic and Molecular Propellants. *Appl. Phys. B*, 38:41–49, 1985.

[22] Jahn R. G. and et al. Electric Propulsion Laboratory Progress Report. Technical report, Department of Mechanical and Aerospace Engineering, Princeton University, Princeton NJ, July 1987. MAE 1776.07.

[23] A. F. Ghoniem. Class notes for *Fundamentals and Modeling in Combustion*, Spring 1993, Massachusetts Institute of Technology.

[24] A. M. Gomes. Criteria for partial lte in an argon thermal discharge at atmospheric pressure; validity of the spectroscopically measured electronic temperature. *J. Physics, D: Applied Physics*, 16:357–378, 1983.

[25] David A. Gonzales. *Models for Vibration-Dissociation Coupling in High Temperature Gases.* PhD thesis, University of Texas at Austin, Austin, Texas, 1993.

[26] H. R. Griem. *Spectral Line Broadening by Plasmas.* Academic Press, New York, 1974.

[27] Daniel J. Heimerdinger. *Fluid Mechanics in a Magnetoplasmadynamic Thruster.* PhD thesis, Dept. of Aeronautics and Astronautics, Massachusetts Institute of Technology, Cambridge, Massachusetts, 1988.

[28] P. G. Hill and C. R. Peterson. *Mechanics and Thermodynamics of Propulsion.* Addison-Wesley, Reading, Mass., 1970.

[29] E. Hinnov and J. G. Hirschberg. Electron-Ion Recombination in Dense Plasmas. *Physical Review*, 125(3):795, 1962.

[30] T. Holstein. Imprisonment of Resonance Radiation in Gases. *Physical Review*, 72(12):1212–1233, 1947.

[31] T. Holstein. Imprisonment of Resonance Radiation in Gases. II. *Physical Review*, 83(6):1159–1168, 1951.

[32] R. G. Jahn. *Physics of Electric Propulsion.* McGraw Hill, New York, 1968.

[33] R. K. Janev, W. D. Langer, K. Evans Jr, and D. E. Post Jr. *Elementary Processes in Hydrogen-Helium Plasmas.* Springer-Verlag, New York, 1987.

[34] H. Kafrouni. Study of Electron Cooling, Diffusion and Recombination in a Decaying Argon Arc. *Physica*, 98 C:100, 1979.

[35] K. Katsonis and H. W. Drawin. Transition Probabilities for Argon(I). *J. Quant. Spectrosc. Radiat. Transfer*, 23:1–55, 1980.

[36] Daniel B. Kilfoyle. Spectroscopic Analysis of a Magnetoplasmadynamic Arcjet. Master's thesis, Dept. of Aeronautics and Astronautics, Massachusetts Institute of Technology, Cambridge, Massachusetts, 1988.

[37] D. Q. King. *Magnetoplasmadynamic Channel Flow for Design of Coaxial MPD Thrusters.* PhD thesis, Dept. of Mechanical and Aerospace Engineering, Princeton University, Princeton, New Jersey, 1981.

[38] K. Kuriki and H. Suzuki. Transitional Behavior of MPD Arcjet Operation. *AIAA Journal*, October 1978.

[39] K. Kuriki and H. Suzuki. Quasisteady MPD Arcjet with Anode Gas Injection. In R. C. Finke, editor, *Electric Propulsion and its Applications to Space Missions.* AIAA, 1981.

[40] M. R. LaPointe. Numerical Simulation of Self-Field MPD Thrusters. Technical report, 27th Joint Propulsion Conference, 1991. Paper AIAA-91-2341.

[41] J. L. Lawless and V. V. Subramaniam. A Theory of Onset in Magnetoplasmadynamic Thrusters. Technical report, 18th International Electric Propulsion Conference, 1985. Paper AIAA-85-2039.

[42] J. L. Lawless and V. V. Subramaniam. A Review of the Theory of Self-Field MPD Thrusters. Technical report, 22nd International Electric Propulsion Conference, 1991. Paper IEPC-91-019.

[43] M. A. Lennon, K. L. Bell, and etal. Recommended Data on the Electron Impact Ionization of Atoms and Ions: Flourine to Nickel. *J. Phys. Chem. Ref. Data.*, 17(3), 1988.

[44] M. A. Liberman and Velikovich. *Physics of Shock Waves in Gases and Plasmas.* Springer-Verlag, New York, 1986.

[45] R. A. London and B. P. Flannery. Hydrodynamics of X-ray Induced Stellar Winds. *The Astrophysical Journal*, 258:260–269, July 1 1982.

[46] M. Martinez-Sanchez. The Structure of Self-Field Accelerated Plasma Flows. *Journal of Propulsion and Power*, 7(1):56–64, January-February 1991.

[47] J. R. Melcher. *Continuum Electromechanics.* The MIT Press, Cambridge, MA, 1981.

[48] S. A. Miller. *Multifluid Nonequilibrium Simulation of Arcjet Thrusters.* PhD thesis, Dept. of Aeronautics and Astronautics, Massachusetts Institute of Technology, Cambridge, Massachusetts, 1993.

[49] M. Mitchner and C.H. Kruger Jr. *Partially Ionized Gases.* John Wiley and Sons, New York, 1973.

[50] Eliahu H. Niewood. Transient One Dimensional Numerical Simulation of Magnetoplasmadynamic Thrusters. Master's thesis, Dept. of Aeronautics and Astronautics, Massachusetts Institute of Technology, Cambridge, Massachusetts, 1989.

[51] Eliahu H. Niewood. *An Explanation for anode Voltage Drops in an MPD Thruster.* PhD thesis, Dept. of Aeronautics and Astronautics, Massachusetts Institute of Technology, Cambridge, Massachusetts, 1993.

[52] T. G. Owano, C. H. Kruger, and R. A. Beddini. Electron-Ion Three-Body Recombination Coefficient of Argon. *AIAA Journal*, 31(1), January 1993.

[53] S-I Pai, editor. *Radiation Gas Dynamics.* Springer-Verlag, New York, 1963.

[54] S-I Pai, editor. *Magnetogasdynamics and Plasma Dynamics.* Springer-Verlag, New York, 1966.

[55] E. Pfender. Electric Arcs and Arc Gas Heaters. In M. N. Hirsh and H. J. Oskam, editors, *Gaseous Electronics, Volume I: Electrical Discharges*, chapter 5. Academic Press, 9999.

[56] W. H. Press, B. P. Flannery, S. A. Teukolsky, and W. T. Vetterling. *Numerical Recipes: the art of scientific computing.* Cambridge Univ. Press, New York, 1986.

[57] W. H. Press and S. A. Teukolsky. Integrating Stiff Ordinary Differential Equations. *Computers in Physics*, May/June 1989.

[58] P. A. Ramachandran. A Numerical Solution Method for Boundary Value Problems Containing an Undetermined Parameter. *J. Computational Physics*, 102:63–71, 1992.

[59] T. M. Randolph, W. F. von Jaskowsky, A. J. Kelly, and R. G. Jahn. Measurement of Ionization Levels in the Interelectrode Region of an MPD Thruster. Technical report, 28th Joint Propulsion Conference, 1992. AIAA-92-3460.

[60] D. G. Samaras. *Theory of Ion Flow Dynamics.* Dover, New York, 1971.

[61] R. K. Seals, Jr. and H. A. Hassan. Analysis of MPD Arcs with Nonequilibrium Ionization. *AIAA Journal*, 6(12):2273–2278, Dec. 1968.

[62] J. F. Shaw, M. Mitchner, and C. H. Kruger. Effects of Nonelastic Collisions in Partially Ionized Gases, II: Numerical Solution and Results. *Physics of Fluids*, 13(2):339–345, Feb. 1970.

[63] E. J. Sheppard and M. Martinez-Sanchez. Ionizational Ignition at the Inlet of an MPD Thruster. Technical report, 22nd International Electric Propulsion Conference, 1991. IEPC-91-020.

[64] P. C. Sleziona, M. Auweter-Kurtz, and H. O. Schrade. MPD Thruster Calculation Considering High Ionization Modes. Technical report, 22nd International Electric Propulsion Conference, 1991. IEPC-91-087.

[65] S. Suckewer. Excitation and Ionization of Atoms and Ions in a Non-Thermal Plasma,I. Populations of Excited Levels. *Journal of Physics, B3*, 3:380 –389, 1970.

[66] H. Tahara, T. Tsubaki, Y. Kagaya, Y. Tsubakishita, and T. Yoshikawa. Diagnostic Experiment and Numerical Analysis of One-Dimensional MPD Flowfields. Technical report, 23rd International Electric Propulsion Conference, 1993. IEPC-93-197.

[67] Y. Takano and T. Akamatsu. Simulations for Collisional and Radiative Mechanisms of Shock-Heated Argon Plasma. In *XVI Intl. Conf. on Phen. in Ionized Gases*, 1983.

[68] K. Toki, M. Sumida, and K. Kuriki. Multi-Channel Two-Dimensional MPD Arcjet. Technical report, 19th International Electric Propulsion Conference, 1987. IEPC-87-1000.

[69] K. Uematsu, S. Morimoto, and K. Kuriki. MPD Thruster Performance with Various Propellants. *Journal of Sapcecraft*, 22(4):412–416, July-August 1985.

[70] J. J. A. M. van der Mullen, B. van der Sijde, and D. C. Schram. An Analytical Excitation Model for an Ionizing Plasma. *Physics Letters*, 96A(5):239–242, 1983.

[71] B. van der Sijde, J. J. A. M. van der Mullen, and D. C. Schram. Collisional Radiative Models in Plasmas. *Beitrage aus der Plasmaphysik*, 24(5):447–473, 1984.

[72] M. Venugopalan, editor. *Reactions Under Plasma Conditions.* Wiley-Interscience, New York, 1971.

[73] J. Vlcek and J. Ferdinand. Collisional-Radiative Recombination in Argon Plasmas. In *XVI Intl. Conf. on Phen. in Ionized Gases*, 1983.

[74] L. Vriens and A. H. M. Smeets. Cross-section and rate formulas for electron-impact ionization, excitation, deexcitation, and total depopulation of excited atoms. *Physical Review A*, 22(3):940–951, Sept. 1980.

[75] W. L. Wiese and G. A. Martin. *Wavelengths and Transition Probabilities for Atoms and Atomic Ions, Part II, Transition Probabilities.* National Bureau of Standards, Washington, D.C., 1980.

[76] F. A. Williams. *Combustion Theory.* Addison-Wesley, Reading, MA, 1965.